Recent advances in vanadium pentoxide (V$_2$O$_5$) towards related applications in chromogenics and beyond: fundamentals, progress, and perspectives

Top Khac Le, [iD] *[a] Phuong V. Pham, [iD] [b] Chung-Li Dong, [iD] [c] Naoufal Bahlawane, [iD] [d] Dimitra Vernardou, [iD] [e] Issam Mjejri,[f] Aline Rougier [iD] [f] and Sok Won Kim [iD] *[a]

Smart multifunctional V$_2$O$_5$ is an appealing oxide for energy-saving and energy-storage applications. This review article comprehensively analyzes its most recent advances and applications. The unique electronic structure of V$_2$O$_5$ with three bands triggers peculiar smart optical properties and multi-color appearance. The colors and optical characteristics of pristine V$_2$O$_5$ films are affected by the processing growth and conditions. The multi-chromism in V$_2$O$_5$ can be controlled by various external stimuli: applied voltage, electrochromic gas type, gasochromic; light source, photochromic; and temperature, thermochromic. Fundamental comprehension of chromism and "fixed-chromism" has been discussed. Chromism in V$_2$O$_5$ is reviewed, and the related advantages, drawbacks, and potential applications are emphasized with a focus on the fundamental aspects. General strategies to enhance the coloration performances of V$_2$O$_5$ chromogenic devices (CDs) are discussed. The role of the micro−nanostructural morphologies, growth conditions, doping elements, and hybrid composite structures on smart optical devices for improving the chromic performance is also addressed. The challenges that lie ahead of the commercialization of V$_2$O$_5$-based applied research are presented.

1. Introduction

The energy demand for heating, air-conditioning, ventilation, and lighting has increased due to climate change and the development of buildings, vehicles, and technology devices. Unfortunately, they all produce more greenhouse-gas emissions and induce global warming and climate change.[1] The energy increase has reached approximately 40% in the EU, 30% in the US, and 30–40% in the world of primary energy.[2–4] This energy can be reduced using optical devices to prevent and reduce excessive heating and lighting where necessary. Chromogenic devices (CDs) are known for their stimuli-dependent

optical properties and have attracted worldwide attention for reducing global warming. Indeed, electrochromic (EC), gasochromic (GC), photochromic (PC), thermochromic (TC), ionochromic (IC), solvatochromic (SC), vapochromic (VC), and mechanochromic (MC) devices play an essential role in energy saving and make an outstanding contribution to protecting the environment as a key "green" technology.

Energy saving *via* CDs is currently a major focus in the nanomaterial science community with a large number of publications. In this perspective, CDs are not only crucial for smart windows as energy-saving devices but are also used in displays, windows for civil aircraft, light modulators, sensors, eyeglass, stimuli-responsive devices, rear-view mirrors, and switching optics.[5] In addition, chromic properties are also extended to applications, such as thermal control in the IR region, and variable IR/NIR devices.[6,7]

As stated earlier, chromogenics corresponds to irreversible/reversible changes in material color and optical characterization caused by a change in the chemical and physical properties due to external stimuli. Among them, electrochromism has attracted considerable attention because of the facile control of the insertion/de-insertion of metal ions and carrier concentration at the applied voltage, allowing control of the optical contrast, switching time, and coloration

[a] *Department of Physics and Energy Harvest Storage Research Center, University of Ulsan, Ulsan 44610, Republic of Korea. E-mail: lekhactop@gmail.com, sokkim@ulsan.ac.kr*

[b] *School of Micro–Nano Electronics, Zhejiang University, Hangzhou 310027, China*

[c] *Research Center for X-ray Science & Department of Physics, Tamkang University, Tamsui 25137, Taiwan*

[d] *Luxembourg Institute of Science and Technology (LIST), 5 Avenue des Hauts–Fourneaux, L-4362 Esch-sur-Alzette, Luxembourg*

[e] *Department of Electrical and Computer Engineering, School of Engineering, Hellenic Mediterranean University, 71410 Heraklion, Greece*

[f] *Univ. Bordeaux, CNRS, Bordeaux INP, ICMCB, UMR 5026, F-33600, Pessac, France*

efficiency. Fritsch *et al.* first reported PC materials and their behaviors in 1867.[8] In the 20th century, chromic materials have been studied extensively since the report by Pohl on the chromic phenomena of alkali halides.[9] The possible change in the color produced by EC phenomena in dye materials was attributed to the shift of absorption and emission spectra under an electric field, which Platt studied in 1961.[10] Deb reported the first application of electrochromism in an electrophotographic system using WO_3 thin films in 1969.[11] For the three next decades from 1970 to 1999, transition metal oxide (TMO) films (*e.g.*, WO_3, VO_2, TiO_2, MoO_3, NiO, and V_2O_5) were used in CDs because of their higher thermal stability, strength, and chemical resistance. Since 2000, different morphologies of micro–nanostructures with large surface areas and favorable transport properties have enhanced the coloration efficiency.[8]

The significant attention on CDs has prompted considerable interest in papers reviewing EC materials. W.C. Dautremont-Smith first reviewed EC TMO materials and displays that include cathodic and anodic colorations in 1982.[12,13] Mortimer,[14] Thakur *et al.*,[15] and Rai *et al.*[16] reviewed other EC material types, such as conducting polymers, viologens, metal coordination complexes, Prussian blue, metal hybrids, hybrid materials (organic–inorganic), metal complexes, and metal plasmonics-metal/alloy. Recently, Wang *et al.*,[2] Ke *et al.*,[5] Dalapati *et al.*,[17] He *et al.*,[18] and Tallberg *et al.*[19] reviewed smart windows based on the electro-, thermo-, mechano-, and photochromic phenomena of materials. Recent progress in

Top Khac Le

Top Khac Le obtained his BS and MS degrees in Physics from the University of Science, Vietnam National University HCM City (US-VNUHCM). He then spent a few years as a researcher member and lecturer of faculty at the Dept. of Materials Science and Technology, US-VNUHCM. He earned his PhD degree in Physics (2019) from the University of Ulsan, South Korea. He is currently a Postdoctoral Researcher at the Energy Harvest Storage Research Center (EHSRC, Department of Physics, University of Ulsan). His research interests include micro–nano material synthesis techniques, physical properties of vanadium oxides, and other metal oxide semiconductor materials. He also has interests in micro–nano applications in photocatalysis, solar cells, and chromogenic, optoelectronic, and thermoelectric devices.

Phuong V. Pham

Phuong V. Pham is a Distinguished Research Fellow at the School of Micro-Nano Electronics, Zhejiang University, China. He earned his PhD degree in SKKU Advanced Institute of Nanotechnology (SAINT), Sungkyunkwan University (SKKU), South Korea (2016). He then has spent a few years as a Postdoctoral Researcher and a Research Fellow at the School of Advanced Materials Science and Engineering, SKKU, and at the Center for Multidimensional Carbon Materials (CMCM), Institute for Basic Science (IBS), South Korea, respectively. He is a recipient of the NSF Career Award of China for excellent young scientists. His research interests include low-dimensional materials, 2D material synthesis, new doping technique development, nanocomposites, block copolymers, plasma engineering for OLEDs, transistors, sensors, photodetectors, flexible displays, and wearable electronics.

Chung-Li Dong

Chung-Li Dong has a PhD in Physics (2004, Tamkang University, Taiwan) and conducted postdoctoral research at the Institute of Physics, Academica Sinica, Taiwan, and at the Advanced Light Source, Lawrence Berkeley National Laboratory, the USA from 2005 to 2009. From 2009 to 2015, he was a scientist at the National Synchrotron Radiation Research Center (NSRRC) in Taiwan. He is now an Associate Professor at the Department of Physics, Tamkang University. His research focuses on synchrotron-based in situ/operando spectroscopic studies of advanced and energy materials.

Naoufal Bahlawane

Naoufal Bahlawane is a lead research and Technology Associate at Luxembourg Institute of Science and Technology. He received his PhD (1998) in materials science from Lyon 1 University in France and was awarded JISTEC and Alexander von Humboldt Fellowships in Japan and Germany. He received a habilitation (venia legend) in Physical Chemistry at Bielefeld University in Germany. His research activities are related to the surface chemistry and the interplay between the structure–properties and surface reactivity of materials.

chromogenic research of TMOs highlights several materials, including WO_3,[20] VO_2,[21–23] TiO_2,[24] MoO_3,[25] and NiO.[26] Among them, WO_3 has been studied extensively for EC applications (Fig. 1A); VO_2 has been studied extensively for TC applications for smart windows. Chromogenic V_2O_5 has attracted less attention.

Several review articles have focused on the battery applications of V_2O_5 because of its layered structure.[27–32] Nevertheless, no review articles have addressed the optical properties, chromic phenomena, and applications or reported the influence of V_2O_5 micro–nano structures, dopants, micro–nanocomposites, and hybrid materials to enhance the performance of V_2O_5-based actual applications. Despite this, V_2O_5 has attracted considerable attention owing to its promising applications based on its multifunctional properties, as shown in Fig. 1B. Its electrochemical properties, i.e., energy storage,[30,31] electrochemical systems,[32] and supercapacitors,[33,34] have received most attention owing to its layered structure. On the other hand, less emphasis has been placed on the applications of its optical characteristics, such as photocatalysis,[35] photodetectors,[36] solar cells,[37] light-emitting diodes,[38] and waveguides.[39] The number of publications on chromogenics[16,40] and gas-sensor[41,42] applications of V_2O_5 is quite modest. Other applications, e.g., thermoelectrics,[43] field-effect transistors,[44] magnetization,[45] ferromagnetism,[46] field emission,[47] mechanical properties, and electromechanical actuation[48] have also been investigated.

The various oxidation states of vanadium (V^{2+}, V^{3+}, V^{4+}, and V^{5+}) allow the existence of many oxides and form the ground for rich chemistry and physics. Multiple oxide phases include VO, V_2O_3, VO_2, V_2O_5, and mixed phases, such as the Magnéli phase V_nO_{2n-1} (V_3O_5, V_4O_7, V_5O_9, V_6O_{11}, and V_7O_{13}), and the Wadsley phase V_nO_{2n+1} (V_3O_7, V_4O_9, V_5O_{11}, V_6O_{13}, V_7O_{15}, and V_8O_{17}).[49,50] Several vanadium oxides feature structure-driven properties, and some of them exhibit strong sensitivity to external stimuli.

Dimitra Vernardou

Dimitra Vernardou received her PhD in Physical Chemistry from the University of Salford in 2005. During her PhD, she designed, optimized, and demonstrated an APCVD reactor to grow VO_2 and V_2O_5 coatings as thermochromic and electrochromic layers. She is currently an Assistant Professor in the Department of Electrical & Computer Engineering of Hellenic Mediterranean University. Important research targets of her group (https://cuttematerials.hmu.gr/) include the development and characterization of materials as electrodes within advanced manufacturing for battery and electrochromic devices.

Issam Mjejri

Issam MJEJRI received his PhD in Materials Chemistry from Tunisia University in 2015. He joined the CNRS (Bordeaux, France) as a researcher in 2016 to work on the synthesis and characterization of the micro/nano material-based transition metal oxides and study their X-chromic properties. His main research interest is to provide a comprehensive view of the coloration mechanism in chromogenic materials. He also has interest in investigating the relationship between the structure, morphology, and electrochemistry of novel transition metal oxides as positive electrodes for rechargeable Li-ion batteries and Na ion batteries.

Aline Rougier

Aline Rougier received her Ph. D in 1995 from the University of Bordeaux. She is currently a senior CNRS researcher at the Institut de Chimie de la Matière Condensée de Bordeaux, ICMCB. Her expertise as Solid-State Chemist and Materials Scientist is in inorganic materials for energy storage and energy conversion applications. Her main topic is the study and optimization of electrochromic materials as powders or films, from the deep investigation of their optical and electrochemical properties to their integration in devices for applications in the visible and infrared regions.

Sok Won Kim

Sok Won Kim received his BS in Physics Education from Seoul National University (1982) and his MS and PhD degrees in Physics from KAIST (Korea Advanced Institute of Science and Technology) (1987). He is currently a professor of physics with the University of Ulsan and President of the Korean Society of Thermophysical Properties. His research interests includ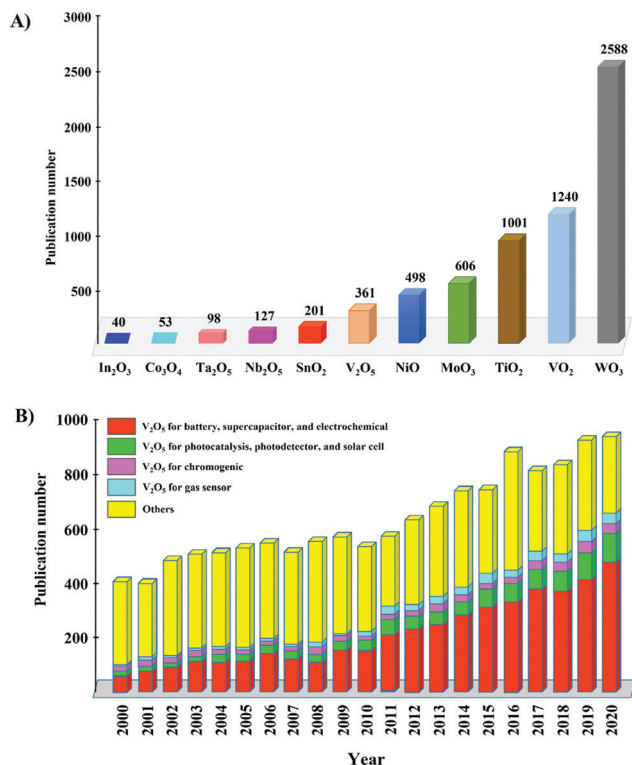e measurement of the physico-chemical properties of vanadium oxides (V_2O_5 and VO_2) and other metal oxide semiconductor materials. He also has interest in measuring the thermophysical properties of solids, films, and liquids using optical techniques.

Fig. 1 Number of publications (A) on chromogenics of metal oxides and (B) on V_2O_5 from 2000 to 2020. Source: ISI Web of Science, access date 2021-05-01.

These smart multifunctional materials are appealing for various applications, including energy saving and energy conversion. Among the various oxide phases, at standard temperatures and pressures, V_2O_5 is thermodynamically the most stable and exhibits outstanding optical and electrochemical properties.

V_2O_5 is toxic to cells, but recent studies have shown that a surfactant of nanosized V_2O_5 is a promising candidate for use in biology and medicine.[51–55] The warning toxicities reported in the U.S National Library of Medicine show that V_2O_5 is harmful if swallowed or inhaled and may cause respiratory irritation.[56] Nevertheless, V_2O_5 micro–nanostructures can act as nanoisozymes and naturally occurring vanadium haloperoxidases in specific biological and anti-biofouling agents.[51,52] Nanoscale V_2O_5 can also mimic an enzyme cascade reaction because of its intrinsic peroxidase and glucose oxidase-like activity.[53,54] V_2O_5 has been applied to selective colorimetric methods to detect glucose and fully restore the redox balance inside biomolecules. V_2O_5 NWs can act as a tandem nanozyme based on the absorption of the V_2O_5 surface that can be applied to the continuous monitoring of glucose.[55]

Many synthesis methods have been used to engineer V_2O_5 micro–nano devices for applications in CDs with enhanced performance in coloration. Improving the coloration efficiency and switching time of smart V_2O_5 micro–nano films with different morphologies, such as NFs,[57] NRs,[58] NWs,[59,60] and nanopores,[61] has been a major focus. Improvement in optical properties is reported by doping with metals and rare earth elements, hybridized structures, and composites. Nevertheless,

there have been no reviews published in this area. Understanding the fundamentals and the influence of micro–nanostructures, elements, dopants, and composite structures on the physical and chemical properties and morphologies of V_2O_5 is very important for enhancing the coloration efficiency of CDs. Thus, this general review presents the fundamentals, progress, and applications of chromogenic V_2O_5.

2. Structure and morphology of V_2O_5

2.1 Crystal structure

Depending on the growth conditions, polymorphic phases including α-, β-, ε-, δ-, γ-, ζ-, and ω-phases were reported in V_2O_5 crystals. Among them, the α-V_2O_5 phase is the most stable, while other metastable V_2O_5 phases or the mixed phases can be formed by a transition from α-V_2O_5 at high temperatures, high pressures, or electrochemical operation.[29,62–68] Moreover, α′-, ε′-, δ′-, γ′-, ζ′-, and ω′-V_2O_5 are obtained by deintercalation, *i.e.*, complete removal of the metal ions (*e.g.*, M = Li, Zn, Al, and Mg) from α-, β-, ε-, δ-, γ-, ζ-, and ω-$M_xV_2O_5$.[63] Section 5.2.1 presents the detailed phase transition α ↔ ε ↔ δ ↔ γ ↔ ζ ↔ ω by the deintercalation of V_2O_5.

For forming a pure α-V_2O_5 phase without an electrochemical process, some of the phase transitions from the α phase, such as β-, δ-, γ-, and ζ-phases, occur as a function of pressure or temperature, while other phases are difficult to form.[62,64,66,67] The energy required for the diffusion of O and V ions at low temperatures and pressures is sufficient to produce α-V_2O_5, and it can be converted into β- and δ-V_2O_5 structures or mixed phases at high temperatures/high pressures.[67] These transitions were observed at 5.3 GPa (from α- to β-V_2O_5) and at 9.5 GPa (from β- to δ-V_2O_5).[66] The energies required to convert α-bulk into β- and γ-V_2O_5 bulk are 14.2 and 10.6 kJ mol^{-1}, respectively. The formation energy of the γ-, α-, and β-layer from α-bulk is 20.7, 19.9, and 17.9 kJ mol^{-1} while that needed to convert the α-layer into the γ-V_2O_5 layer is 0.8 kJ mol^{-1}.[65]

The stable structure of α-V_2O_5 corresponds to a layer-like structure with the D_{2h}-P*mmn* space group with the lattice parameters of a = 11.51 Å, b = 4.37 Å, and c = 3.56 Å.[50,69–71] α-V_2O_5 is formed by shared edges and corners of VO_5 pyramids to form zigzag lamellar sheets along the [010] direction.[72] The metastable phases of V_2O_5 are derived from the puckering, sliding, and expanding of the layers, and interface of layers or the rotations of two edges share (VO_5) square pyramidal units.[29,73,74] Table 1 lists the lattice parameters of the various phases. Note that lattice parameters a, b, and c depend on the coordination denoted.

Fig. 2A presents the α-V_2O_5 crystal structure and three views of the (001), (001), and (100) surfaces.[75] The primitive cell of atomic structure includes three oxygen centers bonding with vanadium: terminal O(1)–V = 1.58 Å, bridging O(2)–V = 1.78 Å, and bridging O(3)–V = 2.02 Å.[50,69–71]
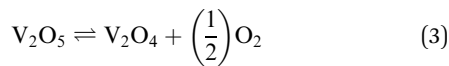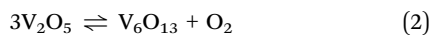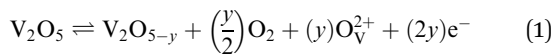
The ε-, and δ-phases correspond to the expanded α-phase, so they feature similar atomic structures.[76] Indeed, the edge-sharing distorted VO_6 octahedra of ε- and δ-V_2O_5 are connected

Table 1 Lattice parameters of various V_2O_5 phases

| Phase types of V_2O_5	Method	Lattice parameters (Å)			
		a	b	c	Ref.
α-phase	DFT	11.627	3.577	4.538	62
	Exp. pure V_2O_5 powder	11.523	3.562	4.330	77
	Exp. α-$Li_{0.0625}V_2O_5$	11.5121	3.5701	4.3737	335
β-phase	DFT	7.440	3.571	6.368	62
	Exp. pure V_2O_5 NPs	7.1216	3.5720	6.2882	62
	Exp. β-$Li_{0.3}V_2O_5$	15.288	3.7321	9.604	336
ε-phase	PBE + U	11.720	3.686	9.541	74
	Exp. pure V_2O_5 NRBs	11.65	3.68	13.5	337
	Exp. ε-$Li_{0.6}V_2O_5$	11.40	3.56	4.53	338
δ-phase	GGA	11.9974	4.7041	5.4169	77
	Exp. pure V_2O_5 powder	11.9719	4.7017	5.3253	66
	Exp. δ-LiV_2O_5	11.20	3.56	9.91	338
γ-phase	Hybrid DFT and HF	10.055	3.565	10.042	65
	Exp. pure V_2O_5 NRs-NWs	9.946	3.585	10.042	68
	Exp. γ-LiV_2O_5	9.64	3.60	10.60	338
ζ-phase	PBE + U	15.586	3.666	10.269	74
	Exp. pure V_2O_5 NWs	15.275	3.604	10.098	153
	Exp. ζ-$Li_2V_2O_5$	9.08	3.60	10.24	339
ω-phase	DFT	9.21	9.13	3.95	340
	Exp. ω-$Li_{0.4}V_2O_5$	9.17	9.17	4.09	341
	Exp. ω-$Li_{2.65}V_2O_5$	9.21	9.21	4.09	341

by the corner O(1) to form layers with weak V–O(3) and V–O(2) interactions.[63,74,77] For the γ-phase, oxygen forms five bonds with two types of vanadium cations resulting in a configuration with two different apex-connected VO_5 pyramids.[65,68,78] The β-phase features five nonequivalent oxygen atoms bonded to two octahedrally coordinated vanadium atom types.[62,65] The ζ-phase is formed by three distinct vanadium-centered polyhedral that share and connect with eight oxygen atoms.[74]

Fig. 2B shows the top view of the vacancies on the (010) surface. Oxygen vacancies can be formed due to the removal of O(1), O(2), or O(3), as expressed in eqn (1)–(3). Goclon *et al.*[75] compared the formation energy of oxygen vacancies of the (100), (010), and (001) surfaces. In equilibrium, the energy required to form oxygen vacancies on (100) and (001) was 1.0–1.5 eV lower than that on (010), despite the (010) surface comprising approximately 85% of the total surface area of the crystal.

$$V_2O_5 \rightleftharpoons V_2O_{5-y} + \left(\frac{y}{2}\right)O_2 + (y)O_V^{2+} + (2y)e^- \quad (1)$$

$$3V_2O_5 \rightleftharpoons V_6O_{13} + O_2 \quad (2)$$

$$V_2O_5 \rightleftharpoons V_2O_4 + \left(\frac{1}{2}\right)O_2 \quad (3)$$

2.2 Morphologies of V_2O_5 and synthesis methods

2.2.1 Morphologies of V_2O_5. Various morphologies were fabricated using different synthesis methods that bring promising applications. V_2O_5 gels were first synthesized from NH_4VO_3 salt in 1885.[79] Thus far, considerable efforts have been made to improve the physical and chemical properties of V_2O_5, including the synthesis of various structures, such as 0D, 1D, 2D, and 3D structures. Fig. 3 shows a schematic diagram of the mechanisms to form different morphologies that depend on the growth conditions based on the bottom-up approach mechanism. At
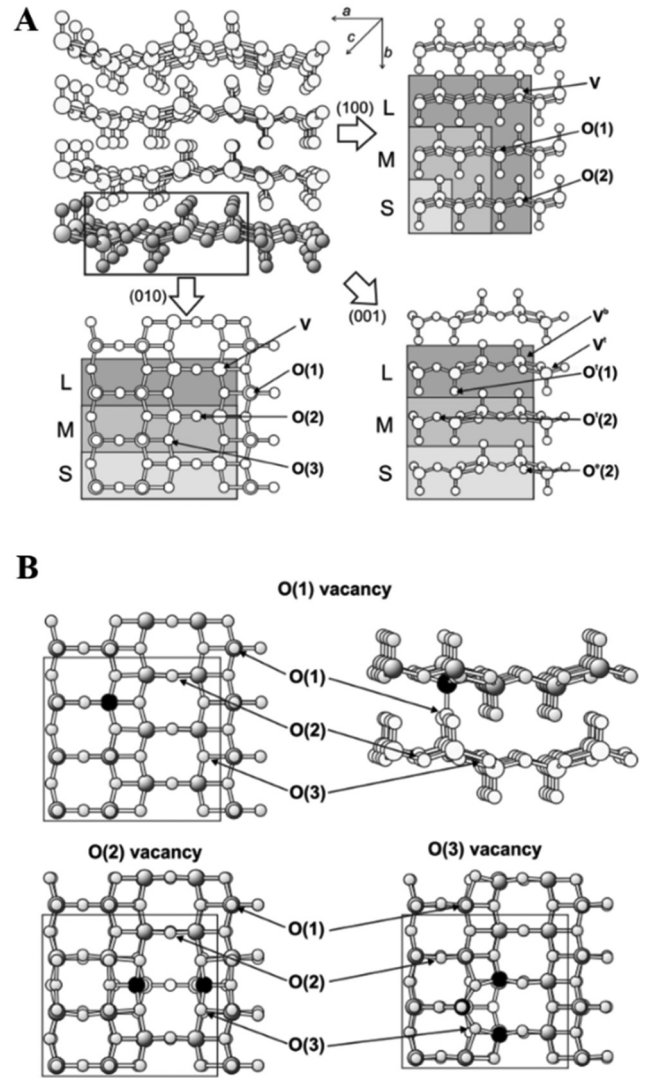
Fig. 2 α-V_2O_5 crystal structure and oxygen vacancies: (A) Perspective view and top view along the (010), (001), and (100) surface directions, and (B) top view of vacancies on the (010) surface with the O(1) site, O(2) site, and O(3) site, reproduced with permission (Copyright 2022, American Physical Society[75]).
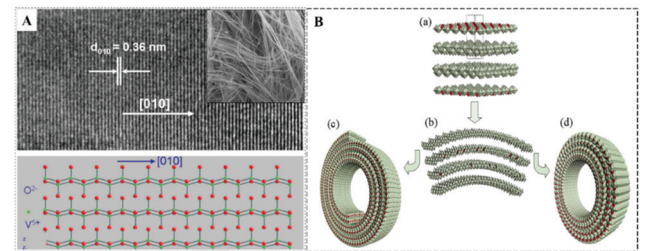
Fig. 3 Schematic diagram of the mechanism of formation and TEM images of V_2O_5 morphologies: (A) TEM image and atomic model of NW and (B) atomic model of NT. The figures are reproduced with permission (Copyright 2022, Wiley[47] and American Physical Society[81]).

the beginning, a small cluster or small crystallites were formed, which coalesced to form larger crystallites, and grain boundary

diffusion at the surface was boosted to form morphologies, such as NPs, NWs, and NSPs. The formation process depends on the growth of preferential orientation of molecules and clusters. Owing to the formed layer and the layer by the vdW force (the vdW gap is approximately 4.4 Å), the V_2O_5 growth takes place preferentially along the [001] orientation with a layered structure because of the lowest surface energy of the (010) plane.[75,80] The interlayer distance d (Å) and tangent angle ($\alpha°$) between the layers play an important role in determining the dimensionality structure.

For $\alpha = 0°$, V_2O_5 grows and extends in one or two orientations (Fig. 3A) to form 1D structures, such as NWs,[47] NFBs,[37] and NRs,[82,83] or 2D structures, such as ultra-large NSHs,[84] and sponge-like structures from 2D NSHs.[85] In the hydrothermal and solvothermal processes, the formation and growth of 1D or 2D materials can be based on Ostwald Ripening and Oriented Attachment growth mechanisms.[86] The pre-solution, temperature, and time reaction affect the reaction speed, activating crystal, and surface diffusion mobility. 1D and 2D V_2O_5 structures were self-assembled from nucleation or original vanadate, such as $(VO_2)^+$ and VOOH.[85,87] Micrometer-, centimeter-, and ultra-long NWs, NFBs, NSPs, and NRs were formed as a result of a continuous process in a long-term reaction.[37,47,59,60,88–91] Similarly, this process can lead to the diameter increase or assembly of NWs and NFBs to form NBs.[86,92,93] The bent layers (for $\alpha = 90°$) may form nanoscrolls, NHLs, or closed NTs, as shown in Fig. 3B.[81,94,95] In the vapor deposition and electrodeposition processes, the thin films were formed via nucleation and the expanded growth mechanism.

For $\alpha = 30°$ or $45°$, the growth in multiple directions co-occur, resulting in the formation of compact of 0D V_2O_5, such as QDs with average diameters of 3 nm,[96] 2–3 nm,[97] 5–8 nm,[98] and 30–50 nm,[35] or 3D V_2O_5, such as flower-like arrays,[99] porous hierarchical octahedra, and microspheres.[100,101] In wet chemical reactions and solvothermal processes, nucleation and growth occurred to form particles. These particles grow or attach and self-aggregate to form larger particles or 3D V_2O_5 depending on precursors, concentrations, or reactants. However, due to preferential orientation along the [001] orientation, the direct synthesis of 0D V_2O_5 via the bottom-up method requires optimal conditions in terms of reaction rate, time, and temperature. The 0D VO_x or vanadium-containing precursors ($V(OH)_2NH_2$ and VOOH) were commonly fabricated before being annealed in oxygen to form 0D V_2O_5.[32] Annealing temperature also improves crystallinity, changes the crystal phase (i.e., from α- phase to other phases), and alters the morphology (i.e., from 0D to 1D).

Diverse 0D, 1D, and 2D V_2O_5 micro–nanostructured morphologies of various sizes have been separated from bulk V_2O_5 using the top-down technique. Mechanical shaking (ultrasonication), high-energy collision (ball milling process), or high-temperature treatment (by pulsed laser ablation or melting) was used to divide 3D V_2O_5 to lower dimensions. As illustrated in Fig. 4A, bulk V_2O_5 was exfoliated to layer 2D using an ultrasonication process. Fig. 4B shows the production of compact and hollow NPs (0D V_2O_5) from solid V_2O_5 pellets
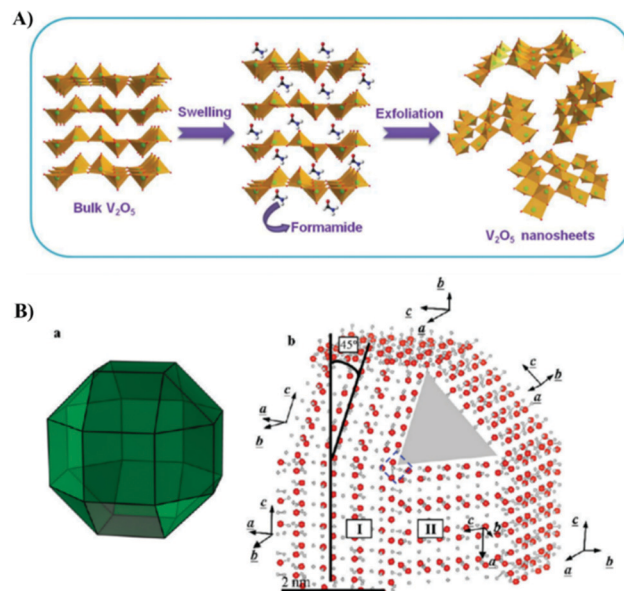

Fig. 4 Schematic diagram of the top-down formation mechanism of lower dimensions: (A) 2D and (B) 0D. The figures are reproduced with permission (Copyright 2022, American Chemical Society[102,103]).

using the PLA technique. Bulk V_2O_5 is ablated by the incident laser beam, forming a plume which is then deposited on the substrate.

2.2.2   Synthesis method. Different methods have been used to fabricate V_2O_5[50] with multiple morphologies, including bottom-up methods, top-down methods, and combined methods.

2.2.2.1 Bottom-up methods

(i) Physical vapor deposition (PVD). This technique is used to grow thin films under high vacuum, usually using plasma, laser, and heat to sputter or sublime a target material with the appropriate composition.[50] The inlet gas composition, pressure, substrate temperature, and substrate types are the main factors affecting the structure and physical properties of the grown V_2O_5 films. The PVD methods used to grow different V_2O_5 morphologies are PLD,[104] EBE,[105,106] RF-sputtering,[107,108] DC-sputtering,[109,110] IB-sputtering,[111] and RFRP.[112]

Thiagarajan et al.[105] reported the influence of the nature of the substrates on morphology. The films exhibited very densely packed particles with a smooth surface (glass and ITO substrates) and different particle sizes with rough surfaces (Al, Cu, and FTO substrates). Kang et al.[106] examined the effects of the beam dose rate irradiation (EBE method) on the morphology and crystal structure. The rod-like morphologies appear at dose rate irradiation of 300–600 kGy with a buffer layer while the film was amorphous at 0–600 kGy without a buffer layer; V_2O_5 NRs were obtained at 800–1000 kGy in both cases.

(ii) Chemical vapor deposition. This technique including CVD,[113–116] AP-CVD,[117] LP-CVD,[118] AL-CVD,[119] MO-CVD,[120] PE-CVD,[121] and AA-CVD[122] is based mainly on the vapor phase reaction-adsorbed precursors (i.e., $VO(acac)_2$, $V(C_5H_8O_2)_3$, and

VO(OC$_2$H$_5$)$_3$) on the substrate surface.[50] The reaction temperature, O$_2$ source, reaction time, and sample position are factors that play an important role in controlling the morphology, crystal structure, and surface of the thin film.[50,113]

Among these factors, the deposition temperature is used to control the morphology and thickness of the film. When the deposition temperature was increased from 320 °C to 420 °C for the same duration, the length of V$_2$O$_5$ NWs increased from 10 μm to 100 μm while the widths remained approximately 80 nm.[116] The deposition temperature in the range of 500–700 °C significantly influences the porous morphology, surface, and size of the film, whereas different NP sizes of 15, 60, and 30 nm were obtained at 900, 1100, and 1300 °C, respectively.[113] Yin et al.[114] examined the influence of the substrate temperature on the surface roughness of 1D porous V$_2$O$_5$ micro–nanotubes. The surface changed from porous (at 220 °C) to much less porous (at 260 °C) and smooth (at 320 °C). Musschoot et al.[123] compared the influence of thermal and plasma-enhanced (PE) ALD/CVD on V$_2$O$_5$ films. The as-grown films deposited by CVD at 300 °C and PE O$_2$ ALD at 150 °C were crystalline with 001-oriented V$_2$O$_5$, whereas the as-grown films deposited by thermal and PE H$_2$O ALD at 150 °C were amorphous.

(iii) Solution method. Solution methods, including WCR,[35] hydrothermal,[47] CBD,[124] sol–gel,[30] ECAD,[125] ESS,[126] ED,[67] TP,[127] SP,[128] and ESP,[36,129,130] are used widely to synthesize nanostructures. Among these solution methods, WCR and hydrothermal methods are used widely because of the simple processing and low cost. Sukanya Datta et al.[131] reported various morphologies of nanostructured V$_2$O$_5$, such as 3D microbeads, 2D NSHs, and 1D nanofleeces using different deep eutectic solvent relines. Mu et al.[132] controlled different morphologies, NFLs, nanoballs, NWs, and NRs, using different pre-solutions (acid-solvents), such as H$_2$C$_2$O$_4$–C$_2$H$_5$OH, HNO$_3$–C$_2$H$_5$OH, HNO$_3$–H$_2$O, and H$_2$C$_2$O$_4$–H$_2$O, respectively. Wang et al.[133] prepared V$_2$O$_5$ NWs and NSHs with different growth times. For short reaction times, V$_2$O$_5$•nH$_2$O sheets were synthesized, while NWs were obtained after extended reaction times.

2.2.2.2 Top-down methods. Bulk V$_2$O$_5$ is converted to small nano-sized particles or sheet-layers using physical and chemical treatments, such as mechanical dynamic, thermal, etching-reaction, laser ablation, and ultrasonication.[134] These methods can be used to fabricate high purity NPs, but they are unsuitable for preparing uniform-shaped particles. Top-down methods have been reported to prepare abundant morphologies of V$_2$O$_5$, such as TE,[60] MQ,[135] TD,[136] ultrasonication (liquid exfoliation),[102] PLA,[80,137] dissolution–splitting,[138] and BM.[139,140] Díaz-Guerra et al.[136] examined the influence of the treatment duration on morphology using the TD method. Micro-rods, urchin-like structures, and nanotips were formed during annealing under Ar at 700 °C for 10 and 15 h. Rui et al. obtained ultrathin V$_2$O$_5$ NSHs with lateral dimensions of 100–400 nm by sonicating V$_2$O$_5$ powder at RT for three days.[102] Zou et al.[140] used the BM method, adding H$_2$C$_2$O$_4$ to prepare V$_2$O$_5$ NPs of various sizes based on different milling times. After three hours of grinding, the powder particle size decreased

from 500 to 40 nm. Taylor et al.[137] prepared "nearly spherical" α-V$_2$O$_5$ NPs with sizes below 100 nm and "flower-like" β-V$_2$O$_5$ NSs with a micrometer size by irradiating bulk vanadium flakes immersed in DI water with a Nd:YAG laser. The surface morphologies were also controlled using different Nd:YAG laser treatments from vanadium sols.[141]

2.2.2.3 Combined methods. Various V$_2$O$_5$ morphologies have been studied extensively using a combination of different methods, such as MQ-hydrothermal,[86] WCR-hydrothermal,[84,95] LASP-sol–gel,[141] and UV irradiation-sol–gel.[142] Mesoporous ultra-large V$_2$O$_5$ NSHs were synthesized by combining WCR and hydrothermal methods.[84,143] V$_2$O$_5$ NWs, 50–100 nm in diameter and up to several micrometers in length, were prepared using the MQ method by heating V$_2$O$_5$ powder at high temperatures (800 °C) and quickly pouring the powder into water with vigorous stirring and autoclaving the solution at 200 °C for four days.[144] Ultralong NBs with widths in the range of 30–200 nm were formed by heating the powder at 850 °C and heating a solution containing the heated powder at 220 °C for a few days.

Recently, the combination of many techniques was used to fabricate different morphologies, such as NTLs, NTs, NPRs, NHLs, and nanobox.[33,145–151] In these combinations, the V$_2$O$_5$ layer is deposited on substrates with different mask types as prepared previously. Chen et al.[146] and Liu et al.[147,148] grew V$_2$O$_5$ layers on anodic aluminum oxide (AAO) using the ALD method. The results showed that the size of the NTLs and NTs depends on the AAO pore diameter and the number of deposition cycles. The NPRs with different pore diameter sizes were prepared in two steps: (1) PS spheres with different diameter sizes were used to fabricate the monolayer or multilayers colloidal crystal templates; and (2) a V$_2$O$_5$ film was deposited into colloidal crystal templates using the ED or ECAD method and the PS spheres were then removed.[145,149,150]

In another study, multi-shelled V$_2$O$_5$ hollow microspheres were controlled by a repeated adsorption process of vanadium precursor on carbonaceous microspheres (CMSs).[33] The hydrothermally synthesized CMSs were dispersed in a solution containing a vanadium precursor (NH$_4$VO$_3$) by ultrasonication for 10–30 min and kept in a water bath at 40–70 °C for 6 h. Both metal cations and metal anions were adsorbed by CMSs to form CMS/vanadium oxide composite spheres. The resulting composites were annealed at 400 °C for 30 min to obtain hollow spheres. The different hollow spheres, including double-, triple-, thick single-, porous triple-shelled, and multi-cavities, were obtained easily by repeating the adsorption process several times and stirring in different acidic aqueous solutions. Similarly, Liu et al. obtained V$_2$O$_5$ multi-scale hierarchical boxes after 2 h air-annealing at 500 °C of an autoclaved (12 h at 200 °C) solution mixture containing vanadium oxytriisopropoxide and carbon hollow cubes.[33]

The morphology of the V$_2$O$_5$ micro–nanostructures can be controlled by a combination of post-annealing of the films obtained *via* solution, CVD, and PVD processes. Specifically, the shell number of V$_2$O$_5$ was controlled by heat treatment of NSPs.[152] Double-shell hollows were formed by annealing a solid sphere at 350 °C obtained by solvothermal synthesis. Single-

shell NHLs were obtained after annealing at 450 °C while double-shell NHLs were formed after annealing at 350 °C.[152] Similarly, single, double, or multi-shelled hollows can also be controlled by heat treatment at different temperatures.

Different types of 1D V_2O_5 nanostructures, including NTs, NFBs, and NRs, were formed by annealing electrospun NFBs at 400, 500, and 600 °C, respectively.[129] The as-deposited V_2O_5 film grown by the ED method had a smooth surface and became a rod-like structure as the annealing temperature was increased from 400 to 500 °C. When annealed at higher temperatures (550–650 °C), the rod-like structure of V_2O_5 tends to form long-rods due to the high diffusion rate on the surface and becomes stream-shaped slices.[67] Different scales of the belt-like NRs were formed by annealing the V_2O_5 powder formed from the MB method at 630 °C for different durations.[139]

3. Bandgap and optical transition

3.1 Bandgap

Fig. 5 compares the V_2O_5 electron structural density of states between α- and γ-,[78] α- and β-,[62] and α- and ζ-phases.[153] No experimentally or computationally determined bandgaps of pure ε- and ω-V_2O_{5-y} have been reported.

Pure V_2O_5 is an n-type direct/indirect gap semiconductor.[69,154–156] The electronic structure of V_2O_5 is rather complicated and depends on the morphology, number of oxygen vacancies, and crystal phase.[50] At RT, α-V_2O_5 bulk has a direct bandgap of approximately 2.3–2.4 eV and an indirect gap of approximately 1.9–2.0 eV. The VB widths were 5.5 ± 0.5 eV (bulk) and 5.0 ± 0.5 eV (single-layer).[69] Rather than being a single band, the CB is made up of two bands, with a main CB and a split-off CB.[154,157] These split-off

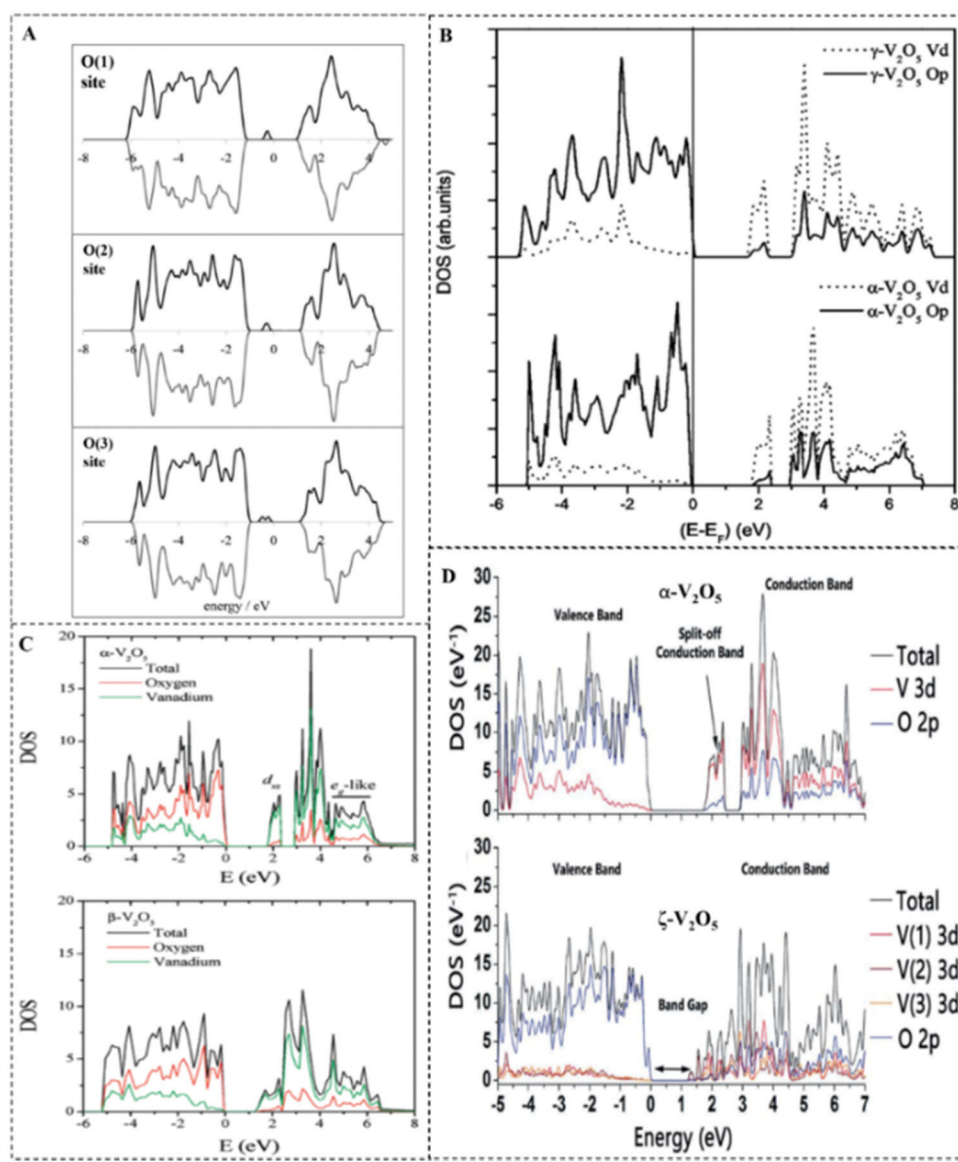Fig. 5 Comparison of the density of states (A) between the O(1) site, O(2) site, and O(3) site of α-V_2O_{5-y}, (B) between α-V_2O_5 and γ-V_2O_5, (C) between α-V_2O_5 and β-V_2O_5, and (D) between α-V_2O_5 and ζ-V_2O_5. The figures are reproduced with permission (Copyright 2022, American Chemical Society,[159] American Physical Society,[62,78] and Royal Society of Chemistry[153]).

CBs have a bandwidth of 0.75 eV and are localized at 0.6 eV below the main CB.[136,154,158]

Oxygen vacancy-induced V_2O_{5-y} leads to changes in the atomic, crystalline, and electronic structures.[159,160] When oxygen atoms are removed from the lattice, the electrons are left behind. The V–O bonding in the crystal changes because of the regulated atomic structure and hybridized V 3d-O 2p.[50] Consequently, the geometric structure is altered and forms mid-gap states and surface states. Scanlon et al.[159] calculated the delocalized defect electronic states in V_2O_{5-y} using gradient-corrected DFT on-site Coulomb interactions (GGA+U). The results revealed the appearance of mid-gap at approximately 0.7–1.0 eV above the VB due to oxygen vacancies. The experimental results revealed this gap at approximately 1.8 eV above the VB.[118] The mid-gap states due to O(1), O(2), and O(3) vacancies are located at ∼0.95, 0.75, and 0.69 eV, respectively, as shown in Fig. 5A.

As shown in Table 1, these phases of crystal and electronic structures are similar because there is little difference between the lattice parameters and the unit cell volumes of α-V_2O_5, ε-V_2O_5, and δ-V_2O_5. Therefore, the band gaps of α-, ε-, and δ-V_2O_5 are homologous. Although the space group and unit cell parameters of γ-V_2O_5 are different from those of α-V_2O_5, γ-V_2O_5 retains similar structural features.[65] The main CB of γ-V_2O_5 was also separated to form a split-off band. The shape, width of split-off CB, and narrow gap from main CB and split-off CB of γ-V_2O_5 were similar to those of α-V_2O_5, as shown in Fig. 5B.[65,78] On the other hand, this split-off was not observed in β- and ζ-V_2O_5, while the gaps of β- and ζ-V_2O_5 were narrower than those of α-V_2O_5 (Fig. 5C and D).[62,65,161]

3.2 Optical transition

The theories and experiments showed that the optical bandgap (E_{opt}) and transition intensity between the bands in V_2O_5 were affected by many factors.[50] The special band structure of V_2O_5 leads to a peculiar smart optical transition. In pure β- and ζ-V_2O_5, there is one optical transition only (VB ↔ CB), while two optical transitions (VB ↔ main CB and VB ↔ split-off CB) are present in pure α-, ε-, δ-, and γ-V_2O_5. In particular, in pure α-V_2O_{5-y} with three bands, four optical transitions (VB ↔ main CB, VB ↔ split-off CB, VB ↔ mid-gap state and surface state, mid-gap state ↔ main CB) may occur. Therefore, in the literature, the E_{opt} and PL position of V_2O_5 do not coincide. Table 2 lists some articles on the

Table 2 Optical bandgap and photoluminescence peak position of different V_2O_5 morphologies

Morphology	Parameter note	Synthesis method	E_{opt} (eV) determined from UV-vis spectroscopy	Excitation wavelength source for PL measurement (nm)	PL peak position (nm)	Ref.
0D V_2O_5	Spherical-like NPs of diameter size in range 10–15 nm	WCR	2.12	475	502	172
	NPs with a perfectly spherical shape of average diameter in the range 5–8 nm	WCR	2.92	380	460, 593	98
	NPs of average diameter 96.5 nm with roughness 1.926 nm (2D) and 3.46 nm (3D)	Sol–gel	3.27	325	382, 397, 450, 469, 530, 557	171
1D V_2O_5	NWs with an average diameter of 50 nm and length of many tens μm	LPCVD	2.74	266	450, 690	118
	NWs with 30 nm in diameter and several tens of micrometer in length	Hydrothermal	2.16, 2.30	< 350	579, 687.5	174
	NWs with an average diameter of 80 nm and length of 10–100 μm	CVD	2.48	365	350–700	116
	NRBs of 100–300 nm diameter and length several hundred micrometers.	Heating foil	2.30	457	550–750	39
	NBs of 50–70 nm diameter and lengths of several tens of microns.	Hydrothermal	2.02	—	571, 634	259
	NFBs of 20–150 nm diameter and length several micrometers.	Hydrothermal	2.20	—	504, 540, 632–647	286
2D V_2O_5	Thin film deposited on ITO substrate	PLD	2.32	—	524	173
	Thin film deposited on glass substrate at 300 °C	SP	1.99	285	475, 513, 532, 552	128
	Thin film grown on FTO substrate with average particle size of 200 nm	E-Beam	2.05	330	485, 510, 528, 545	105
3D V_2O_5	Bulk powder	Commercial	2.20	365	375	116
	Micro–nano powder	WCR	2.39	325	382, 420, 468, 550	176
	Micrometer lamellar powder	WCR	2.2	325	427–826	177
Other	morphologies	L-shaped micro–nanostructures		Hydrothermal	1.91	260
	424, other peaks		198			
	Lamellar plates	MQ	2.16	480	650, 730	342
	Flake	SP	2.05	285	475, 513, 532, 552	128
	Platelet (various dimensions)	Sol–gel	2.36	350	486, 496, 520, 553	343
Micro–nanorods		WCR	2.468	—	418, 453	344

E_{opt} and PL characterization of V_2O_5, particularly the synthesis method and morphology.

The E_{opt} or E_g of V_2O_5 is defined *via* UV-vis spectrum measurements because of the transition between the VB and split-off CB. The band edge absorption (E_{opt}) of the film has been estimated based on the Tauc or Cody plots and Tauc's law, $\alpha \nu = A(\nu - E_{opt})^n$, where, ν, A, E_{opt}, and n are the photon energy, a constant, optical bandgap, $n = 1/2$ and 2 correspond to directly and indirectly allowed transitions; $n = 3/2$ and 3 correspond to forbidden transitions, respectively.[50,162,163] Almost all reports derive an E_{opt} of V_2O_5 from the tailing absorption spectra with $E_{opt} \approx 2.3$ eV (2.2–2.4 eV). Calculation using the Perdew–Burke–Ernzerhof function results in an E_{opt} of 2.325 eV.[164] The lower or higher E_{opt} values, such as from 1.6–2.2 eV,[118,128,165–168] 2.6–3.0 eV,[98,169,170] and 3.0–3.49 eV[165,171] were reported. Similarly, optical recombination shows different PL peak positions, number of peaks, and broad emission, which are distributed over wide ranges. The differences between the PL peaks, including one peak,[116,172,173] two peaks,[98,118,174] three peaks,[175] many peaks,[128,171] and a broad peak,[39,105,116,176,177] have been observed.

4. Multicolor of the original V_2O_5 film

Optical characterization of V_2O_5 was affected by the growth parameters, element-doped V_2O_5, and V_2O_5 based on composites, leading to multi-color of the original film ("fix" chromism). Fig. 6A shows the distribution of the reports regarding the E_{opt} of V_2O_5 (survey 210 samples of 78 works). The wide distribution of the absorption and PL spectrum predicts the multicolor of "fix" and "responsive" chromic V_2O_5 ranging from dark blue to dark orange, as shown in Fig. 6B.

Fig. 7–9 reveal the existence of various absorptions and different colors of the original films. The "fix" chromic phenomena are the optical characterization of V_2O_5 materials with a fixed color production and irreversible color change. The different colors or transmitted-reflected light intensity of the film are determined before, and these films are called pristine V_2O_5 or modified-pristine V_2O_5 films. Hence, the presentation of "fix" chromism of V_2O_5 is needed to understand the fundamentals and applications of chromic V_2O_5.

4.1 Influence of the growth parameters

The fully stoichiometric phase of pure V_2O_5 exhibits orange color in optical coloration.[178] The growth conditions can change the stoichiometry of the V_2O_5 film because oxygen vacancies or other oxidation states of vanadium, sequentially, nonstoichiometric phase exhibit different colors, such as pale yellow, yellow-brown, dark green, and grayish-black.

Fig. 7A–D show the influence of ambient and temperature annealing on the color film and absorption spectra. The blue

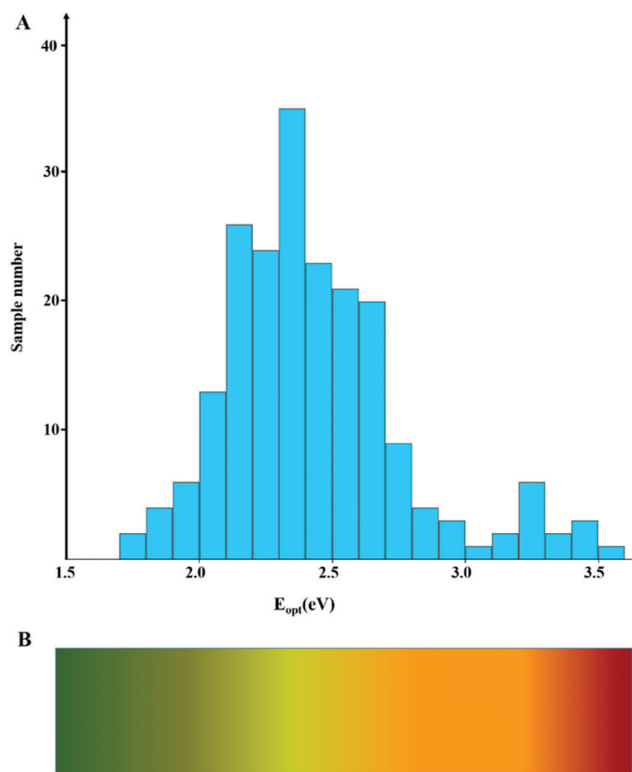**Fig. 6** Distribution of the reports on V_2O_5 optical characterization: (A) optical bandgap and (B) possible color distribution of fixed and responsive chromogenics.

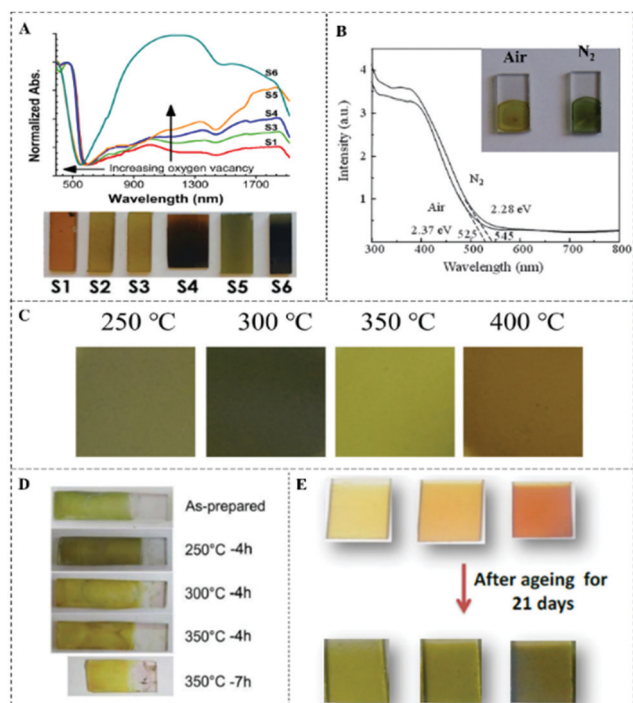**Fig. 7** Absorption spectra and photographs of V_2O_5 films: (A) with thermally induced oxygen vacancy, (B) under different annealing gas conditions, (C) and (D) at different annealing temperatures, and (E) before and after spontaneous aging. The figures are reproduced with permission, (Copyright 2022, American Physical Society,[178] Royal Society of Chemistry,[179] Elsevier,[180,181] and Wiley[83]).
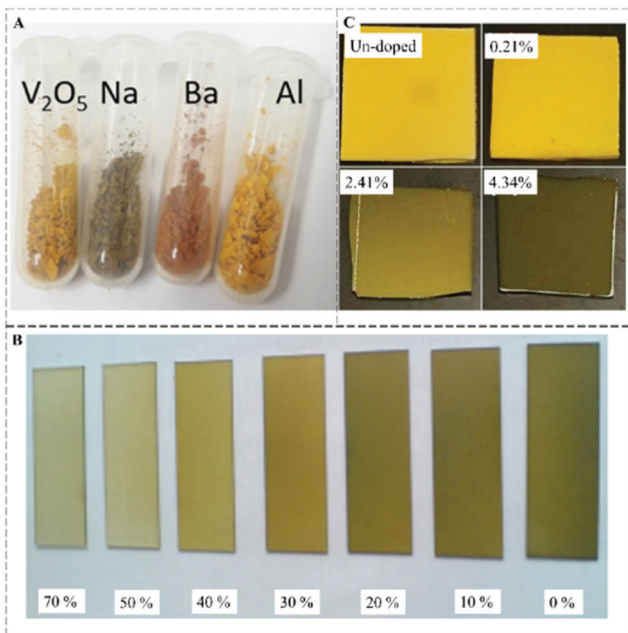
Fig. 8 Photographs of pure and doped V_2O_5 films with: (A) different dopant elements, (B) different fluorine dopant percentages, and (C) different chromium dopant percentages. The figures are reproduced with permission, (Copyright 2022, Springer,[193] Elsevier,[194] and American Chemical Society[120]).
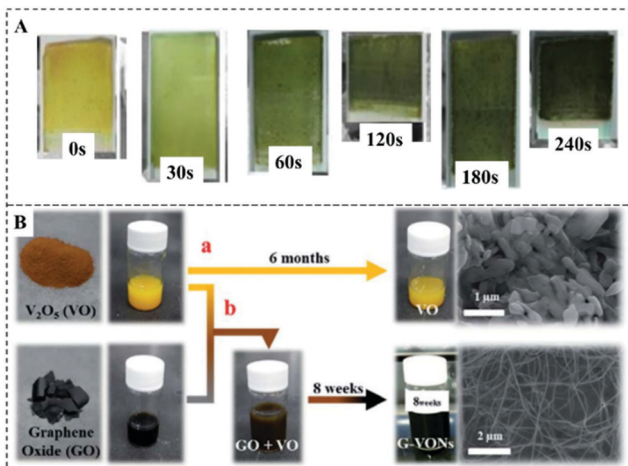
Fig. 9 Photographs of pure V_2O_5 and M@V_2O_5 composites: (A) V_2O_5/PANI composite NFs under different electropolymerization times and (B) pure and GO/V_2O_5 composite keep six months and eight weeks, respectively. The figures are reproduced with permission (Copyright 2022, Elsevier[203] and Royal Society of Chemistry[204]).

shift in the visible region, which increases in the NIR spectral range from 1200 to 1700 nm due to increasing nonstoichiometric ratio, was attributed to the increase in oxygen vacancies in V_2O_5 NWs. This leads to different film colors (S1 orange, S2 yellow, S3 dark yellow, S4 brow, S5 dark green, and S6 black, Fig. 7A).[178] The absorption spectra shift toward a longer wavelength because of the low valence state (V^{4+} and V^{3+}), when

annealed in nitrogen, which leads to a color change from yellow to dark green (Fig. 7B).[179] Oxygen vacancies also occur during the growth of V_2O_5 to form mid-gap states, which leads to an absorption shift. V_2O_5 nanostructures, including NSPs, NPs, NRs, and NWs, contain the V^{4+} oxidation state at 30.0, 4.7, 10.9, and 12.8%, respectively.[35]

The colors of vanadium oxides change due to variations of the phase evolution, structural distortion, and morphological deformation when the samples are annealed at increasing temperature and time, as shown in Fig. 7C[180] and Fig. 7D[83]). After 21 days of aging, the partial self-reduction of V^{5+} to V^{4+} was caused by the V_2O_5 xerogel acting as an acid with mobile protons and the localized electron density at the metal center. As a result, the film color changes from orange to green (Fig. 7E).[181]

The initial color of the V_2O_5 film is affected by the intensity of the optical transition leading to variations in the absorption and the transmittance spectra. The transmittance curves of the V_2O_5 film with different thicknesses and O_2/Ar ratios during the sputtering process revealed three main regions (range $300 < \lambda < 490$, $490 < \lambda < 800$, and $\lambda > 800$ nm).[182] The transition percentages of the first and third regions decrease with increasing thickness while that of the second region fluctuates. The formation of oxygen vacancies leads to increased absorption in the near-infrared region and a decrease in the optical bandgap.[183] V_2O_5 NBs exhibit different colors ranging from brownish to brilliant yellow, corresponding to a blue shift of the absorption edge with an extended reaction time from 6 h to 48 h. The films exhibit the color change when deposited at different temperatures, *i.e.*, pale yellow (RT), light brown (300 °C), and black (500 °C).[170] The color of the pristine film changes from orange → light green → orange during the annealing process.[184]

Furthermore, the E_{opt} is closely related to the color of the film; therefore, the original V_2O_5 exhibits various colors. Table 3 lists the effects of the morphology, growth conditions, dopant element, dopant concentration, composite element, and composite concentration on the E_{opt} of V_2O_5 micro–nanostructures. These factors can increase, decrease, or fluctuate the E_{opt}.

The optical band changes due to changes in the morphology originating from the precursor to the nanostructure.[185] In particular, it is affected by different substrates,[105] oxygen partial pressures,[186] precursor types,[168] precursor concentration,[187] growth times,[188] ambient annealing conditions,[179] and annealing temperatures.[167,188] The E_{opt} of films fabricated by the EBE method increases from 2.18 (840 nm) to 2.36 eV (1200 nm) or from 2.04 (oxygen partial pressure 10^{-7} mbar) to 2.30 eV (oxygen partial pressure 10^{-4} mbar) while E_{opt} decreases from 2.50 to 2.20 eV with increasing film thickness (fabricated by DC sputtering) from 110 to 450 nm.[109,186,189]

E_{opt} also changes due to non-stoichiometry and the influence of the crystallite size. E_{opt} of the film reduced from 2.47 to 2.12 eV and from 2.53 to 2.35 eV when the substrate temperature was increased from 30 to 500 °C,[104] and from 350 to

Table 3 Influence of growth parameters, dopants, and composites to the optical bandgap of V_2O_5

Typical morphologies	Synthesis method	Investigated parameter	Note	E_{opt} (eV)	Ref.
—	Different morphologies were prepared by the hydrothermal method	Different V_2O_5 nano morphologies	Precursor: 2–5 μm diameter	2.20	185
			Wire: 20–30 nm diameter	2.55	
			Rod: 30–40 nm diameter	2.55	
Film	The films were grown on glass substrates by the DC sputtering method	Film thickness (d) and crystallite size (L)	d = 110 nm, L = 17.4 nm	2.50	109
			d = 315 nm, L = 24.8 nm	2.27	
			d = 450 nm, L = 26.4 nm	2.20	
Film	The films were grown on glass substrates by the EBE method	Film thickness (d) and crystallite size (L)	d = 1200 nm, L = 31 nm	2.36	189
			d = 1100 nm, L = 35 nm	2.33	
			d = 995 nm, L = 40 nm	2.31	
			d = 910 nm, L = 45 nm	2.26	
			d = 840 nm, —	2.18	
NBs	NBs were prepared by the hydrothermal method	Diameters	52.7 nm	2.25	345
			46.3 nm	2.74	
			44.7 nm	3.00	
Film	SP	The films were deposited on the micro slide glass substrate at different substrate temperatures	300 °C	1.99	128
			325 °C	2.01	
			350 °C	2.03	
			375 °C	2.04	
			400 °C	2.05	
Film	PLD	The films were deposited on glass at different substrate temperatures	30 °C	2.47	104
			200 °C	2.22	
			400 °C	2.32	
			500 °C	2.12	
Film	CSP	The films were deposited on glass at different substrate temperatures	350 °C	2.53	190
			400 °C	2.51	
			450 °C	2.47	
			500 °C	2.35	
Film	RF Sputtering	The films were deposited on quartz with different RF powers	100 W	2.80	346
			200 W	2.40	
			300 W	2.40	
			400 W	2.60	
			500 W	2.50	
			600 W	2.60	
			700 W	2.60	
Sheet	Thermal calcinating	Pristine V_2O_5 NSHs were treated thermally in a H_2/Ar atmosphere at different temperatures for 30 minutes	0 °C	2.13	167
			250 °C	2.06	
			300 °C	1.92	
			350 °C	1.87	
Film	Sol–gel	The films were annealed at 300 °C for 3 h under different ambient conditions	Annealing in nitrogen	2.28	179
			Annealing in air	2.37	
Film	EBE	The films were deposited on a glass substrate at 553 K in a vacuum at different oxygen partial pressures	P = 5×10^{-7} mbar	2.04	186
			PO_2 = 5×10^{-5} mbar	2.20	
			PO_2 = 2×10^{-4} mbar	2.30	
Film	EBE	The films were deposited on different substrate types	Glass	2.36	105
			ITO	2.10	
			FTO	2.05	
Film	Sol–gel	The films were deposited on ITO by different precursors	Metalorganic	1.70	168
			Organic	2.2	
			Inorganic	2.5	
Film	Sol–gel	The films were deposited on ITO with different molar percentages of ICS-PPG	0%	2.44	347
			1%	2.48	
			5%	2.52	
NRs and NSPs	Hydrothermal	The films were hydrothermally deposited at 230 °C for different deposition times (t_d) and were annealed at 500 °C (t_a)	t_d = 4 h and t_a = 1 h	2.45	188
			t_d = 4 h and t_a = 2 h	2.46	
			t_d = 8 h and t_a = 1 h	2.34	
			t_d = 8 h and t_a = 2 h	2.35	
NPs	NPs were prepared by the sol–gel method	Different element doped V_2O_5 NPs	Pure V_2O_5	2.18	172
			Gd doped V_2O_5	2.12	
			Nd-doped V_2O_5	2.10	
Thin film	The films were deposited on an ITO substrate by the PLD method	Different element doped V_2O_5 to form $M_xV_2O_5$	Pure V_2O_5	2.32	173
			Ag-doped V_2O_5 ($Ag_{0.24}V_2O_5$)	2.15	
			Nb-doped V_2O_5 ($Nb_{0.3}V_2O_5$)	2.16	
			Ce-doped V_2O_5 ($Ce_{0.25}V_2O_5$)	2.44	
			Nd-doped V_2O_5 ($Nd_{0.2}V_2O_5$)	2.50	
			Sm-doped V_2O_5 ($Sm_{0.26}V_2O_5$)	2.52	
			Dy-doped V_2O_5 ($Dy_{0.25}V_2O_5$)	2.51	

Table 3 (continued)

Typical morphologies	Synthesis method	Investigated parameter	Note	E_{opt} (eV)	Ref.
Film	The films were deposited on a glass substrate by RF-sputtering	Different Mg doping concentrations in V_2O_5	Mg = 0.0%	2.18	108
			Mg = 6.7%	2.25	
			Mg = 12.5%	2.45	
			Mg = 15%	2.35	
Film	Composite materials were prepared by the MQ method	Different Li doping concentrations in V_2O_5 to form $V_{2-x}Li_xO_{2-\delta}$	$V_{1.85}Li_{0.15}O_{2-\delta}$	2.22	135
			$V_{1.8}Li_{0.2}O_{2-\delta}$	2.16	
			$V_{1.75}Li_{0.25}O_{2-\delta}$	2.14	
			$V_{1.70}Li_{0.30}O_{2-\delta}$	2.08	
Film	The films were deposited on an FTO substrate by RF-sputtering	Different W doping concentrations in V_2O_5 (V:W)	V:W = 1:0	2.43	196
			V:W = 28:1	2.37	
			V:W = 14:1	2.29	
			V:W = 9:1	2.16	
			V:W = 7:1	2.55	
			V:W = 3.5:1	2.62	
			V:W = 2:1	2.76	
NRs	NRs were prepared by the WCR method	Different Gd doping concentrations in V_2O_5	Gd = 0%	2.187	195
			Gd = 1%	2.181	
			Gd = 3%	2.145	
			Gd = 5%	2.098	
			Gd = 10%	2.044	
NPs	NPs were deposited by the sol–gel spin-coating method	Different Sn doping concentrations in V_2O_5	Sn = 0%	3.27	171
			Sn = 2%	3.19	
			Sn = 4%	3.11	
			Sn = 6%	3.07	
L-shape and NWs	L-shaped and NWs were synthesized by the hydrothermal method	Different F doping concentrations in V_2O_5	F = 0%	1.91	198
			F = 1.42%	1.87	
			F = 1.69%	2.04	
			F = 1.74%	1.94	
3D micro–nano spheres	Micro/nanospheres were prepared by the solvothermal method	Different volumes of $SnCl_4$ solution (X ml $SnCl_4$ of 0.1 M) added in the V_2O_5 precursor and the difference between before and after annealing (S_{xa}) at 550 °C for 1 h	S_0: X = 0 ml	2.30	197
			S_0: X = 0 ml	2.31	
			S_1: X = 1 ml	2.21	
			S_{1a}: X = 1 ml	2.28	
			S_2: X = 2 ml	2.11	
			S_{2a}: X = 2 ml	2.25	
			S_3: X = 3 ml	1.89	
			S_{3a}: X = 3 ml	2.22	
NRs	Nanocomposite films were prepared by the sol–gel spin-coating method	V_2O_5/GO nanocomposite with different volume percentages of GO	0% GO	2.670	205
			1% GO	2.632	
			2% GO	2.619	
			3% GO	2.608	
Film	The films were deposited by the drop-casting method	Different volumes of isopropyl alcohol (IPA) were mixed with vanadium oxytriisopropoxide and chosen additive (IPA:alkoxide:additive) 1000:10:1 (LCP), 250:10:1 (HCP), and the effect of polyethylene glycol – PEG	LCP	2.47	206
			LCP heat treated	2.18	
			LCP–PEG	2.44	
			LCP–PEG heat treated	2.11	
			HCP	2.62	
			HCP heat treated	2.69	
			HCP–PEG	2.59	
			HCP–PEG heat treated	2.49	
Gel	WCR	V_2O_5/IPA (1:1) composites were kept for different times	Fresh	2.70	37
			24 h-old	2.80	

500 °C,[190] respectively. E_{opt} increases from 2.5 eV to 2.2 eV as a function of treatment temperature in the hydrothermal process.[191] On the other hand, the films fabricated by spray coating revealed an increase in E_{opt} from 1.99 to 2.05 eV with increasing substrate temperature from 300 to 400 °C.[128]

In another work, the color process transformed from greenish-yellow to yellow as a function of temperature and annealing time.[83] The transformation from the as-deposited to β-V_2O_5 due to heat treatment also impacts the absorption and film color. The α-V_2O_5 strongly absorbs light at wavelengths of approximately 410 nm and shows a slight blue shift as a function of the annealing temperature. In contrast, mixing α- and β-V_2O_5 leads to a substantial shift of the tailing absorption to lower energy.[67] Consequently, the film color changes from dark yellow to transparent yellow. Similarly, the films prepared by AA-CVD appeared brown (as-deposited) and yellow (post-annealing).[192]

4.2 Influence of dopants

Suitable doping elements may alter the band structure and modify E_{opt}. The color of the produced V_2O_5 changes following dopant element and amount. Fig. 8A reveals that the color of V_2O_5 micro-powder changes from yellow (undoped) to dark green/yellow (2% Na-doped), orange (3% Ba-doped), and bright yellow (3% Al-doped).[193] The film color changed to pale yellow according to the fluorine dopant amount (Fig. 8B).[194] Doping

with metal, non-metal, and rare-earth-doped V_2O_5, such as Gd, Nd, Ag, Nb, Ce, Sm, Dy, Mg, Li, W, Sn, Yb, La, and F, affects the E_{opt} of V_2O_5 with no clear tendency.[108,135,171–173,195–200]

The E_{opt} increased with increasing Ce-, Sm-, Dy-, and Mg-doped V_2O_5, whereas Sn-, Nb-, Gd-, Ag-, and Li-doped V_2O_5, lead to a decrease in E_{opt}. For Nd, F, La, Yb, and W doping, E_{opt} changes depending on the dopant concentration. The E_{opt} decreased when the V : W ratio was lower than 9 : 1, but this trend was reversed, and E_{opt} increased when V : W was higher than 7 : 1. Depending on the environments, such as the solvent, temperature, time reaction, and pressure, dopants bond with different functional groups in the vanadium precursors, which affects the V_2O_5 properties. The different radii of elements with reaction dynamics lead to the competition and replacement or location between the layers of the doping element inside V_2O_5 at different positions, leading to a change in the local and band structures.[135] Dopants can urge or inhibit crystallization processing. The lattice constant and crystalline size decrease with decreasing dopant radius compared to the radius of the host lattice while they increase with increasing dopant radius. These elements form V–M oxide or local vanadate (MVO_4). The experimental results show that the unit cell volume of M-doped V_2O_5 (M = Na, Ba, and Al) changes according to pure V_2O_5, being largest with 3% Ba and smallest with 2% Na.[193]

Moreover, dopants can act as donors in V_2O_5 to form new energy levels below the CB. The new transition between the VB and new energy levels occurs easily, which leads to a decrease in E_{opt}.[135,196] On the other hand, a higher excess donor concentration fills the new energy level and shifts the E_f to a higher energy state.[173,196] The insertion of an ionic element also generates defects and oxygen vacancies to produce lower oxidation states, such as V^{4+} and V^{3+}. The fraction of V^{4+}/V^{5+} or ($V^{4+} + V^{3+})/V^{5+}$ increases with increasing dopant concentration, which provides more electron carriers. Electrons were also generated due to the replacement of V^{5+} by M^{x+} ($x > 5$). For example, the replacement of V^{5+} by Cr^{6+} or W^{6+} provides excess electrons. These electrons can enter the split-off band, which widens the E_{opt} and causes a color change. The color films change from bright yellow to mustard yellow and olive green, corresponding to the Cr doping concentrated increase of 0.21%, 2.41%, and 4.34%, respectively (Fig. 8C).[120] The optical bandgap is $E_g = E_{opt} + \Delta E_g^{BM}$, where E_{opt} is the optical bandgap of pure V_2O_5, and ΔE_g^{BM} is the Burstein–Moss shift, as described in eqn (4).[201]

$$\Delta E_g^{BM} = \frac{h^2}{8\pi^2 m_{vc}^*}(3\pi^2 n_e)^{2/3} \qquad (4)$$

where, $(m_{vc}^*)^{-1} = (m_c^*)^{-1} + (m_v^*)^{-1}$ is the effective mass.

4.3 Influence of composites

The color change observed for composite materials, based on at least two constituents, is associated with a modulation of E_{opt} because of the change in physical and chemical properties of the original materials.[202] Fig. 9A reveals the different colors corresponding to the different electropolymerization times of V_2O_5/PANI composites.[203] Pure V_2O_5 NFBs exhibit yellow color,

and after increasing the electropolymerization deposition time, V_2O_5/PANI color changes to yellow-green (30 s), green (60 s), deeper green (180 s), and dark green (240 s). The color of gel produced changes after eight weeks by mixing V_2O_5 and GO with the assistance of an acid, while the color of pure V_2O_5 remains in D.I water after six months (Fig. 9B).[204] The presence of GO as an oxidizing agent accelerates the oxidation process, causing the morphology to change and the V^{4+} state to rise. Moreover, V^{5+} is reduced to V^{4+} due to a partially reversible reaction of H_2O molecules of V_2O_5 hydrate and alcohol in organic molecules, which changed the color from red to green (gel).[37]

The E_{opt} of the GO/V_2O_5 composites decreased from 2.67 to 2.608 eV because of the effects of the narrowing gap ($E_g \sim 0.5$ eV) of GO with increasing GO concentration from 0 to 3 vol %.[205] The E_{opt} was also affected by the polymer types (isopropyl alcohol – PIA, alkoxide, and polyethylene glycol – PEG) and different dilutions (low concentration dilution – LCP and high concentration dilution – HCP).[206] The HCP film showed a higher E_{opt} than the LCP film, but E_{opt} decreased to 0.51 eV and 0.38 eV in the PEG-containing LCP and HCP thin films, respectively.

In particular, the E_{opt} and optical transmission of all films decreased after heat treatment, which led to different colors of the pristine film. Hence, the composite materials affect the color of the pristine film because of the absorption shift and the alteration in intensity variation of the optical transmittance. Another example is the presence of carbon on the surface of V_2O_5 NBs, which decreased the ΔT and produced a blue shift in the as-prepared film and after annealing at 250 °C. In contrast, ΔT increased dramatically after annealing at 300, 350, and 400 °C and reached the highest transmittance of 80% (at 790 nm) after annealing at 350 °C.[207]

5. Chromic phenomena of V_2O_5

5.1 Chromogenic properties of V_2O_5

In contrast to "fix" chromism, "responsive" chromogenics including electrochemical-, gas-, photon-, and thermal-reduction processing, can control the V_2O_5 film color via direct control of the band structures through external stimuli, such as applied voltage (electric current), gas concentration, excitation light source, and temperature. These external impacts lead to a reversible/irreversible physical and chemical reaction that alters both the electronic and atomic structures of the material. Fig. 10 shows the four types of CDs using V_2O_5, namely electrochromic, ECD; gasochromic, GCD; photochromic, PCD; and thermochromic, TCD.

Owing to the special band structure, the color change is caused by a shift in the absorption and intensity of the transmitted/reflected light. Fig. 11 shows the transmission spectra of the chromogenic V_2O_5 devices (except TCDs). The changes in E_{opt} and transmittance/reflectance are the most important parameters for evaluating the possible chromic phenomena of V_2O_5 (where λ_b/λ_c and T_b/T_c are the tail of the
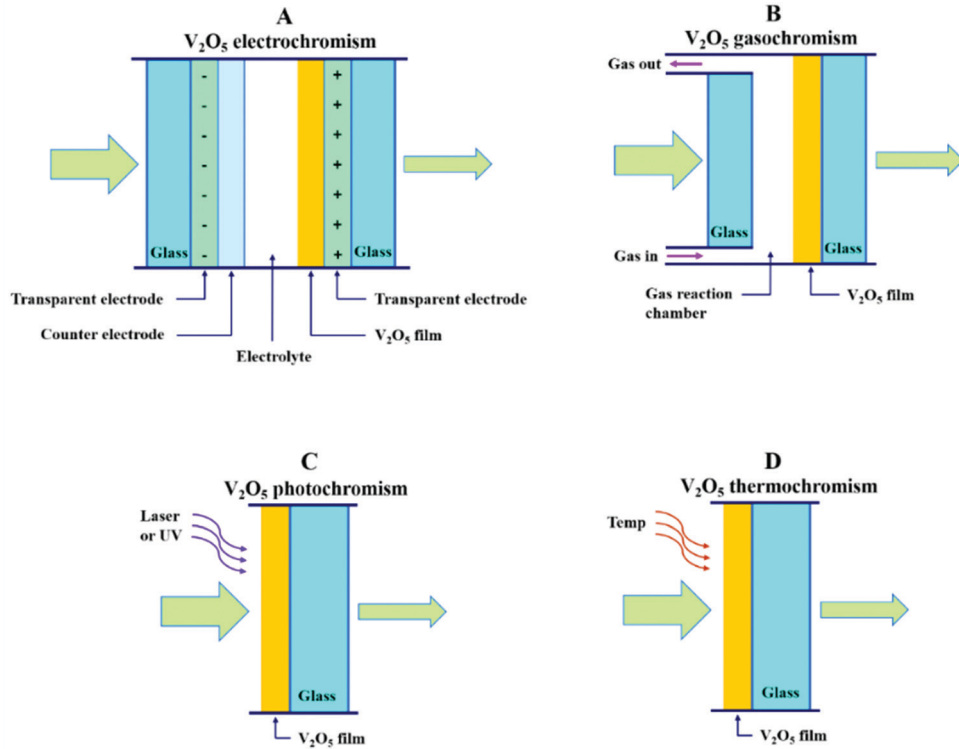
Fig. 10 Illustration of the four typical V_2O_5 CDs: (A) ECD, (B) GCD, (C) PCD, and (D) TCD.
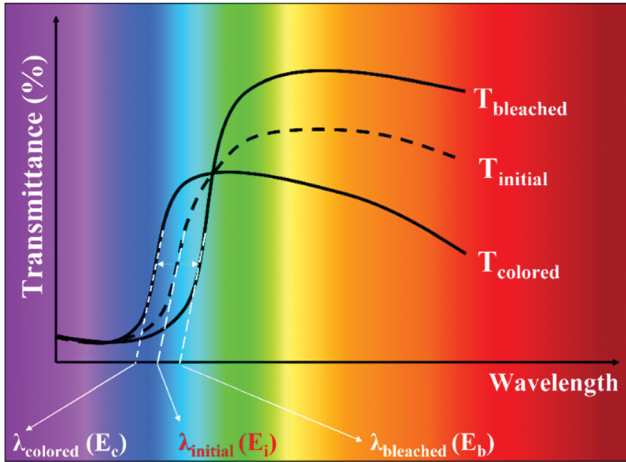

Fig. 11 Simulation of the transmission spectra of V_2O_5 film at three states: initial state, bleached state, and colored state.

absorption/transmittance and percentage transmittance (%) in the bleached/colored states, respectively). Furthermore, parameters, such as the switching time, optical density, coloration efficiency, cycling stability, durability, and operational environment, are the figures of merit to evaluate CDs. Depending on the utilization, the efficiency of the CDs can be evaluated using different parameters.

The change in optical bandgap (ΔE_{opt}) is the altered electron band structure of a material that leads to an absorption shift ($\Delta \lambda$) due to the relationship between the energy of absorption

and excitation $\Delta E = \dfrac{hc}{\lambda}$ (where h is Planck's constant and c is the speed of light in vacuum), as defined by eqn (5) and (6).

$$\Delta E_{opt} = E_c - E_b \text{ or } \Delta E = E_{c/b} - E_i \qquad (5)$$

$$\Delta \lambda = \lambda_c - \lambda_b \text{ or } \Delta \lambda = \lambda_{c/b} - \lambda_i \qquad (6)$$

The optical transmittance/reflectance variation ($\Delta T/\Delta R$) is the offset intensity of light transmittance $T(\lambda)$ or light reflectance $R(\lambda)$ between the color state and bleach state or between the color (bleach) state and initial state. This is an essential parameter for evaluating the intensity of the color change in a chromogenic device and can be estimated at a specific wavelength or in white light.[15] Although $T(\lambda)$, $R(\lambda)$, and the intensity of absorption $A(\lambda)$ have the relation, $T(\lambda) + R(\lambda) + A(\lambda) = 1$, the optical contrast was calculated using eqn (7) or (9). Moreover, the optical contrast can also be evaluated from the ratio of $T(\lambda)$ or $R(\lambda)$ between states, as shown in eqn (8) or (10).[15]

$$\Delta T \ (\%) = T_b(\lambda) - T_c(\lambda) \text{ or } \Delta T \ (\%) = T_{b/c}(\lambda) - T_i(\lambda)$$
$$\qquad (7)$$

$$\Delta R \ (\%) = R_c(\lambda) - R_b(\lambda) \text{ or } \Delta R \ (\%) = R_{c/b}(\lambda) - R_i(\lambda)$$
$$\qquad (8)$$

$$CR = T_b/T_c \text{ or } CR = T_i/T_{c/b} \qquad (9)$$

$$CR = R_b/R_c \text{ or } CR = R_i/R_{c/b} \qquad (10)$$

$\Delta \lambda$ and ΔT occur simultaneously in V_2O_5 chromic materials. Consequently, V_2O_5 shows the anodic coloration toward short wavelengths and cathodic coloration at longer wavelengths. In

particular, in V_2O_5, $\Delta\lambda$ can be changed while ΔT is maintained or slightly changed. This leads to a color change while the brightness changes only slightly.

The switching response time (t_c and t_b) is defined as the time for color conversion of transmittance (reflectance) percentage,[93] with specific standards for this parameter.[208] The switching response time for chromogenic materials was evaluated as a color conversion reaching 90–95%, but some studies were based on a range of 70 to 85%.[60,208]

The optical density (OD) is the change in the absorbance of a thin film, which is defined in eqn (11). OD expresses the change in the optical absorption coefficient (or transmission) at a given wavelength before and after the colored states (or bleached state and colored state).[15,18]

$$\Delta OD(\lambda) = \log \frac{T_b(\lambda)}{T_c(\lambda)} \quad (11)$$

where T is the transmittance.

The coloration efficiency (CE) is one of the most important metrics for evaluating EC materials and is defined as the change in OD acquired by the injected charge per unit area, as expressed in eqn (12).[142,209]
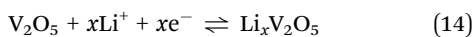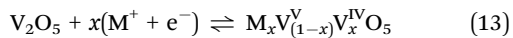
$$CE(\eta) = \frac{\Delta OD}{Q} = \frac{\log\left[\frac{T_b(\lambda)}{T_c(\lambda)}\right]}{Q}, \quad (12)$$

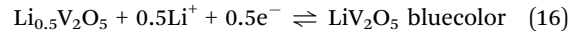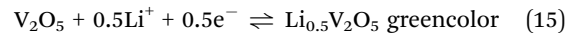where Q is the electronic charge injected into the EC material per unit area.

5.1.1 Cycling stability. The thermal stability and long-term lifetime are standards to evaluate and determine the cycling stability of CDs. CDs usually undergo fatigue or failures inside solid materials during cycling caused by physical changes or chemical reactions.[15] This leads to a loss of optical contrast and a decrease in performance. The standard to evaluate differs according to the CD types and applications. For example, stable EC materials are expected to exhibit a life cycle of more than 10^4 cycles. ECDs require at least 15 000 cycles to maintain stability over 20 years in building windows and 10^6 cycles in eyewear and rear-view mirrors.[192] Sections 5.2 to 5.5 provide details on the values and mechanism of all parameters.

5.2. Electrochromic process in V_2O_5

5.2.1 Fundamentals of electrochromic V_2O_5. The form of the layers in the α-V_2O_5 structures provides inserted spaces for intercalated metal ions (M^{n+}), such as Li, Na, K, Ca, Mg, Al, and Zn metals. Since 1970, V_2O_5 has been a positive electrode candidate for metal ion intercalation.[210,211] Among various ions, lithium has been used extensively in ion batteries and electrochromism. The electrochemical reaction for M^{n+} and Li^+ ion injection/extraction in V_2O_5 is expressed in eqn (13) and (14).[210,211]

$$V_2O_5 + x(M^+ + e^-) \rightleftharpoons M_x V_{(1-x)}^V V_x^{IV} O_5 \quad (13)$$

$$V_2O_5 + xLi^+ + xe^- \rightleftharpoons Li_x V_2 O_5 \quad (14)$$

The lithium concentration x in $Li_x V_2 O_5$ is given by $x = \frac{N_{Li}}{N_{V_2O_5}}$, where $N_{V_2O_5} = \frac{\rho \cdot A \cdot d \cdot N_A}{M}$ is the number of V_2O_5 molecules in the sample (where the volume of the layer is Ad; ρ, N_A, and M are the density of materials, Avogadro's constant, and the molar weight, respectively) and $N_{Li} = \frac{Q}{e}$ is the number of inserted lithium-ions with $Q = \frac{I}{t}$ (where I is a sufficiently low applied current, and t is the time necessary to apply a current to obtain the lithium concentration).[212] The lithium concentration x in $Li_x V_2 O_5$ is characteristic of the film color. For example, when $x = 0.5$ and 1, green and blue colors are observed, as shown in eqn (15) and (16), respectively.[90] On the other hand, the specific relationship between the x value and color of ECDs depends on the intrinsic film.

$$V_2O_5 + 0.5Li^+ + 0.5e^- \rightleftharpoons Li_{0.5}V_2O_5 \text{ greencolor} \quad (15)$$

$$Li_{0.5}V_2O_5 + 0.5Li^+ + 0.5e^- \rightleftharpoons LiV_2O_5 \text{ bluecolor} \quad (16)$$

The layers are held together *via* weak vdW forces. The ion injection/extraction can alter the V_2O_5 film color because of the alteration of the crystal structure and band structures leading to a phase transformation. In crystallized phases, the change in lattice parameters caused by Li^+ ion intercalation leads to phase transformations for α-, ε-, δ-, γ-, and ζ-$Li_x V_2 O_5$, as shown in Fig. 12A.

De Jesus *et al.*[29] and Cocciantelli *et al.*[73] discussed the diffusion pathways in the intercalated materials and phase transition in V_2O_5. The α-, ε-, and δ-$Li_x V_2 O_5$ showed a quite reversible transformation, while γ- and ζ-$Li_x V_2 O_5$ remained after the charge–discharge cycle. In the first discharge, phase transition occurs as line D_0 (Fig. 12A). For a low lithium concentration ($x \leq 0.1$), the interlayer spacing of V_2O_5 expanded slightly, and the α-V_2O_5 phase was retained. For $0.1 \leq x \leq 0.35$, the α-phase coexists with another orthorhombic ε-phase, stabilizing the ε-V_2O_5 with increasing concentration, $0.35 \leq x \leq 0.8$. With the further insertion of lithium ions ($0.88 \leq x \leq 1$), ε-V_2O_5 transforms to δ-V_2O_5. The γ-phase coexists with the δ-phase ($1 \leq x \leq 1.4$), and the ζ-phase coexists with the δ-phase ($1.4 \leq x \leq 2.0$).[29,73] For the first recharge (line C_1, Fig. 12A), a mixture of $\delta + \gamma$ phases at $x \geq 0.9$, $\varepsilon + \gamma$ at $x \approx 0.7$, $\alpha + \gamma$ at $x \approx 0.5$, and $\alpha + \gamma'$ occurs as x tends to zero. At the beginning of the second discharge (line D_1, Fig. 12A), lithium ion intercalations occur first in the γ'-phase. The formation of the δ-phase occurs for a higher lithium concentration than the first discharge. In contrast, the co-existence of the γ-phase with the δ-phase and ζ-phase occurs at lower lithium concentrations.

In chromic applications, optical reversibility is the most important property. Therefore, a lithium concentration in the range $0 \leq x \leq 1$ is the most appropriate to investigate the chromic phenomena in V_2O_5 materials. The high crystallinity of V_2O_5 could exhibit better reversibility than low crystallinity or amorphous films.[16]
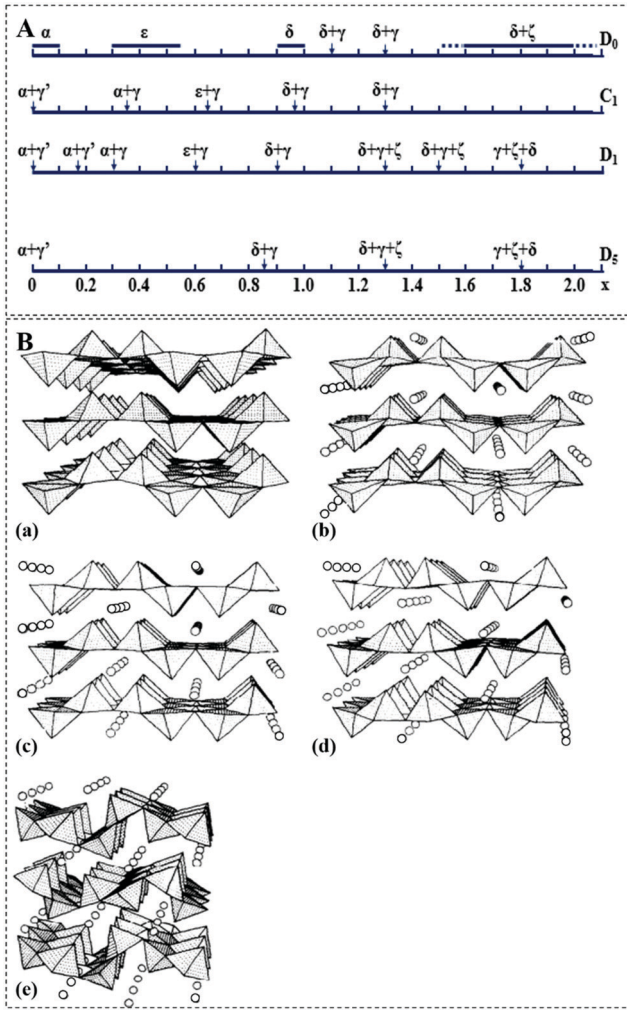
Fig. 12 Phase transition and the arrangement of VO_n polyhedral: (A) result of XRD analysis: (D_0) first discharge, (C_1) first charge, (D_1) second discharge, and (D_5) fourth charge. (B) Structural phase transition in V_2O_5: (a) layered orthorhombic α-V_2O_5 structure, (b) α-$Li_xV_2O_5$, (c) ε-$Li_xV_2O_5$, (d) δ-$Li_xV_2O_5$, and (e) γ-$Li_xV_2O_5$, reproduced with permission (Copyright 2022, Elsevier[73]).

As the lithium insertion content is approximately $0 < x < 1$, V_2O_5 skeletons do not change, and the apical V=O bonds follow one direction along the b-axis. The α-V_2O_5 phase transforms to α-, ε-, and δ-$Li_xV_2O_5$ because of the puckering of layers and the expanding interlayer space (Fig. 12B(a)–(d)). This leads to the entire reversibility of the $\alpha \leftrightarrow \varepsilon \leftrightarrow \delta$ phase transitions as a re-charge.[213] Further increases in the lithium content to $1 < x < 2$ result in the rotations of two edge share (VO_5) square pyramidal units by 90 °C (Fig. 12B(e)), leading to an irreversible transformation of γ- and ζ-$Li_xV_2O_5$.[73] This distortion allows higher lithium concentrations with a complicated oxidation process.[29]

During electrochemical reduction, electrons are injected to reduce pentavalent vanadium (V^{5+}) to lower valence states, such as (V^{4+}) and (V^{3+}). The V^{4+}/V^{5+} or V^{3+}/V^{5+} ratio depends on the cathodically and anodically polarized values. Table 4 lists the amount (%) of V^{5+}, V^{4+}, and V^{3+} with different states (pristine, colored state, and bleached state) of the film *via* XPS fitting

Table 4 Atomic percentage of V in different valence states (V^{5+}, V^{4+}, and V^{3+}) in the as-deposited film and reduced/oxidized film

Sample	Atomic percentage of V in different valence states			Ref.
	V^{5+} (%)	V^{4+} (%)	V^{3+} (%)	
As-deposited V_2O_5	100	0.0	—	184
Annealed for 30 min	71	29	—	
Annealed for 24 h	89	11	—	
+0.2 V	91	09	—	
−2.0 V	13	87	—	
Pristine V_2O_5	75.91	18.02	6.08	348
+2.0 V	81.15	10.78	8.07	
−0.3 V	9.06	80.02	10.92	
−1.5 V	7.99	80.12	11.90	
−2.0 V	6.65	81.73	11.62	
As-prepared SnO_2/V_2O_5	76.2	23.8	—	262
+1 V	76.0	24	—	
+0.4 V	52.2	44.8	—	
−1 V	43.7	56.3	—	
As-deposited V_2O_5	91	9	—	216
+1.9 V	93	7	—	
−0.3 V	68	32	—	
−0.9 V	27	73	—	
As-deposited V_2O_5	57.45	42.55	—	349
+2 V	75.35	24.65	—	
−2 V	35.78	64.22	—	
As-deposited V_2O_5	83.89	4.46	11.65	244
+2 V	90.40	4.92	4.68	
+1.5 V	83.28	11.71	5.01	
+1.0 V	73.28	25.11	1.61	
−0.2 V	29.39	65.30	5.31	
−0.5 V	4.29	83.25	12.46	

calculations. The color of pure vanadium oxide is yellow-orange (V^{5+}), blue (V^{4+}), green (V^{3+} or mixture V^{4+} and V^{5+}), and violet (V^{2+}).[31,214] Other vanadium oxides, such as V_2O_3, and the family of Wadsley phases (V_nO_{2n+1}), such as V_3O_7, also exhibit multi-valences during the EC process.[215–217]

Owing to the presence of V^{3+} ions, the color of the film changes to olive green, and the multiple colors in V_2O_5 are attributed to the presence of V^{3+}/V^{4+} and V^{5+}.[83,216] A potential range where the vanadium ions with the two oxidation states coexist at a well-defined ratio can explain the green intermediate coloring by the occurrence of the V^{5+}/V^{4+} redox couple.[57,82,214,216,218] The mechanism of the multi-electrochromism observed in vanadium oxides is explained by a change in the oxidation state and a structural modification. Indeed, the CV curve, Fig. 13A, shows a phase transition to α/ε, ε/δ, and δ/γ during the reduction process that corresponds to three cathodic peaks at 0.38 (C1), 0.19 (C2), and −0.70 V (C3), respectively. Accordingly, ε/α, δ/ε, and γ/δ phase transitions occur at the three anodic peaks, denoted as A1, A2, and A3, respectively.[57]

These findings are consistent with the color of V^{3+}, V^{4+}, and V^{5+} in the ionic liquid [EMIM][VO_3] during the electrolysis process (Fig. 13B). The yellow color of the initial V^{5+} changes to blue (V^{4+}), green (mixed V^{4+}/V^{5+}), and dark green (V^{3+}) upon electrolysis. The origin of the color change observed for vanadium oxide was also explained by a structural change between the amorphous and crystallized states (Fig. 13C).[216] During cycling, the reduction process leads to a mixture of V^{4+} and
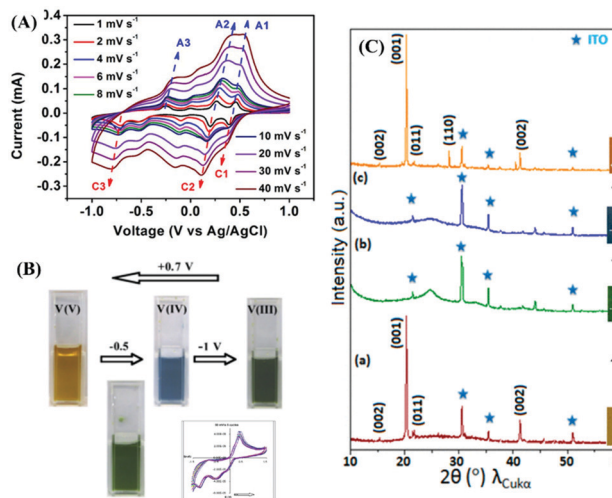
Fig. 13 Change in the oxidation state, color, and structural modification: (A) CV curves of V_2O_5 at various scan rates, (B) color change corresponding to the three oxidation states of ionic liquid [EMIM][VO_3], and (C) *ex situ* grazing incidence XRD of the V_2O_5 film before cycling (a) and after 50 cycles at the oxidized state (b), reduced green state (c), and reduced blue state (d). The figures are reproduced with permission (Copyright 2022, Nature,[57] Royal Society of Chemistry,[219] and American Chemical Society[216]).

V^{5+} and passes from the crystalline to the amorphous state. The bleaching process (oxidized state) leads to a fully oxidized V^{5+} state, which is in agreement with the orange color. The complete reoxidation at the end of each cycle allows the recrystallization of pristine V_2O_5.

Moreover, Li^+ intercalation alters the crystalline order, leading to a phase transformation, reacts with oxygen in the lattice to form lithium oxides (LiO and Li_2O), and generates V_o defects.[178] Consequently, the proportion of the V^{4+} oxidation state increases, and a mid-gap state between the VB and split-off CB was formed (Fig. 14a and b).

The appearance of a new transition between the VB and mid-gap states (Fig. 14b) leads to an increase in the absorption in the NIR region. The excess electrons move the entire crystal and begin to fill the unoccupied mid-gap states and split-off states (Fig. 14c). Consequently, the optical transitions of absorption (or transmittance) have four kinds of transitions: (1) VB ↔ main CB in the range of 300–450 nm, (2) VB ↔ split-off CB in the range of 450–600 nm, (3) VB ↔ mid-gap states in the range of 650–850 nm, and (4) mid-gap states ↔ main CB in the range >1000 nm. These transitions are noted as I-1, I-2, I-3, and I-4, respectively, as shown in Fig. 14c. These may lead to the simultaneous color collectives of V_2O_5 thin films.

For the colored state, in the film-upon reduction, the electron concentration increases, leading to an increase in the Fermi level (E_f) to split-off CB. Consequently, the conductivity increases, the optical bandgap changes, and a color center is formed. When the electron concentration is high enough, E_f enters between the main CB and the split-off CB (Fig. 14c).[29,50,158,178,220] The transition from the split-off CB to the main CB is forbidden. In contrast, the transition from the VB to the split-off CB appears weakly because of the filled electrons in the split-off CB. Therefore, the absorption intensity I-1 decreases slightly while the absorption intensity I-2 decreases strongly. The absorption spectra begin to shift to a shorter wavelength (Fig. 14b and 14c). The absorption due to a transition between the mid-gap state and main CB and the shift to a shorter wavelength co-occur, leading to an increased absorption intensity of I-3 and I-4.

A phase transition occurs when the lithium concentration is increased, which causes a change in the density of states of V_2O_5. When Li-ions lie between O(1) and V ions or between two O(2) ions, the V═O(1) bonding lengths become shorter or longer compared to the initial lattice of V_2O_5. Electrons from the Li_2s orbitals transfer to the V3d states due to the higher E_f. The split-off CB becomes narrower (bandwidth increases) or even disappears (split-off CB merges with CB), leading to an increase in the bandgap (Fig. 14d).[29,50,158,178,220] Consequently, the absorption transition from the VB to the split-off CB (noted I-2) disappears or shifts to a higher energy. Supposedly, these I-1, I-2, I-3, and I-4 transitions co-occur. In this case, the transmittance of the colored state shifts to a shorter wavelength, and the intensity decreases in the IR and NIR regions, as shown for the colored state in Fig. 11.

Lithium ions and excess electrons are withdrawn reversibly from V_2O_5 in the bleached/oxidized state. The recrystallization
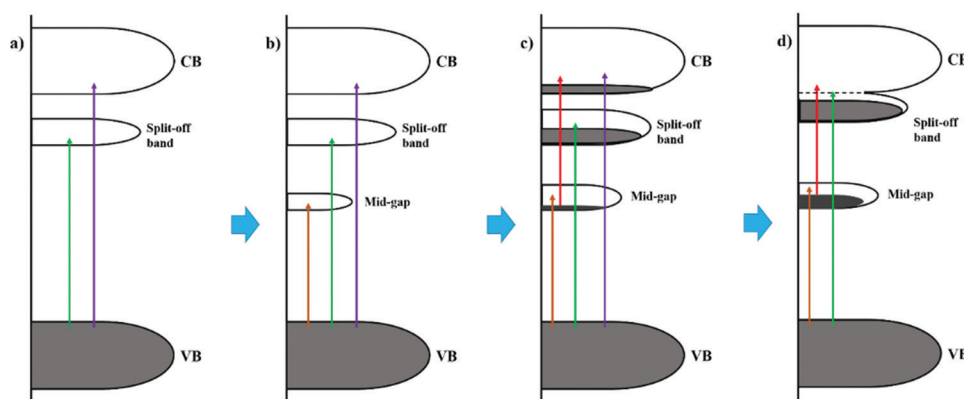
Fig. 14 Schematic diagram of the energy band structure and optical transition ability in V_2O_5: (a) pure V_2O_5, (b) and (c) V_2O_{5-y}, and (d) $Li_xV_2O_5$.
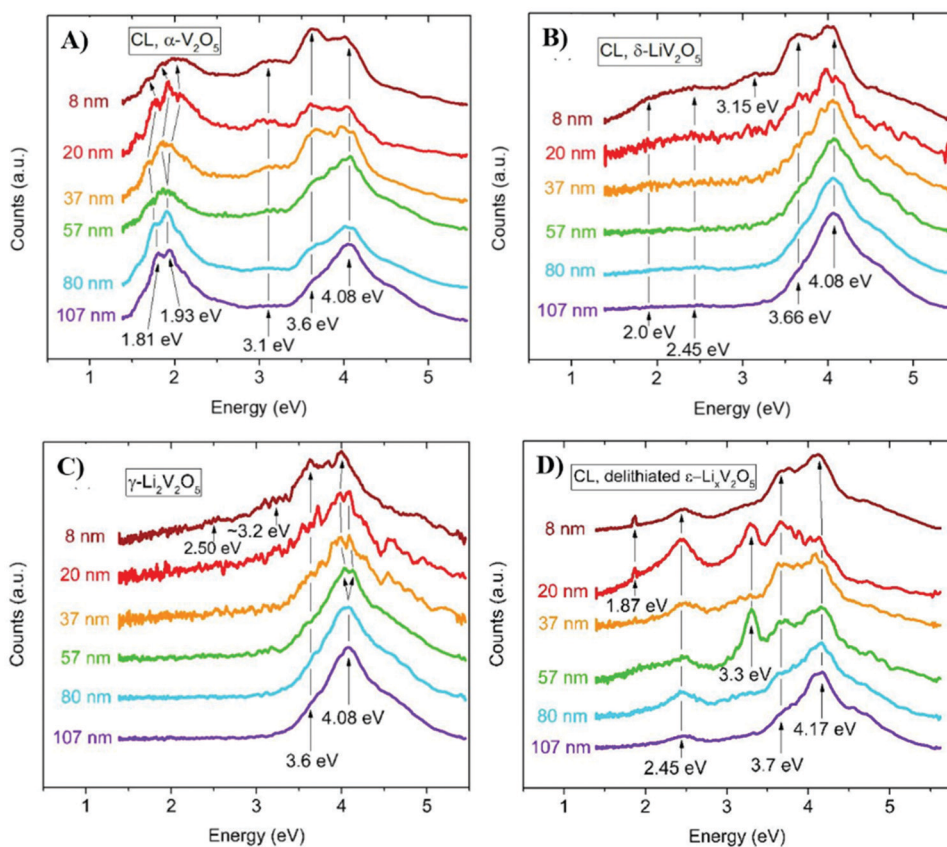
Fig. 15 CL spectra of lithiated/delithiated $Li_xV_2O_5$: (A) α-V_2O_5, (B) lithiated δ-LiV_2O_5, (C) lithiated γ-$Li_2V_2O_5$, and (D) de-lithiated ε-$Li_xV_2O_5$ ($0.1 < x < 0.3$), reproduced with permission (Copyright 2022, Royal Society of Chemistry[221]).

process, reformation of the split-off state, and some of the defects are recovered. The amount of V^{4+} after bleaching (oxidized state) can become less than or equal to that of the as-deposited film (pristine V_2O_5) (Table 4). Absorption occurs primarily due to a transition from the VB to the split-off CB and from the VB to the main CB, while the transitions from the VB to the mid-gap state and from the mid-gap state to the main CB are very weak. Consequently, the absorption intensities of I-1 and I-2 are strong, while the absorption intensities of I-3 and I-4 are very weak.

Fig. 15 shows the recombined transition (depth-resolved cathodoluminescence (DRCL) spectroscopy) spectra of $Li_xV_2O_5$.[221] The DRCL spectra of α-V_2O_5 with an electron beam energy ($E_B = 0.5$ kV) showed peaks at 1.8–2, 3.2, 3.6–3.7, and 4.0 eV, with a wide feature of approximately 2 eV and 3.6 eV as E_B increased (Fig. 15A). With δ-LiV_2O_5, the features around 1.8–2.0 eV were suppressed, and a new peak at 2.45 eV was observed for $E_B = 0.5$ kV. As E_B increases, these peaks < 3 eV are suppressed, and a peak around 4.0 eV was observed (Fig. 15B). With γ-$Li_2V_2O_5$, the weak peak at 2.45 eV remains, but the peaks below 3.0 eV are suppressed. Except for the 4.0 eV feature, all emission spectrum vanished as E_B was increased (Fig. 15C). With the de-lithiated ε-$Li_xV_2O_5$ ($0.1 < x < 0.3$), the narrow peak at 1.8 eV and broad peak at 2.45 eV were observed at a low E_B. As E_B increased, the peak at 3.3 eV appeared ($E_B = 1.0$ kV and 2.0 kV) while the narrow peak at 1.87 eV was suppressed (Fig. 15D).

Jarry *et al.*[222] observed the relationship between the color change and the local structure of vanadium oxide during the electrochemical process. The color of the film changes with the associated phase transformation (Fig. 16A), orange ↔ yellow gold ↔ light green ↔ darker green corresponding to (3.4 V: α-V_2O_5) ↔ (3.2 V: ε-$Li_xV_2O_5$) ↔ (2.8 V: δ-$Li_xV_2O_5$) ↔ (2.2 V: γ-$Li_xV_2O_5$), respectively. On the other hand, colored/reduction–bleached/oxidation states are not perfectly symmetrical. The color of the fully oxidized material (3.4 V: α-V_2O_5) does not return to the pristine α-V_2O_5 film color (orange) because of an irreversible phase transformation of γ-V_2O_5 as $x > 1$.

Fig. 16B presents the Raman spectra of pristine α-V_2O_5 with cycled $Li_xV_2O_5$ samples and reference powders (Li_2O, V_2O_4, and V_2O_3). The vibrations between O and V, such as O(a)–V, V–O(a)–V, and O(a)–V–O(b), generate 21 Raman active modes, $7A_g + 3B_{1g} + 7B_{2g} + 4B_{3g}$. The Raman spectra showed 11 peaks, including 102 (Ag), 144 (either B_{1g} or B_{3g}; B_{1g}/B_{3g}), 195 (Ag/B_{2g}), 283 (B_{1g}/B_{3g}), 301 (Ag), 403 (Ag), 483 (Ag), 523 (Ag), 701 (B_{1g}/B_{3g}), 850 (B_{1g}), and 993 (Ag) cm^{-1}.[223] The Raman spectra of pristine pure α-V_2O_5 showed a predominant low-frequency peak at 143 cm^{-1}, corresponding to the bent vibration mode B_{3g}, while the highest frequency ν(d_1) mode at 995 cm^{-1} originates from the V=O_1 double bonds. Other peaks were at 480, 525, and 700 cm^{-1} from the vibration modes A_g (V–O_3–V), ν(d_4), and ν(d_3), respectively. For δ-$Li_xV_2O_5$ (sample VI, V, and VIII, $x \approx 1$),

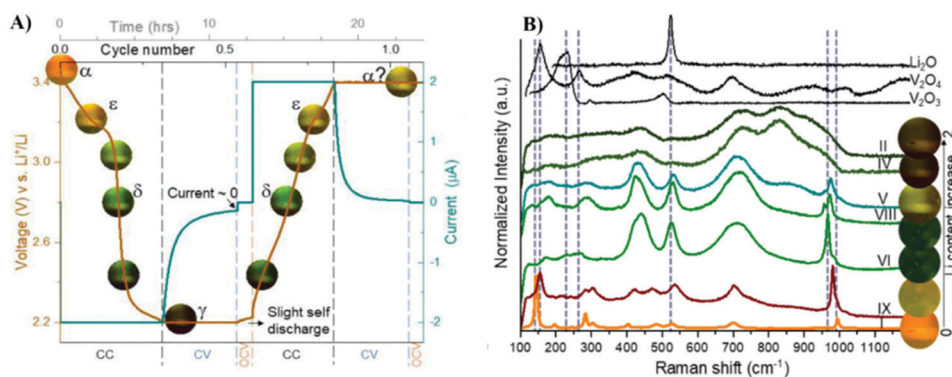**Fig. 16** Electrochemical and Raman spectra of $Li_xV_2O_5$ ($0 < x < 2$): (A) electrochemical and (B) Raman spectra of $Li_xV_2O_5$ as a function of lithium deintercalation/intercalation ($0 < x < 2$), reproduced with permission (Copyright 2022, American Chemical Society[222]).

the peak of mode B_{3g} is extinct while the peak of 995 cm^{-1} was shifted to 967 and 957 cm^{-1}. For γ-$Li_xV_2O_5$ (sample II and IV, $x \approx 2$), these signature peaks disappeared as a shoulder of a peak at 930 cm^{-1}, and two new peaks appeared at 830 and 730 cm^{-1}.

For α-$Li_xV_2O_5$ and Li-poor ε-$Li_xV_2O_5$ (sample IX, $x \approx 0$), these peaks did not recover perfectly, such as the original position and intensity of pristine pure α-V_2O_5. The Raman spectra of the reference powders (LiO_2, V_2O_4, and V_2O_3) showed that the peaks of V_2O_4 (155 and 267 cm^{-1}) and V_2O_3 (223, 300, and 500 cm^{-1}) did not overlap with the peaks of $Li_xV_2O_5$ while the peak at approximately 523 cm^{-1} for Li_2O overlapped with that of α-, ε-, and δ-$Li_xV_2O_5$.

5.2.2 V_2O_5 electrochromic thin films and devices. Colton reported the first study on the photochromism and electrochromism of V_2O_5 films fabricated by vacuum evaporation using X-ray electron and absorption spectroscopy in his PhD thesis and publications in 1976–1977[224–226] after the important studies on the ability of lithium intercalation in V_2O_5 materials by John B. Goodenough, M. Stanley Whittingham,[210] and Akira Yoshino (Nobel prize in chemistry 2019 for the development of lithium-ion batteries). The V_2O_5 film changes color from yellow to greenish-blue with upon lithium intercalation and X-ray irradiation. Dickens et al.[227] examined the relationship between the phase transition and the coloration of $Li_xV_2O_5$ ($0.1 < x < 1.1$) in 1979. The phase transition and coloration occurred with increasing lithium content in $Li_xV_2O_5$: ochre ($x = 0.1$), pale green ($x = 0.24$), dark green ($x = 0.45$–0.69), dark blue ($x = 0.78$), and blue black ($x = 1.08$).

Sato et al. designed the EC light transmission modulators containing an aqueous electrolyte solution between the EC layer electrode (WO_3, MoO_3, and V_2O_5 film) and the SnO_2 transparent electrode substrate.[228] Compared to WO_3 and MoO_3 films, the transmittance spectrum of the V_2O_5 film shifted towards a shorter wavelength with a decrease in intensity, extending to the UV region following the change in lithium intercalation. Rauh et al.[229] and Yoshino et al.[230] reported another sandwich-type modulator using two V_2O_5 films as two EC elements on ITO substrates in 1987. These modulator systems showed that V_2O_5 electrodes could operate as both EC

and counter layers, and the coloration exhibited both anodic and cathodic colorations of V_2O_5 films.

From 1975 to 1999, studies focused on the shift in the absorption–transmission spectra in visible light and the change in light intensity in the IR and NIR regions. Other important key figures of merit to evaluate the performance of ECDs, such as the coloration efficiency, cycling life, and switching time, have attracted less attention. Classical V_2O_5 films for ECDs are usually fabricated by RF magnetron sputtering,[229,231,232] DC magnetron sputtering,[158,233] thermal evaporation,[225,226,234,235] and sol–gel[236–238] methods. The advantage of these techniques is the good adhesion of the film to the substrate. Nevertheless, the compact morphologies decrease the diffusion rate and reversibility. The absorption tail shifted to a higher energy (shorter wavelengths) from 2.25 to 3.1 eV ($x = 0$ to 0.75), from 2.38 to 2.75 eV ($x = 0$ to 11),[158] from 2.7 to 3.4 eV,[226] and from 2.27 to 2.47 eV ($x = 0$ to 0.86)[232] upon lithium intercalation in $Li_xV_2O_5$. The absorption in the NIR and IR regions also increased when cathodically polarized, and the reversibility decreased when anodically polarized. Consequently, the film color varied depending on the applied voltage (or current). For example, the following EC changes have been observed: yellow $\leftrightarrow$ greenish–blue,[226] yellow $\leftrightarrow$ blue,[232] pale-yellow $\leftrightarrow$ gray,[233] yellow $\leftrightarrow$ yellowish,[235] yellow $\leftrightarrow$ green,[236] yellow $\leftrightarrow$ green $\leftrightarrow$ deep-blue,[237] yellow $\leftrightarrow$ light-blue,[239] and blue $\leftrightarrow$ green $\leftrightarrow$ yellow.[240]

Nagase et al. introduced a new coloration using V_2O_5-based composites, such as Au-V_2O_5 and V_2O_5-TiO_2.[234,238] Fig. 17 compares the coloration of pure V_2O_5 and V_2O_5-based composites.[234,238] In the V_2O_5-TiO_2 system (x-TiO_2, $x = 0$ for pure V_2O_5 and $x = 1$ for pure TiO_2), the pristine film color and EC coloration are affected by the x value. The color change of blue $\leftrightarrow$ green $\leftrightarrow$ yellow ($x = 0$–0.3), gray $\leftrightarrow$ yellow ($x = 0.5$), and reddish-brown $\leftrightarrow$ gray $\leftrightarrow$ green $\leftrightarrow$ yellow ($x = 0.7$) occurred as the films were polarized while only a color change of dark-blue $\leftrightarrow$ transparent ($x = 1$) was observed.[238] Similarly, the new coloration of reddish-violet $\leftrightarrow$ green due to the effective dielectric constant of Au grains was observed in Au–V_2O_5.[234]

There are fewer reports on the response time and CE of a compact V_2O_5 film at this stage. The compact granular
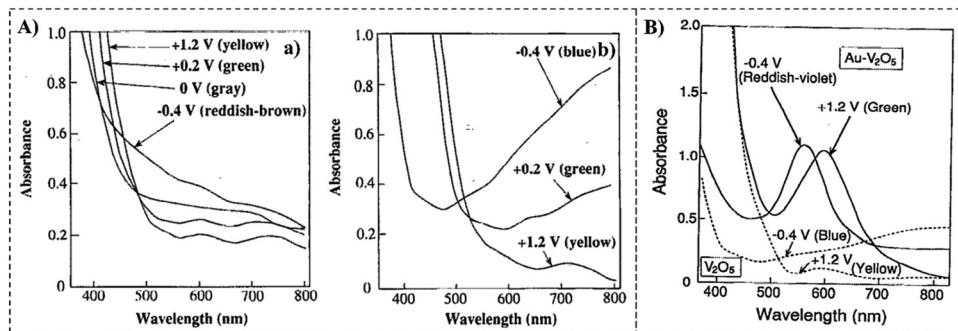
Fig. 17 Optical absorption spectra of (A) V_2O_5–$TiO_2(x)$ films with (a) $x = 0.7$ and (b) $x = 0$ and (B) coloration Au–V_2O_5 films with 26% Au content. The figures are reproduced with permission (Copyright 2022, American Physical Society[234,238]).

morphology of a V_2O_5 film with grains, 80–100 nm in size, produced a low CE value of approximately 13 cm^2 C^{-1} at 630 nm with a slow response time of approximately 60 s and an unsatisfactory reversibility of approximately 70%.[241] The sol–gel V_2O_5 film reached only 30% transmittance modulation at 700 nm when 3.0 V was applied for 5 min and required 10 min to reach saturation. The V_2O_5 film prepared by thermal evaporation showed an increase in transmittance of 48.9% at 400 nm and 14.1% at 700 nm. The E_{opt} increased from 2.03 to 2.62 eV when the amount of intercalated lithium-ions ranged from 0 to 0.54.[201]

Since 2000, various V_2O_5 micro–nanostructure morphologies have improved the CE and switching response time of smart films. Large volume, large specific surface area, and short diffusion distance have made outstanding contributions to the switching response time of ECD. The redox reaction occurs on the surface before diffusion into the inside of the solid. This is favored by the many electroactive sites and favors the charge-transfer resistance.[57] Emphasizing this morphology, 1D nanostructured V_2O_5 as an EC layer, such as NRs,[82,83,150,184] NWs,[59,60,89,90] NBs,[93] and NFs,[57] has been reported.

The NR arrayed film with a 100 nm diameter has a six times faster response rate than the sol–gel thin film.[58] Different 1D-V_2O_5 types were formed by annealing macroporous amorphous phases that showed bleaching-coloration times of 5.6–4.3 s, 8.0–6.5 s, 9.3–8.8 s, and 7.4–8.9 s at 460 nm.[57,83,150] NB-membrane hybrid structures with a width of 20–40 nm fabricated by a hydrothermal method showed a high contrast of 62% with bleaching-coloration time of 7.0–9.9 s at 700 nm.[93] Compared to commercial bulk V_2O_5 with a contrast of 3.8% at 490 nm and a bleaching–coloration time of 8.5–6.6 s, ultra-long NBs (length up 20 mm, width 10–30 nm) inhibit excellent EC with a contrast of 41.6% and a bleaching–coloration time of 4.2–1.4 s.[242] A rapid bleaching–coloration time (2.6–2.8 s) is achieved for NWs with an average width of approximately 15 nm and several micrometer lengths.[89]

The advantages of the solution and chemical methods on the growth of 1D nanostructures allow the easy control of the size, orientation, and morphology. Nevertheless, the weak physical adhesion strength and poor physical/chemical contact with the substrate may decrease the efficiency and redox cycling time. The transmittance modulation of the NRs decreased by approximately 5.6% in the NIR region after 100 cycles.[150] Regarding the NBs, they were peeled off from the substrate after several cycles.[93] This led to a decrease in optical contrast and an increase in transmission of coloration $\Delta T_{colored}$ before and after a certain number of cycles. The contrast decreased by 92.5% after 100 cycles, and $\Delta T_{colored}$ increased 15.33% after 70 cycles.[93]

The 1D-membrane stability was improved by treating the substrate surface, producing a composite or encrusted structure, and employing physical methods. A linear polythylenimine surface treatment of the substrate increased $\Delta T_{colored}$ by only 0.8% after 70 cycles.[93] A polyaniline (PANI) composite with V_2O_5 NWs showed an enhanced switching time compared to the pristine material and maintained cycling stability.[89] Multicolor (black, pale, yellow, light yellow, and dark green) V_2O_5/PANI CDs demonstrated cycling stability for 1000 cycles and rapid bleaching–coloration times of 1.5–2.3 s. The optical contrast retention at 1000 cycles was 85% for MnO_2-entrusted V_2O_5 compared to 80% for bare V_2O_5.[90] V_2O_5 NWs with diameters ranging from 10 to 100 nm and lengths up to several hundred nanometers fabricated by the TE methods were stable for 1000 redox cycles.[60]

Other morphologies of V_2O_5 micro–nanostructures, *i.e.*, NPs,[214,243] stacked multilayer film,[244] and NSs,[245] have been investigated on flexible ECDs. NPs and NSs show excellent contact with a flexible substrate, but the difference in the method and morphology has advantages and disadvantages for each EC material. NP EC materials exhibit long-term cycling with 18% decreased ΔT after more than 30 000 cycles but a slow switching time in the ranges $t_c = 139$–230 s (t_c) and $t_b = 92$–230.[214] Stacked multilayer film exhibits a fast response time with $t_c/t_b = 20.9/34.4$ s and excellent stability with 17.75% decreased ΔT after 2000 cycles.[244] In contrast, ultrathin NS (4 to 40 nm) EC material showed a rapid t_c–t_b of 4.1–6.4 s but has poor stability with 35% decreased ΔT after 100 cycles.[245] Surca *et al.*[243] synthesized NPs (100 nm) using a mechanical milling method, and then the film was coated using a spin-coating technique on ITO-PET before being treated thermally at 150 °C for 1 h. Interestingly, ΔT increases to 6% and 24% after the 41st and 521st cycles, respectively, compared to the 6th cycle.
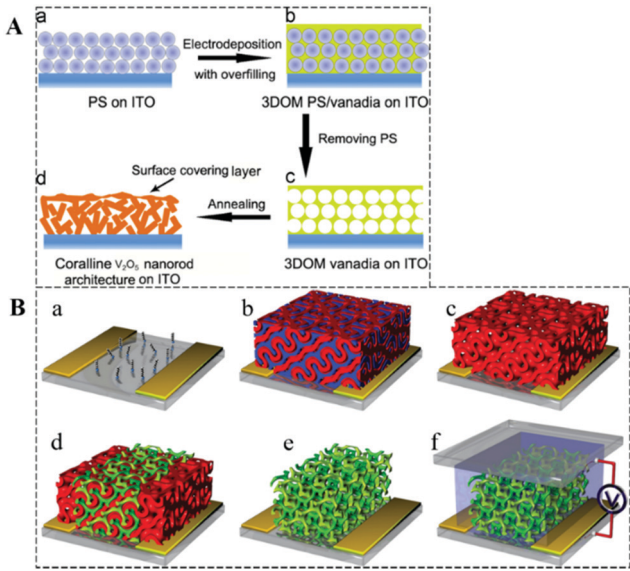
Fig. 18 Schematic diagram of the growth of V_2O_5 nanostructures: (A) 3DOM and NRs and (B) Gyroid morphology. The figures are reproduced with permission (Copyright 2022, Elsevier[150] and Wiley[246]).

In general, V_2O_5 is characterized by slower response times than WO_3. Nevertheless, EC V_2O_5 has superior deintercalation/intercalation capacity with a reduced optical band spectrum. The coloration state can be operated and maintained at a low potential (voltage range of ± 1 V).[16,145] Fortunately, most applications of EC materials, such as EC windows, do not require rapid response times.[124] In particular, to reduce the switching time below 100 ms, the nanostructured device should satisfy the lithium-ions diffusion distance, $x = \sqrt{2Dt} \sim 5$ nm, where D and t are the diffusion coefficient and response time, respectively.[246] This size is approaching the Bohr radius $a_B = 4.52$ nm.[50,247] This affects the bandgap of semiconductor materials because of the quantum confinement effects.

Novel micro–nanostructures, such as three-dimensionally ordered macroporous (3DOM), 3DOM of 1D morphology, and Gyroid structures, were fabricated using the new technique or combination of techniques, as shown in Fig. 18.[150,246] These structures can meet the rapid switching time due to rapid intercalation–deintercalation diffusion. The effective diffusion coefficient D of lithium ions (Li^+) can be estimated from the Randles–Servcik equation (eqn (17)).[57,248]

$$J = 269 \times 10^3 An^{2/3}D^{1/2}C_0\nu^{1/2} \qquad (17)$$

where J, A, n, C_0, D, and ν are the current density at the oxidation state, effective surface area of the electrode (cm²), number of electrons transferred in the unit redox reaction, concentration of diffusion species of electrolyte (mol cm⁻³), effective diffusion coefficient (cm² s⁻¹), and potential voltage scan rate (V s⁻¹), respectively.

The chronocoulometric response under diffusion-limited conditions can be expressed using eqn (18).[249]

$$Q = 2n^{-1/2}FAD^{1/2}C_0t^{1/2} + Q_{dl} + nFA\Gamma \qquad (18)$$

where Q_{dl} and Γ are the double-layer charging and the concentration of adsorbed species participating in the faradaic reaction, respectively.

Li's research group developed EC films of three-dimensionally ordered macroporous (3DOM) and 3D crystalline NRs and NFs.[57,83,89,145,150,249,250] Fig. 19 A presents the 3DOMs with different pore diameters of 210, 340, and 840 nm. The similar thicknesses of 1.1 ± 0.1 μm of dense and 3DOM films resulted in the same solid volume but different surface areas. Compared to the dense film, the 3DOM films showed high transmittance modulation, faster switching response, and high OD because of the increased active area of whole nanostructures, as shown in Fig. 19B and C. Among them, the 3DOM V_2O_5 film with a pore size of 210 nm showed the highest EC performance with $\Delta T = 50\%$ (at 650 nm), $t_c = 1.7$ s, and $t_b = 3.2$ s because this size obeys the short Li^+ diffusion distance and larger active surface areas for more effective Li^+ intercalation.

Steiner's research group grew gyroid-structured electrodes for EC and supercapacitor applications.[246,251,252] The small size of the periodic DG V_2O_5 with a cubic unit cell size of 41.5 ± 1 nm, strut diameter of 11.0 ± 0.3 nm, and high specific surface led to a rapid response time. The short switching time of DG with a t_b/t_c of 82.5 ± 2.9 ms/86.7 ± 2.3 ms was comparable to the inverted opals structure of 122–235 ms. Fig. 20A and B show the cross-sectional SEM images and a schematic diagram of DG for CDs. The photograph and UV-vis-NIR spectrum (Fig. 20C and D) revealed a vivid yellow and green-gray color for the oxidized state at the anode (+3.5 V) and reduced state at the cathode (−3.5 V) for 20 s, respectively. Both anodic and cathodic colorations clearly showed an enhanced absorption peak at approximately 425 nm that decreased sharply in the visible-NIR region. The dynamic optical behavior and the temporal response showed a change in color under an applied potential of ± 1 V that reached the full redox state at ± 3 V, as shown in Fig. 20E.[251]

Moreover, combinations between the V_2O_5 micro–nanostructures and other materials to form a micro–nanocomposite or hybrid structure and enhance the EC performance have been reported: Ag@V_2O_5,[59] MnO_2@V_2O_5,[90] V_2O_5@PEDOT,[112] Carbon@V_2O_5,[207] Carbon@V_2O_5@PEDOT:PSS,[253] Mo@V_2O_5,[248] MoO_3@V_2O_5,[254,255] polymer@V_2O_5,[256] TiO_2@V_2O_5,[257,258] PEDOP@V_2O_5,[259] graphene @poly@V_2O_5,[260] RGO@V_2O_5,[261] SnO_2@V_2O_5,[262] and NiO@V_2O_5.[263] In addition, bi-layer and multi-layer structures, such as WO_3/V_2O_5/WO_3/V_2O_5,[264] TiO_2/V_2O_5,[265] GO/V_2O_5 NSs/GO/V_2O_5 NSs,[245] and V_2O_5 dot-decorated WO_3,[96] improve the optical properties. Metal, GO, RGO, and PEDOT, with high carrier mobility, have higher electrical conductivity, which improves the ECD switching time. Furthermore, owing to volume expansion during cycling, crystalline pure V_2O_5 became amorphous, resulting in a decrease in stability. Vanadium ion dissolution can be inhibited by M@V_2O_5 composite structures, improving durability.[89,266]

Xiong et al.[59] reported the electrochromism applications of V_2O_5 NWs and Ag particle-decorated V_2O_5 (SVO) NWs. The small diameter of both the SVO and V_2O_5 NWs of 10–20 nm showed an advanced switching time due to the short diffusion
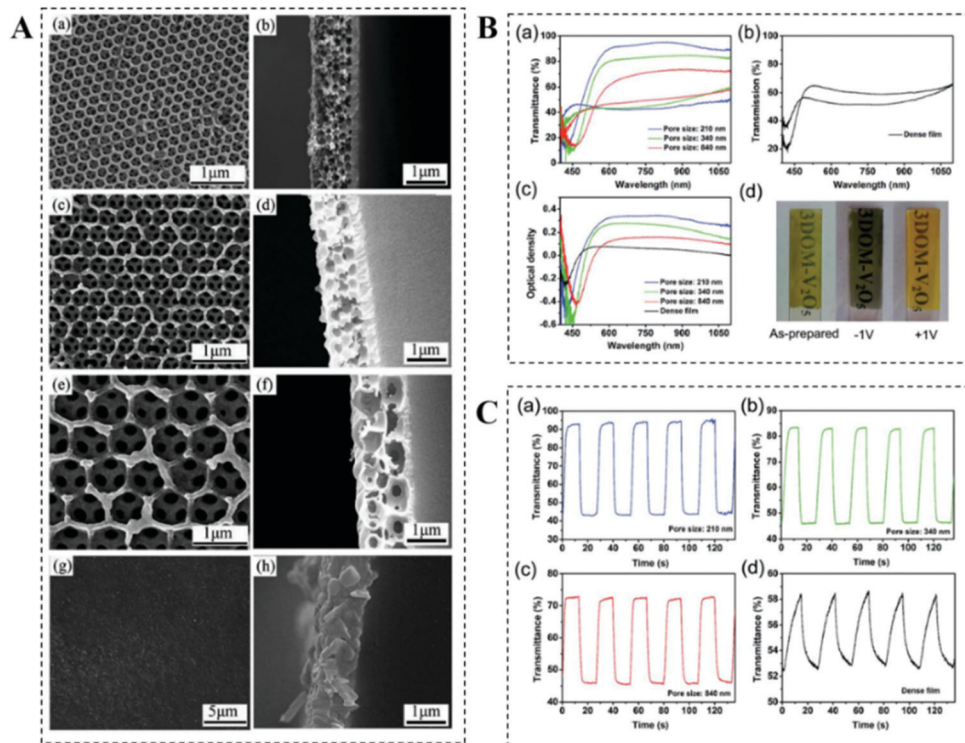
Fig. 19 The electrochromic properties of 3DOM V_2O_5: (A) SEM images of films with different pore sizes: (a and b) 210 nm, (c and d) 340 nm, (e and f) 840 nm, and (g and h) dense film. (B) Transmittance contrast of (a) 3DOM and (b) dense V_2O_5 films, (c) optical density, and (d) digital photographs of 3DOM films with different potentials. (C) Switching response curves of films with different pore sizes: (a) 210 nm, (b) 340 nm, (c) 840 nm, and (d) dense V_2O_5 film, reproduced with permission (Copyright 2022, Royal Society of Chemistry[145]).
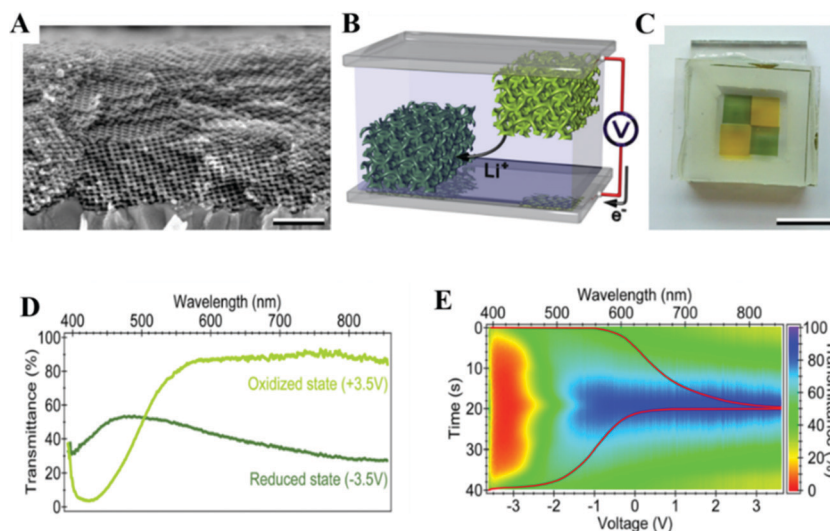
Fig. 20 The electrochromic properties of double-gyroid structured V_2O_5: (A) cross-section SEM image of the DG film, (B) schematic diagram of two laterally offset DG structured electrodes, (C) photograph of ECDs (oxidized state: yellow color and reduced state: green-gray color), (D) transmittance spectra, and (E) transmittance variations during chronopotentiometry (+2 mA cm^{-2} for the initial 20 s and −2 mA cm^{-2} for the remaining time), reproduced with permission (Copyright 2022, American Chemical Society[251]).

distance. The presence of Ag product with more electronic concentration led to better electrical conductivity than that of pure V_2O_5. Consequently, the t_c of SVO was more than 20 times faster than that of pure V_2O_5 NWs because of the enhanced diffusion coefficient. On the other hand, Ag NPs could promote catalytic behavior that leads to an unstable colored state. The
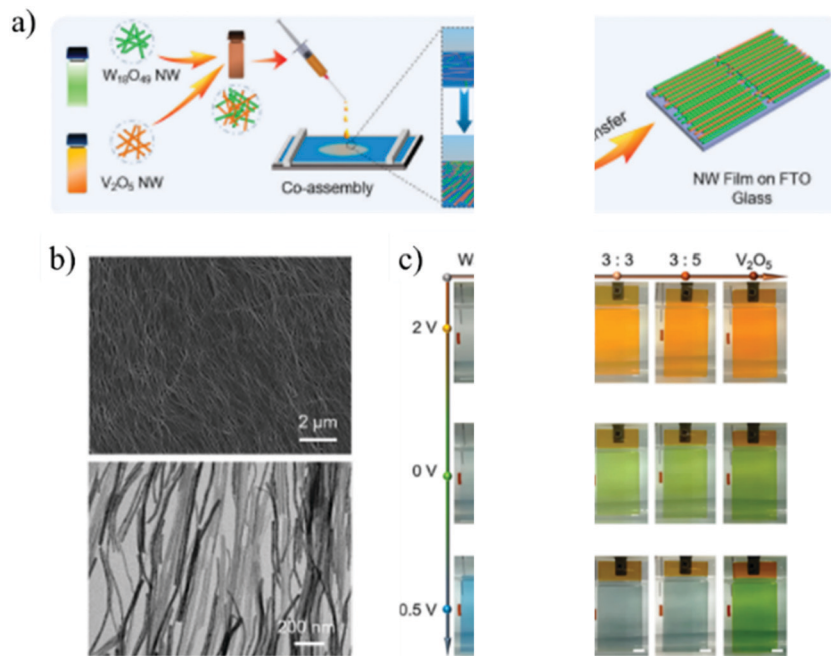
Fig. 21 $V_2O_5/W_{18}O_{49}$ electrochromic: (a) schematic diagram of the co-assembly process, (b) SEM and TEM images (ratio 3 : 3), and (c) optical images upon 2.0 and −0.5 V applied voltages of 10 layers, reproduced with permission (Copyright 2022, American Chemical Society[267]).

high conductivity of the composite due to the contribution of high conductivity materials, such as graphene, GO, RGO, and PEDOP, improves the switching time.[205,259–261]

Composite materials exhibit improved electrical, mechanical, and optical properties yielding durable ECDs. A previous study reported that a SnO_2/V_2O_5 hybrid still maintained 85% optical modulation of the original value after 2000 cycles, while pure V_2O_5 lost almost 90% after 300 cycles.[262] The ΔT and CE of polymer/V_2O_5 composite ECD after being stored for several weeks were approximately 40–30% and 8–20% lower than the initial cycle and after 100 redox cycles, respectively.[256] In particular, the ECD of the V_2O_5–TiO_2 (70 : 30) composite exhibited a high ΔT of 68% at 580 nm and long-term cycling stability with a decreased ΔT of 2% after 150 000 cycles.[257] Wang et al.[267] used Langmuir–Blodgett technique to co-assemble V_2O_5 and $W_{18}O_{49}$ NWs (Fig. 21a and b) with different mass ratios. The colored-bleached states of pure V_2O_5 NWs inhibit orange and green colors while pure WO_3 inhibits the transparent and blue colors with applied voltages of 2.0 and −0.5 V. Multicolors from orange, green, and gray depend on the mass ratio, as shown in Fig. 21c.

Another addition for improving the EC performance is doping. V_2O_5 is an n-type semiconductor with a low electron carrier concentration that leads to low electrical conductivity. The room-temperature conductivity of pure V_2O_5 thin films ranged from approximately 10^{-2} to 10^{-1} Ω^{-1} cm^{-1}.[268] The intercalation/deintercalation processes were strongly affected by electronic conductivities and ionic diffusivities.[269] Towards this direction, the role of doping on the improvement of electrical conductivity (i.e., large carrier concentration) was investigated.[270] The experimental result showed that the

electrical conductivity of element-doped V_2O_5 ($M_xV_{2-x}O_5$) increased from 10^{-3} to $5–7 \times 10^{-1}$ Ω^{-1} cm^{-1} (M = Ag, Cu),[269] and from 4×10^{-4} to 2×10^1 Ω^{-1} cm^{-1} (M = Na).[271]

Ti-, Mo-, W-, Fe-, Ta-, and Mg-doped V_2O_5 showed improved EC performance in cycling stability, switching time, CE, and optical contrast.[108,196,248,272–278] Among them, Ti-doped V_2O_5 showed outstanding properties. Li et al.[272] prepared durable reinforced hybrid type ECDs based on modified Ti-doped V_2O_5 films and solution-phase ethyl viologen. The results showed that the ECDs exhibited long-term cycling stability with only a slight decrease in ΔT after 250 000 cycles. 4% Ti-doped V_2O_5 showed a high ΔT% of 51.1% (at 415 nm) and CE of 95.7 cm^{-2} C^{-1} compared to 36.0% and 53.1 cm^{-2} C^{-1} for pure V_2O_5. Fe-doped V_2O_5 exhibited an enhanced switching speed (t_c = 2.0 s and t_b = 3.7 s) compared to bare V_2O_5 (t_c = 4.6 s and t_b = 6.0 s).[273] A high Mg content (15% Mg-doped V_2O_5) enhanced the visible transmittance of pristine film and improved the CE to 71.3% compared to 9% for pure V_2O_5 (at 560 nm).[108] The transmittance contrast of W-doped V_2O_5 increased with increasing W content (expect ratio V : W = 9 : 1), and its maximum gains were 76.9% (at 560 nm) and 77.5% (at 750 nm) in the V : W = 2 : 1 case.[196] Table 5 lists the EC performance (i.e., t_c/t_b, OD, ΔT, and CE) and illustrates the considerable progress in nanoscience to upgrade the EC parameters of different micro–nanostructural morphologies, doping elements, and hybrid composite structures.

The overlapped colors obtained by combining two EC types between V_2O_5 and other counters were attributed to the various colors using the simultaneous reversible color of two counters in V_2O_5/electrolyte/counter(s) (counters = VO_x, TMOs, polymers). Classical V_2O_5 films were also studied to change the

Table 5 Electrochromism of V_2O_5

Sample	Synthesis method	Evaluation wavelength (nm)	Coloration time (s)	Bleaching time (s)	Optical density (ΔOD)	Transmittance ΔT (%)	Coloration efficiency CE (cm² C⁻¹)	Ref.
One-spin film	The film was deposited on an ITO substrate by sol–gel spin-coating	630	—	—	0.31	37	11.36	236
Two-spin film			—	—	0.55	56	12.5	
Film – 250 °C	The film was deposited on an FTO substrate by sol–gel spin-coating, was annealed at different temperatures	420	4.5	4.0	0.897	18.46	33.22	343
Film – 350 °C			2.7	2.2	1.277	51.76	49.13	
Film – 450 °C			2.4	2.1	1.730	56.09	110.98	
Film – 3% O₂ (300 °C)	The films grown by RF-sputtering at different O2/Ar gas ratios and different substrate temperatures	400	—	—	1.93	30.39	52.9	350
		560			0.479	27.5	13.1	
		750			0.35	18.6	9.6	
Film – 6% O₂ (300 °C)		400	19.5	20.25	1.81	35.14	73	
		560			0.22	14.6	8.87	
		750			0.28	17.5	11.4	
Film – 11% O₂ (300 °C)		400	—	—	1.97	36.9	84.5	
		560			—	0.0	—	
		750			0.21	9.6	9.1	
Film – 25 °C (6% O₂)		400	—	—	0.65	21.3	35.3	
		560			0.41	25.8	21.9	
		750			0.41	23.9	22.1	
Film – 150 °C (6% O₂)		400	—	—	1.61	33.2	131.9	
		560			0.39	25.8	32.5	
		750			0.28	17.66	23.2	
Film – 300 °C (6% O₂)		400	20	20	1.81	34.7	73	
		560			0.22	14.6	8.9	
		750			0.28	17.5	11.4	
Film – 375 nm	The film was deposited on an ITO substrate by sol–gel spin-coating	800	6	6	0.85	80	14	237
Film: 250 (fresh)	V_2O_5 was prepared on FTO by electrophoretic deposition and was treated with isopropanol	700	3	—	0.21	40	18	181
Film: 250 (aged)			5.1	—	0.26	43.15	22.4	
Film: 420 (fresh)			5.90	—	0.28	47.30	20.20	
Film: 250 (aged)			8.7	—	0.38	50.20	25	
Film: 780 (fresh)			18.80	—	0.41	50.40	18.70	
Film: 780 (aged)			18.0	—	0.57	57.90	26.30	
Film – 3 min (240 nm)	The films were prepared by CBD at 85 °C for different deposition times (min)	400	20	56	—	55	—	124
		500	—	—	—	23	—	
		900	—	—	—	17	—	
Film – 20 min (830 nm)		400	—	—	—	1	—	
		500	—	—	—	28	—	
		900	61	36	—	55	—	
V_2O_5 particles (65 nm) 0.1 V	The films were inkjet printed from a gel on PET/ITO, EC measurement with different applied voltages (V)		230	230	—	4.1	42	214
0.5 V			192	170	—	20.4	40	
1.1 V			184	118	—	37.1	30	
1.5 V		750	143	103	—	39.6	16	
Templated 2%	WCR (layered structured with different polymer concentrations)	600	30	39	—	18.0	25.0	82
Templated 10%			29	27	—	17.4	27.0	
Templated 20%			30	38	—	20.0	57	
NBs-membrane	NBs were fabricated by the hydrothermal method and drop-casted on ITO	700	7.0	9.9	—	62	20.7	93
Powder	Commercial	490	6.8	8.5	—	3.8	8.4	242
NBs	NBs were fabricated by the simple solution treatment process		1.4	4.2	—	41.6	83.3	
NFs	V_2O_5 was deposited into PS colloidal crystal templates, and the film was annealed at 450 °C for 4 h	450	8.9	7.4	—	34	32	57
NWs	NWs were grown on ITO using the TE method	415	6	5	—	37.4	—	60
Dense film	V_2O_5 was deposited into PS colloidal crystal templates with different sizes of PS by the ECAD method. A dense film was grown without a template	450	13.1	13.5	—	16	—	145
		650			0.07	10	—	
		900			0.05	4	—	
3DOM with pore size 210 nm		450	1.7	3.2	—	24	—	
		650			0.33	50	—	
		900			0.31	47	—	
3DOM with pore size 340 nm		450	2.2	5.7	—	26	—	
		650			0.28	38	—	
		900			0.23	30	—	

Table 5 (*continued*)

Sample	Synthesis method	Evaluation wavelength (nm)	Coloration time (s)	Bleaching time (s)	Optical density (ΔOD)	Transmittance ΔT (%)	Coloration efficiency CE (cm^2 C^{-1})	Ref.
3DOM with pore size 840 nm		450	3.0	3.5	—	19	—	
		650			0.15	19	—	
		900			0.15	18	—	
Macroporous Nano-gyroid	V_2O_5 network was electro-chemically deposited onto a mesoporous template (DG morphology)	430	0.122	0.235	0.57	14.1	24×10^4	246
			0.082	0.086	0.97	49.8	33.9×10^4	
3D ordered macroporous (3DOM)	V_2O_5 was deposited into PS colloidal crystal templates, and the film was annealed at different temperatures for different annealing times	460	2.3	4.5	—	34.01	83.6	83
		1000			0.07	16.41		
3DOM – 250 °C – 4 h		460	1.7	4.5	—	18.49	88.1	
		1000			0.18	20.89		
3DOM–300 °C – 4 h (curving platelets)		460	5.7	7.1	—	29.85	88.3	
		1000			0.28	31.62		
3DOM – 350 °C – 4 h (NRs)		460	6.5	8.0	—	38.48	98.5	
		1000			0.25	28.94		
3DOM – 350 °C – 7 h (3D NRs)		460	8.8	9.3	—	27.43	96.9	
		1000			0.27	36.69		
NWs	Pure and Ag-doped V_2O_5 were hydrothermally synthesized, and a suspension containing NWs was dip-coated onto ITO	633	6	1	—	32	—	59
Ag-V_2O_5 NWs			0.2	0.1	—	54	—	
V_2O_5 NWs (−3.0 V; +3.0 V)	NWs were fabricated by the solvothermal method, MnO_2 was coated onto V_2O_5 by the electrodeposition method	550	1.57	—	—	30.78	51.66	90
V_2O_5 NWs (−2.5 V; +3.0 V)			2.06	—	—	26.35	52.87	
MnO_2/V_2O_5 NWs (−3.0 V; +3.0 V)			5.91	—	—	26	32	
MnO_2/V_2O_5 NWs (−2.5 V; +3.0 V)			4.39	—	—	23.81	45.59	
V_2O_5 NWs	NWs were fabricated by the WCR method, V_2O_5/PANI composites were prepared by the in-situ polymerization method	665	2.8	2.6	—	40	—	89
V_2O_5/PANI composite NWs			2.3	1.5	—	40	—	
V_2O_5 film	NiO film was deposited by the CBD method, V_2O_5 was deposited on ITO and NiO/ITO by the ED method	776	3	4	0.77	30	24.5	263
NiO/V_2O_5 hybrid film			8	11	0.97	35	30.6	
V_2O_5 film	SnO_2 nanoflake array was prepared by the hydrothermal method, the V_2O_5 film was deposited on FTO and SnO_2/FTO by the ED method	450	7	6	0.45	37	66	262
SnO_2/V_2O_5 film			5	8	0.6	47	118	
V:W (1:0)	Mixed W/WO_3–V_2O_5 (W-doped V_2O_5) films were deposited on an FTO substrate by sputtering with different W/V ratios	560	19.5	20.2	0.15	9.10	10.48	196
		750			0.21	12.24	14.68	
V:W (28:1)		560	20.7	25.6	0.20	15.08	11.89	
		750			0.13	9.40	7.37	
V:W (14:1)		560	14.7	11	0.26	19.17	21.66	
		750			0.17	12.02	14.08	
V:W (9:1)		560	16	8.5	0.22	14.44	10.52	
		750			0.12	7.86	5.69	
V:W (7:1)		560	25.8	11.1	0.30	20.10	13.89	
		750			0.34	21.37	15.34	
V:W (3.5:1)		560	47.3	15.5	0.98	44.30	24.12	
		750			0.92	45.30	22.64	
V:W (2:1)		560	68.7	33.3	3.95	76.90	41.15	
		750			3.96	77.50	41.26	
V_2O_5/ITO	Pure and V_2O_5@PEDOT films were fabricated on ITO/PET and MoO_3/PET substrates by the RFRP method	650	6.2	2.5	—	6.8	37	112
V_2O_5/MoO_3			15	14	—	10.95	28	
V_2O_5–PEDOT/ITO			10	14	—	7.1	24	
V_2O_5–PEDOT/MoO_3			16	3	—	16.9	53	
0% Ti-V_2O_5	Ti-doped V_2O_5 films were deposited on an ITO substrate by the ED	415	6	6	—	36	53.1	276
4% Ti-V_2O_5			6	8	0.68	51.1	95.7	
10% Ti-V_2O_5			5	6	0.51	39.7	63.0	

Table 5 (continued)

Sample	Synthesis method	Evaluation wavelength (nm)	Coloration time (s)	Bleaching time (s)	Optical density (ΔOD)	Transmittance ΔT (%)	Coloration efficiency CE (cm² C⁻¹)	Ref.
20% Ti-V_2O_5	method using a gel precursor solution		9	15	—	11.2	54.7	
V_2O_5/TiO_2	The film was deposited by electrodeposition from mixture solution V_2O_5 and TiO_2 (70 : 30)	580	5	4	1.7	68	72	258
0% Mg-V_2O_5	Mg-doped V_2O_5 films were deposited by the RF sputtering method	560	19.5	20.5	—	14.8	9	108
		750			—	17.3	11.2	
6.7% Mg-V_2O_5		560	—	—	—	33.6	22	
		750			—	27	18.6	
15% Mg-V_2O_5		560	10	4	—	34.4	71.3	
		750			—	21.4	44.5	
V_2O_5–polymer (1st cycle)	V_2O_5–polymer hybrid particles were prepared by the self-organization method; the films were inkjet printed from solution on ITO. The cycling stability of electrochromism was evaluated	450	23	20	3.354	33	86	256
20th cycle			24	22	3.003	30	77	
100th cycle			20	27	2.448	25	72	
After storing			24	27	1.96	20	56	
V_2O_5	V_2O_5 NSs/GO composites were prepared by the liquid-phase exfoliation method, and then were deposited on the ITO/PET substrate	425	4.1	6.1	—	41.8	21.66	245
VG–1			0.9	1.1	——	32.7	—	
VG-2			1.3	1.7	—	45.1	38.9	
VG-4			1.6	2.0	—	57.5	43.69	
VG-6			2.3	3.6	—	60.2	32.57	
Bare VR	V_2O_5 NRs/GO films were prepared on FTO by sol–gel spin-coating	415	5.6	6	—	42.60	—	205
VR/G1			3.4	5.2	—	40.99	—	
VR/G2			1.4	2.5	—	40.92	—	
VR/G3			2.3	4.1	—	40.78	—	
V_2O_5	V_2O_5 sol was prepared by the melt quenched method, and then it was mixed with RGO. Mixture of the solution was ultrasonicated.	633	6.3	11.8	—	25.5	5.9	
V_2O_5/RGO			4.4	7.3	—	34.9	11.3	261
Pure V_2O_5	The graphene/poly (ethylene oxide)/V_2O_5 composites were prepared by the sol–gel method	650	4.6	2.4	—	19.64	—	260
Poly/V_2O_5			5.2	1.8	—	21.14	—	
Graphene/V_2O_5			2.0	4.0	—	26.48	—	
Graphene/poly/V_2O_5			3.8	1.8	—	30.28	—	
Pure V_2O_5	V_2O_5–MoO_3 films were grown on an FTO substrate by the PSPT method from mixed solution	630	23	20	0.14	17	14.96	255
5% MoO_3 mixed V_2O_5			32.14	46.39	0.16	14	19.96	
10% MoO_3 mixed V_2O_5			30.06	52.36	0.24	23	29.81	
15% MoO_3 mixed V_2O_5			23.50	48.39	0.31	25	35.27	
V_2O_5/WO_3	V_2O_5/WO_3 films were grown on an ITO substrate by the hydrothermal method	550	3.5	4.1	—	87.8	19.76	218

color as a counter electrode in Li_xWO_3/electrolyte/V_2O_5 devices.[229,231–233] The electrochemical reaction of lithium-ions in WO_3 could be transferred to V_2O_5 following α-Li_xWO_3 + V_2O_5 ⇌ α-WO_3 + $Li_yV_2O_5$.[232] Therefore, the combination of a change in light transmittance intensity in WO_3 and the change in color in V_2O_5 acts as a complementary pair in an ECD.[232]

The single V_2O_5 film suppressed the 500 nm absorption and a slight increase in the broad absorption in the NIR region, while the OD of the Li_xWO_3/PC and $LiClO_4$/V_2O_5 modulations gained near zero at 500 nm and increased strongly in the NIR region (Fig. 22). The color of the ECDs in colored-bleached states is dark green-blue and a very pale blue, respectively.[229] The ECD using the WO_3/Ta_2O_5/LiPON/V_2O_5 structure exhibited an increase in ΔT from 19.1% (at cycle 1500) to 24.9% (at cycle 5000).[279] The T_c of V_2O_5/LiPON/Li_xWO_3 increased from 12% (at cycle 5) to 13.7% (at cycle 500).[280] The simultaneous reversible color changes of Mo-V_2O_5 (orange ↔ blue ↔ green) and WO_3 (blue ↔ white) were also combined.[248]

Park et al. studied the overlapped color on PET/ITO/polyaniline NFs/electrolyte(C_2H_3N–$C_4H_6O_3$–$LiClO_4$)/V_2O_5/ITO/PET.[281] The ECDs and skin-attachable strain sensor (SASS) were integrated on the skin using an Arduino circuit, as shown in Fig. 23. The redox processes in polyaniline and (de)-intercalation of ions in the V_2O_5 film occur simultaneously because of the participation of both ClO_4^- and Li^+ from the $LiClO_4$ gel electrolyte. The change in color from pale yellow to dark blue (polyaniline film) and from yellow to green (V_2O_5 film) resulted in ECD exhibiting a wide color range from yellow to dark blue, as shown in Fig. 23C and D. ECD exhibited high CE values of 56.88 cm² C⁻¹ (dark blue) and 65.44 cm² C⁻¹ (yellow), stable
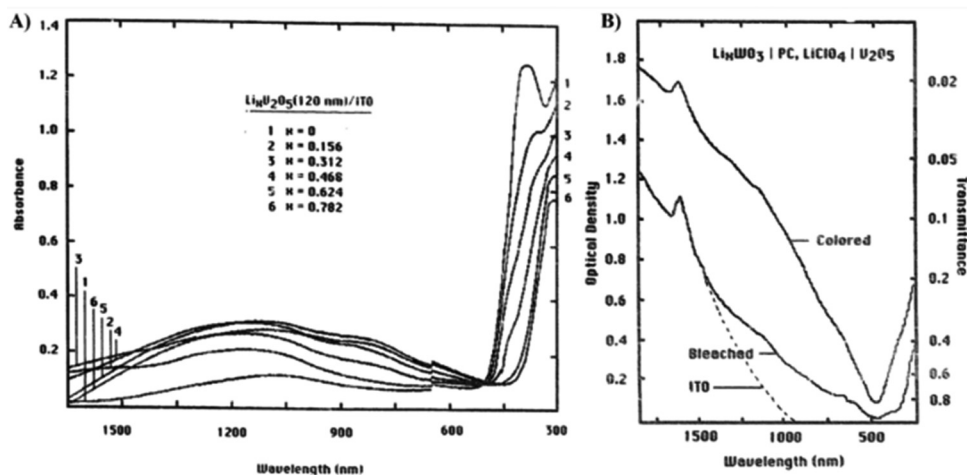
Fig. 22 Optical density and transmittance of $Li_xV_2O_5$: (A) as a function of x (x = 0–0.782) and (B) Li_xWO_3/$LiClO_4$-propylene carbonate/V_2O_5 modulation, reproduced with permission (Copyright 2022, Elsevier[229]).
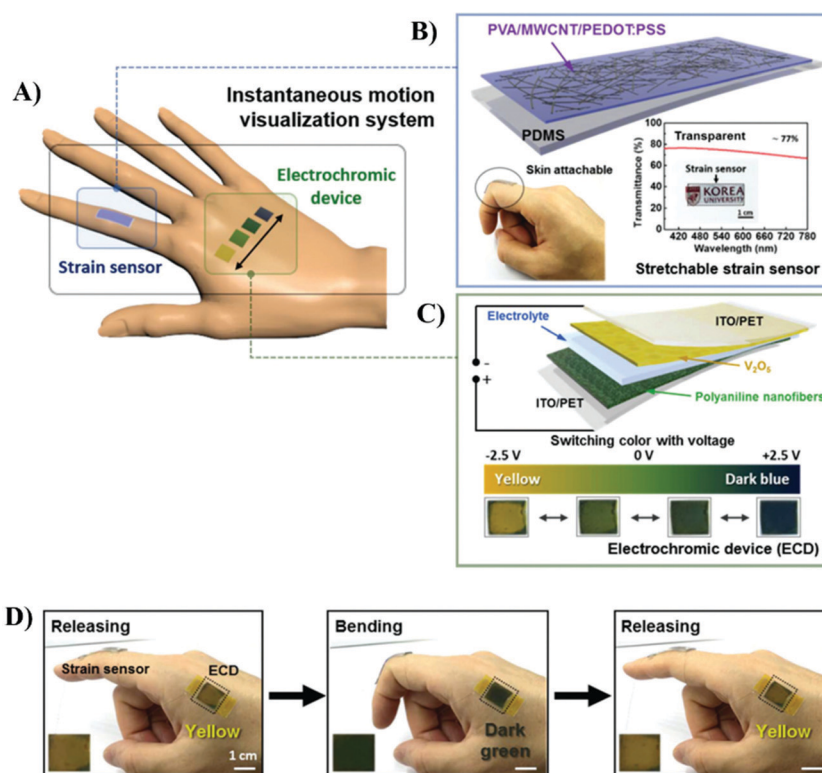
Fig. 23 Schematic diagram of an integrated system based on ECD and SSAS: (A) The interactive color-changeable system of an ECD and SASS on hand skin, (B) SASS using the PVA/MWCNT/PEDOT:PSS nanocomposite on a PDMS substrate and transmittance spectrum of SASS (inset), (C) ECD and photograph of color change from yellow to dark green, and (D) the color changes together with finger motions, reproduced with permission (Copyright 2022, Royal Society of Chemistry[281]).

cycling, and rapid switching response times of t_b = 2.6 s and t_c = 1.5 s; thus, it is a suitable adapter with a strain sensor.

V_2O_5 exhibits multifunctional activity, such as battery, supercapacitor, electrochromism, and photovoltaic activities. ECDs and energy storage of V_2O_5 have a common operating mechanism (charge–discharge).[282] Overall, the ECDs can be combined with energy conversion and storage devices. Nevertheless, they have many features in common, including materials, structure requirements, and operating mechanisms, and discrepancies regarding CE. Specifically, a high CE (*i.e.*, low charge density) and rapid response time are necessary for ECDs. On the other hand, batteries or supercapacitors require a high charge density. The proposed strategies to improve the performance include doping through the addition of Ti in

Fig. 24 Incorporation of EC materials and other devices: (A) Schematic diagram and photograph of EESDs: (a) Zn–SVO EESDs, (b) color overlap *via* the incorporation of orange, yellow and green colors, (c) transmittance spectra, (d) orange color display with an OCP of 1.56 V, (e) 0.5 V reg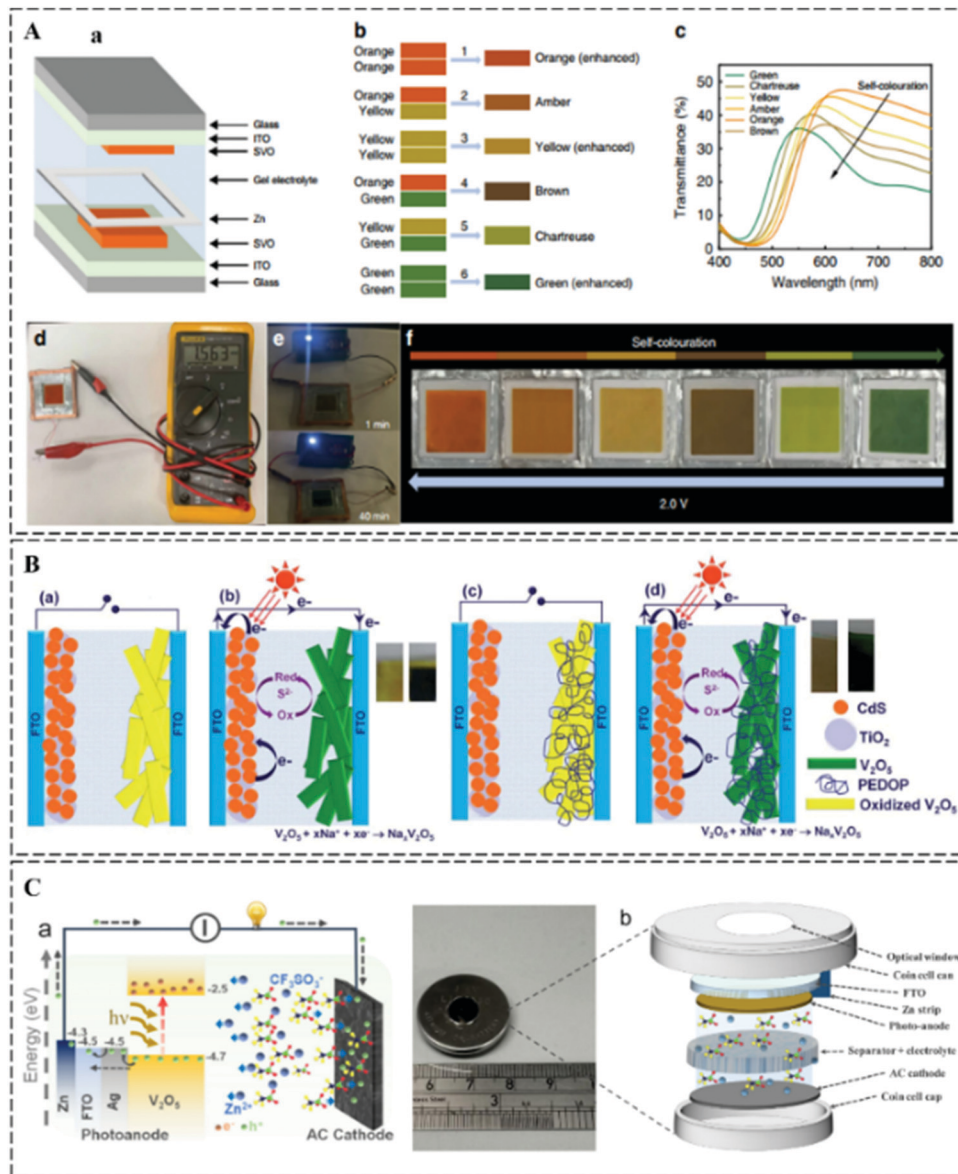ulated LED powered by the Zn-SVO EC display at 1 and 40 min, (f) six colors of Zn-SVO display. (B) Schematic diagram of PECDs: (a and c) pristine V_2O_5 NB and PEDOP/V_2O_5 NB hybrid, (b and d) the coloring counter electrodes of V_2O_5 NB and PEDOP/V_2O_5 NB hybrid. (C) Schematic diagram of PRESDs: (a) Ag@V_2O_5 photoanodes and AC cathodes, (b) photograph of the designed optical coin cell with an optical window (diameter is 8 mm) and its schematic illustration. The figures are reproduced with permission (Copyright 2022, Nature,[184] Royal Society of Chemistry,[259] and American Chemical Society[286]).

V_2O_5[283] to promote lattice distortion and the increase in ion insertion kinetics along with the addition of another oxide, such as MnO_2, providing enhanced stability and increased energy storage performance.[90]

Furthermore, V_2O_5 has a unique band structure allowing it to absorb almost the entire solar spectrum. Therefore, the incorporation of EC materials and batteries (or supercapacitor) to form EC energy storage devices (EESDs),[184,283–285] using a solar cells and EC materials to form photo-electrochromic devices (PECDs),[259] using the battery (or supercapacitor) with a solar cell to form photo-recharge energy storage devices

(PRESDs) and using solar cells and CDs to form photovolta-chromic devices (PVCDs)[286] are an advantage in energy-saving applications. Fig. 24 shows the three moduli, including EESDs (Fig. 24A), PECDs (Fig. 24B), and PRESDs (Fig. 24C).

Zhang *et al.*[184] fabricated a Zn–sodium vanadium oxide (Zn–SVO) EC display by sandwiching Zn foil between two SVO electrodes, as shown in Fig. 24A(a). The SVO electrode was deposited on the ITO substrate using a bar-coating method from a solution containing V_2O_5 NRs. The combination of two electrodes led to an overlay color, resulting in six colors (orange, amber, yellow, brown, chartreuse, and green)

(Fig. 24A(b and f)) compared to a single SVO electrode demonstrating three colors (orange, yellow, and green). Fig. 24A(d) shows the fully charged state (orange-colored) of the device, which means a battery with an open-circuit potential of 1.56 V and provides power to an LED. Nevertheless, the orange hue of the display may be regained using a charging procedure in which Zn is plated onto Zn foil, and Zn^{2+} is removed from the reduced SVO electrode. $Zn^{2+}/2e^-$ intercalation produces a large amount of V^{4+} and a small amount of V^{3+}.[34]

The performance could be further enhanced utilizing hybrid systems, such as Zn^{2+}/Al^{3+}, because Zn^{2+} ions have poor kinetics affecting the capacity, switching, and CE of the EC material. In contrast with Zn^{2+}, Al^{3+} can enhance the performance because of its tri-valence and small ionic radius.[283] Hence, the hybrid electrolyte system can overcome any disadvantages arising from either Zn^{2+} or Al^{3+} and promote a new approach to enlarge the activity of materials used in EESDs. Wang et al.[283] combined many strategies, such as materials (Ti-doped V_2O_5, PEDOT:PSS/ inorganic composites, and hybrid Li/Al-ion electrolyte) chromogenic counters (V_2O_5 and WO_3), and electronic multifunction devices (EC and energy storage devices) to design new three-electrodes (two EC films and one metal frame as anode). The device exhibited high capacity, multicolor (light yellow, transparent, light red, dark green, dark blue, and black), rapid switching, and long-term stability.

Reddy et al.[259] prepared PECDs using pure V_2O_5 or PEDOP/ V_2O_5 composite energy storage-photoelectrochromic cells and the CdS/TiO_2 solar cell, as shown in Fig. 24B. Electron–hole pairs were generated in the CdS/TiO_2 layer. These electrons were transferred by an external circuit and caused the intercalation of Na^+ on the opposite side. Consequently, the PEDOP/ V_2O_5 film was charged as a storage battery, and the color of the film changed from yellow to green. The bleaching process occurred when sunlight was blocked or in the dark. In contrast, Boruad et al.[286] prepared a zinc-ion capacitor (ZIC) using a Ag@V_2O_5 NFBs photoanode and an activated carbon (AC) cathode as the hν-ZIC devices, as shown in Fig. 24C. The electron–hole pairs were generated directly in Ag@V_2O_5 with light irradiation. These holes were transferred to an AC cathode by an external circuit while electrons accumulated on Ag@V_2O_5 NFBs. The anions diffused to the AC cathode, and cations were inserted inside the photo-anode for photo charging. This process can occur simultaneously through three mechanisms: photoconversion, photo-capacitor, and photo-electrochromic.
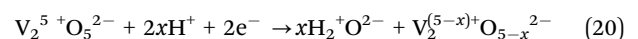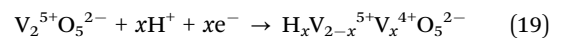
CDs are also used to visualize the reduction/oxi-dation states and to determine the cycle life of energy storage devices (ESDs) without the need for destructive analysis or extra techniques.[284,285] Zhang et al.[284] fabricated 1D V_2O_5 NRB and 2D exfoliated graphene NSH hybrid (EG/V_2O_5) for stimulus-responsive micro-supercapacitors and EC windows. The EG/ V_2O_5 devices exhibited supercapacitance (with an ultrahigh energy density and an ultra-fast responsive time) and an excellent reversible EC. The EG/V_2O_5 device exhibited stimulus-responsive behavior through the relationship between the color change and absorption spectroscopy during the charge–discharge process (0 ↔ 1 V), as shown in Fig. 25A.

When the voltage reached 1V, the device showed the deepest purple color and highest absorbance, and then became colorless and exhibited lowest absorbance at 0V. The cycle life of ESDs can be gleaned through its relation to cation intercalation and photonic crystal (PhCs) in periodicity of materials. The charge–discharge process of metal ions at different rates alters the ordered periodicity because of the crystal structure change, leading to PhC variations and color changes (Fig. 25B).[285] The phase change may be exploited to aid real-time diagnostics by monitoring the color of inverse opal V_2O_5 during charge–discharge operations.

5.3. Gasochromic process in V_2O_5

5.3.1 Fundamentals of gasochromic V_2O_5. Gasochromism of metal oxides, which involves a H^+ intercalation-de-intercalation process due to oxidation and reduction, is similar to the EC mechanism. Therefore, GC phenomena have often been confused with electrochromism. Unlike the ECDs that need an external bias or electric current to drive color switching, the GC phenomenon is activated via a redox reaction of a solid interacting with a gas directly. The working principle can be used for gas sensors and optical sensors in addition to building windows. The electrical and optical properties varied under exposure to various gases, such as methanol, ethanol, acetone, isopropanol, ammonia, and hydrogen.[4,182,287–290] Among them, hydrogen is the most common gas used as a redox gas in gasochromism.

To comprehend the fundamentals of gasochromism in V_2O_5, Fig. 26 summarizes the process of coloration (bleaching) of V_2O_5 with hydrogen (oxygen) gas, which is similar to the mechanism of WO_3.[291–293] The hydrogen molecules (H_2) are dissociated catalytically by using platinum (Pt) or palladium (Pd) to form H^+ ions at the surface (Fig. 26A(1)). They then diffuse into the interior between the layer structure and the pore surface of V_2O_5 (Fig. 26A(2)). The H atoms migrate to the V_2O_5 surface and interact with the lattice oxygen of V_2O_5 (Fig. 26A(3) and eqn (19)).[294] The H^+ diffuses along the surface via water molecules adsorbed on the surface, and electron diffuses into the subsurface. Finally, the oxygen vacancies are generated and diffuse into the interior, followed by the escape of water formed by the hydrogen and surface oxygen (Fig. 26A(4) and eqn (20)). Protons continuously diffuse internally from the surface through favorable planes or sites. For the bleaching process, oxygen molecules (O_2) are adsorbed and dissociated on Pt to O^{2-} ions (Fig. 26B(1)). These ions transfer to the surface and diffuse into the pores of V_2O_5 (Fig. 26B(2)), diffuse internally, and react with oxygen vacancies (Fig. 26B(3)). The resulting oxygen vacancies diffuse to the near surface (Fig. 26B(4)). The protons migrate to the surface, and hydrogen is oxidized at the surface by O^{2-} ions to form the original V_2O_5 and water molecule (eqn (21)).

$$V_2^{5+}O_5^{2-} + xH^+ + xe^- \rightarrow H_xV_{2-x}^{5+}V_x^{4+}O_5^{2-} \quad (19)$$

$$V_2^{5+}O_5^{2-} + 2xH^+ + 2e^- \rightarrow xH_2^+O^{2-} + V_2^{(5-x)+}O_{5-x}^{2-} \quad (20)$$
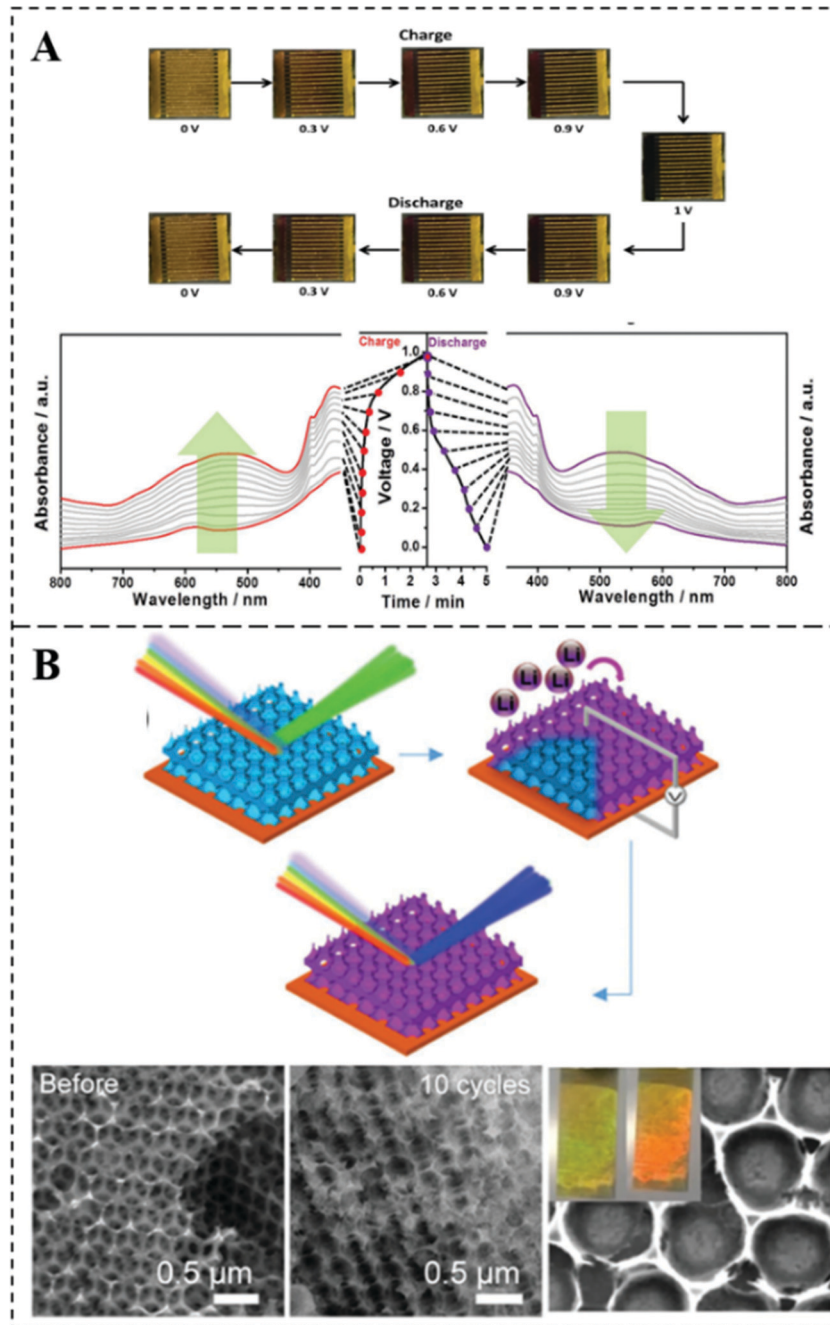
Fig. 25 V_2O_5 ECDs for visualizing and gleaning electrochemical properties: (A) photographs and UV-vis spectra of the electrochromic EG/V_2O_5-MSCs at different voltages and (B) schematic representation of Li-induced variation and SEM images of IO V_2O_5; inset: the variation in color change as a result of charge/phase change. The figures are reproduced with permission (Copyright 2022, Wiley[284,285]).

$$2H_xV_{2-x}^{5+}V_x^{4+}O_5^{2-} + xO^{2-} \rightarrow xH_2^+O^{2-} + 2V_2^{5+}O_5^{2-} + xe^-$$

(21)
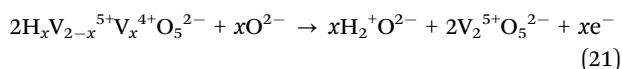
These processes cause structural rearrangement and reduce V^{5+} to V^{4+} and V^{3+}. Hydrogen ions can react with oxygen at O(1), O(2), or O(3) to form localized H_2O molecules and produce an oxygen vacancy. Chen *et al.*[295] used XRD, XAS, and EXAFS to analyze the reduction effect during the GC reaction. XRD showed that the peak of colored V_2O_5 shifted to a higher 2θ angle than the bleached state, indicating that the interlayer distance was altered, as shown in Fig. 27A. Therefore, hydrogen insertion changes a transition and thus the electronic structure. Fig. 27B shows the V L-edge and O K-edge XAS to reveal the electronic structure. Two prominent peaks at 514–521 eV and 521–528 eV of the V L-edge are due to the electron transitions from the V $2p_{3/2}$ and $2p_{1/2}$ energy levels to the V $3d$ unoccupied state, and two pre-peaks at 529–534 eV originated from the O 2p states hybridized with the V 3d-t_{2g} (3d$_{xy}$,
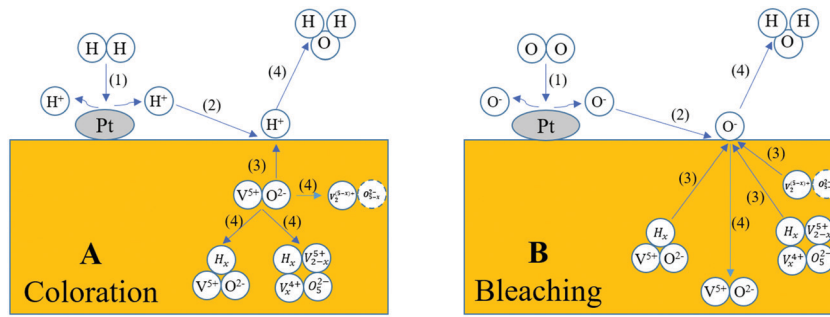
Fig. 26 Schematic diagram of the gasochromic mechanism: (A) coloration by hydrogen and (B) bleaching by oxygen.
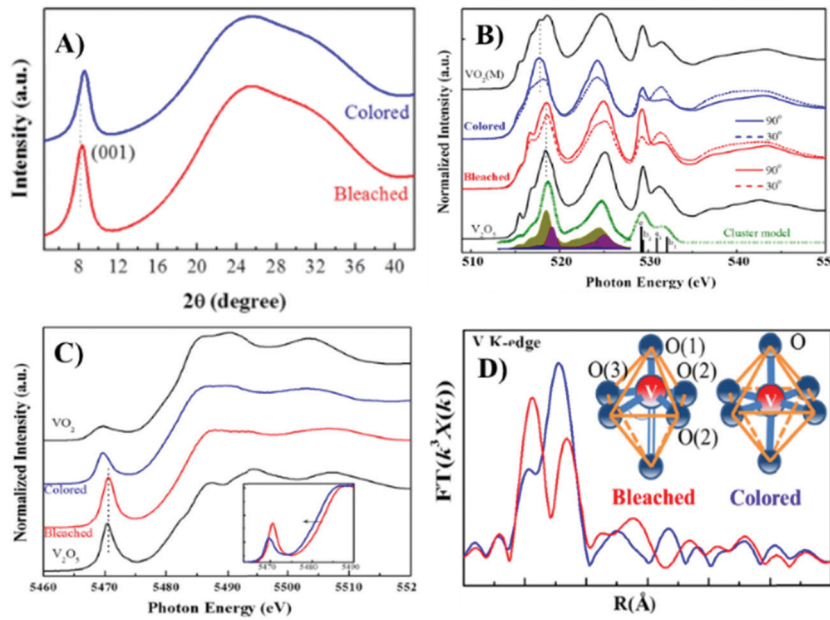
Fig. 27 Gasochromic properties of the V_2O_5 film: (A) XRD patterns, (B) V L-edge and O K-edge spectroscopy, (C) V K-edge XAS spectra, and (D) EXAFS spectra of bleached and colored states, reproduced with permission (Copyright 2022, IOPscience[295]).

$3d_{yz}$, and $3d_{xz}$) and V 3d-eg ($3d_{x^2-y^2}$ and $3d_{z^2}$) states, respectively. The V L-edge of the colored film was shifted to a lower energy and became featureless compared to the bleached film, suggesting a reduced charge state and a deformed atomic structure. The O K-edge confirmed that the valence decreased as the peak for O 2p-V 3d-t_{2g} decreased upon the GC reaction. In addition, the angle-dependent XAS provided further evidence of structural deformation. The pre-peak of the V K-edge of the colored film shifted to a lower energy and decreased in intensity compared to its bleached state (Fig. 27C), which is consistent with the results of a reduced charge state and structural deformation from the V L- and O K-edges.

To gain insight into the atomic structural rearrangement, a Fourier transform (FT) of the EXAFS $k^3\chi$ data at the V K-edge from k = 2 to 10 Å^{-1} indicates the difference in the radial distribution between the colored and bleached states (Fig. 27D). Curve fitting of the bleached state led the V–O bond lengths in VO$_6$, O(1) = 1.61 Å, O(2) = 1.76 Å, and O(3) = 1.90 Å. In contrast, the colored states involving V–O bonding in

symmetrical Oh are V–O = 1.67 and 1.91 Å. The inset in Fig. 27D shows the increase in symmetry of the VO$_6$ octahedral in colored V_2O_5 compared to the bleached state.

Moreover, the sudden decrease in resistance or increase in conductivity during a gas-phase reaction suggests the exchange of electrons or holes. The rapid response and recovery speeds of the V_2O_5 sensor with hydrogen gas at RT is an evidence of a direct reaction without loading any extrinsic catalysts, such as Pt or Pd.[41]

The behavior of the electrical and optical properties of the V_2O_5 film also changes after exposure to organic vapors. Oxygen molecules in an ambient environment were absorbed facilely on the V_2O_5 surface because of the high electron affinity. They captured the free electrons of the CB to form chemisorbed negatively charged oxygen ions, such as O_2^- and O^-, as shown in Fig. 28A and eqn (22)–(24).[296,297]

$$O_2(\text{gas}) \rightarrow O_2(\text{ads}) \qquad (22)$$

$$O_2(\text{ads}) + e^- \rightarrow O_2^-(\text{ads}) \qquad (23)$$
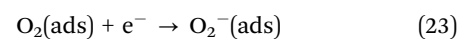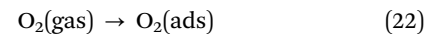
Fig. 28 Schematic diagram of the gasochromic mechanism: (A) In air and (B) in a reducing gas.

$$O_2^-(ads) + e^- \rightarrow 2O^-(ads) \tag{24}$$

When a V_2O_5 film is exposed to organic vapor, the reduction gas is oxidized by the negatively charged surface oxygen ions and releases electrons, as shown in Fig. 28B.[296,297] These electrons move to the entire crystal and fill t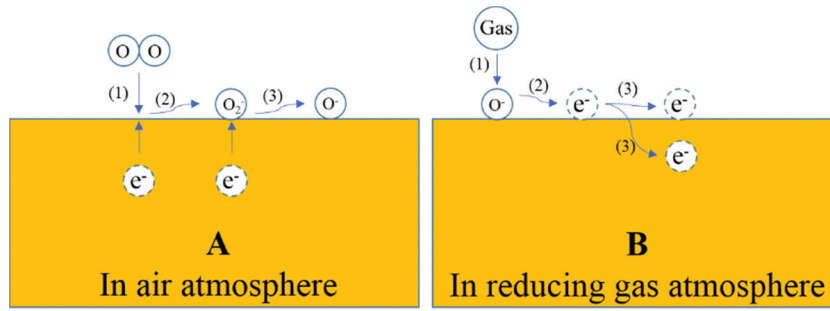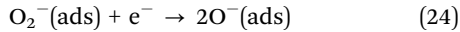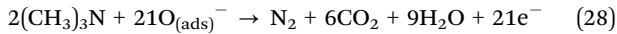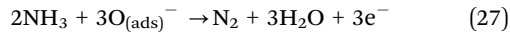he CB, leading to an increase in conductivity and a change in optical transmittance. V_2O_5 exhibits high sensitivity to a range of gases, as defined in eqn (25)–(28).[296,297]

$$C_2H_5OH + 6O_{ads}^- \rightarrow 2CO_2 + 3H_2O + 6e^- \tag{25}$$

$$C_6H_5CH_3 + 3O_{ads}^- \rightarrow C_6H_5COOH + H_2O + 3e^- \tag{26}$$

$$2NH_3 + 3O_{(ads)}^- \rightarrow N_2 + 3H_2O + 3e^- \tag{27}$$

$$2(CH_3)_3N + 21O_{(ads)}^- \rightarrow N_2 + 6CO_2 + 9H_2O + 21e^- \tag{28}$$
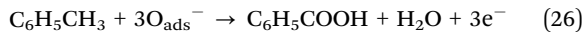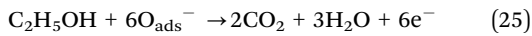
These processes involving exposure to organic gases are similar to the bleaching process using hydrogen. Rizzo *et al.*[289] observed the GC response of the V_2O_5 films to NH_3 by FTIR spectroscopy and compared it with the spectrum of NH_4VO_3. These authors suggested that V_2O_5 NPs react with NH_3 at RT to form ammonium metavanadate (NH_4VO_3), as described in eqn (29). The "bleaching" process for recovering V_2O_5 is achieved by annealing at 350 °C under ambient conditions.

$$V_2O_5 \xrightarrow{NH_3, RT} NH_4VO_3 \tag{29}$$
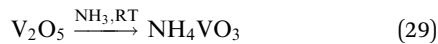
5.3.2 V_2O_5 gasochromic thin films and devices. Gasochromic devices (GCDs), similar to the EC system, have a modular double-glazed unit while the gas for catalysis replaces the electrolyte, as shown in Fig. 10B. Compared to ECDs, GCDs have a slower response time, but GCDs can be produced over a large area. The chromic phenomena of V_2O_5 films exposed to different gases, such as ethanol, methanol, acetone, isopropanol,[287] and ammonia,[289] revealed ΔT modulations. The film color was slightly modified when exposed to ethanol, methanol, and ammonia gases, whereas it did not change when exposed to the remaining gases. The films exhibited an anodic coloration with bleaching when exposed to gas. On the other hand, ΔT reached only 4–5% after 100 min of exposure to methanol or ethanol. The color returned to the initial film color after annealing in air at 350 °C.[289] The low ΔT, slow t_b, and the need for high temperatures to return to the original color have limited the applications to smart windows or switching optical devices.

Liu *et al.*[298] first examined the irreversible color change from yellow to blue and the slight optical modulation of the V_2O_5 film when exposed to hydrogen. The transmittance spectrum shifted strongly toward a shorter wavelength (<500 nm), indicating anodic coloration, whereas it exhibits cathodic coloration at wavelengths longer than 500 nm. The chromic phenomena of vanadium oxide highlight the role of oxygen stoichiometry in the thermodynamic reaction between the hydrogen gas phase and vanadium oxide. The high oxygen stoichiometry samples deposited in the oxygen environment (the TE method) and 5% O_2/Ar (the sputtering method) showed pronounced coloration compared to the samples deposited in the hydrogen environment (the TE method) and without oxygen (the sputtering method). Shanak *et al.*[182] reported the effects of oxygen in terms of the O_2/Ar ratio and thickness on the gasochromism of V_2O_5 films. The low O_2/Ar ratio or very thin films did not reveal clear chromic phenomena (both cathodic and anodic colorations for the first cycle). On the other hand, the films were improved by the increased O_2/Ar ratio and thickness. The higher O_2/Ar ratio and thicker film exhibited anodic coloration only.

The atomic and electronic structures determine the performance of chromogenic materials. Dong's research group has revealed the GC coloration mechanism based on a thin platinum (Pt) layer as a catalyst coated on V_2O_5 thin film to dissociate the hydrogen molecules.[4,288,290,299,300] Different factors, such as synthesis methods (sol–gel and RFS), layer thicknesses, and metal dopant in V_2O_5, were investigated. A VO_x film deposited on a Corning 1737 substrate by RFS showed that the initial film color and colored film were affected by the Ar/O_2 ratio and annealing temperature.[290,300] The different initial color depends on the O_2 concentration and annealing temperature and can affect the GC performance because of the co-existence of V^{4+} of VO_2 and a mixture of V^{4+} and V^{5+} in the as-grown V_2O_5 film.[290,300] The color of the film with an Ar/O_2 ratio of 20:1 remained almost black after gasochromism, whereas the color of the film with Ar/O_2 ratios of 20:3 and 4:1 changed from light yellow to gray. In particular, for the sample prepared in pure O_2, the color changed from deep yellow to dark gray.[300]
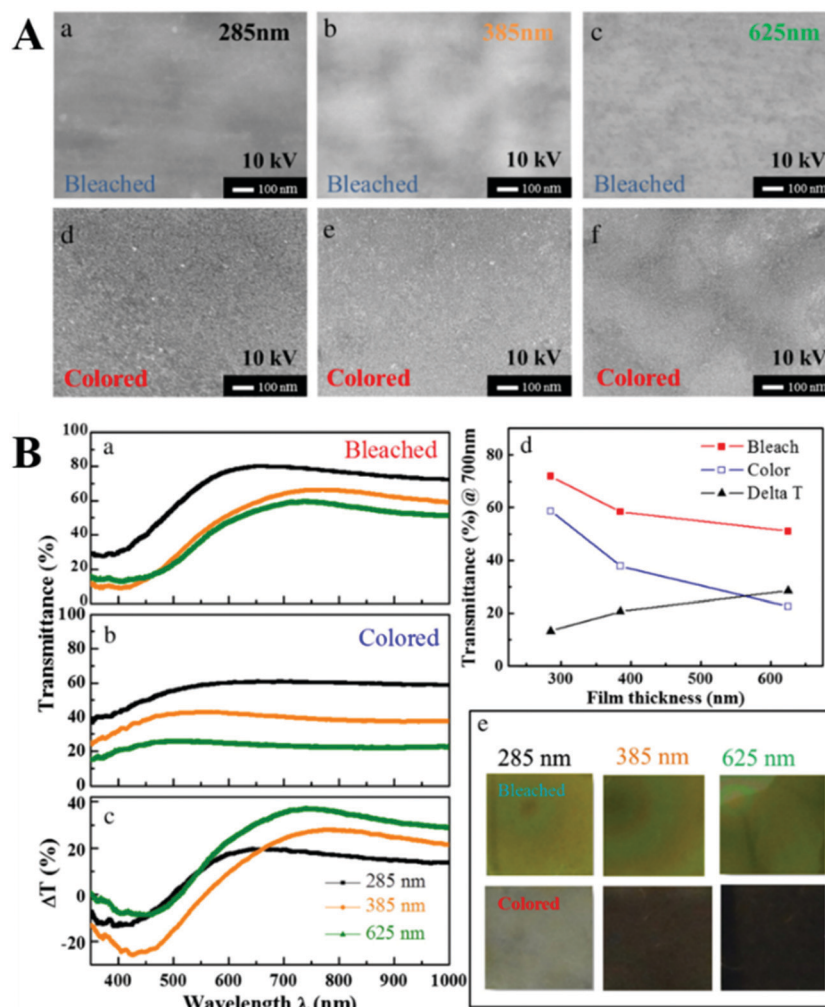
Fig. 29 Oxidized-reduced state of vanadium oxide films: (A) SEM images of films with different film thicknesses; (a and d) 285 nm, (b and e) 385 nm, and (c and f) 625 nm. (B) Optical spectra and images: (a and b) transmittance spectra of films for bleached-colored states, (c) transmittance changes (ΔT), (d) thickness dependence of transmittance, and (e) photographs of the film with different thicknesses for bleached-colored states, reproduced with permission (Copyright 2022, Elsevier[288]).

If the films are exposed for a long time (72 h), they become hydrogen-saturated and turn black due to amorphization and a transition to an irreversible phase of H_xVO_y.[290]

In view of applications, a darkened state of the film is required; it can be achieved by just applying a thicker GC film with the same material. Hence, a new material need not be designed, and the intrinsic properties of the film need not be modified. Thickness-dependent studies were conducted on V_2O_5 films of 285, 385, and 625 nm synthesized by a sol–gel process that exhibited excellent GC performance.[288]

Fig. 29 presents an SEM image, transmittance spectroscopy, transmittance change ΔT, transmittance at $\lambda = 700$ nm, transmittance change at $\lambda = 700$ nm, and photographs of the color change in the film in the bleached-colored states. The film surface became rougher than in the bleached state after exposure to hydrogen gas, as shown in Fig. 29A(a–f). The transmittance in both states and the percentage of transmittance modulation between the colored and bleached states

demonstrate the effects of film thickness on optical coloration. Although a thinner film exhibited higher transmittance than the thicker film, the latter led to a higher ΔT value at $\lambda > 650$ nm (Fig. 29B(a–c)). Indeed, ΔT of the 625 nm film was the highest, $\Delta T = 40\%$ at $\lambda = 740$ nm. As estimated at $\lambda = 700$ nm in Fig. 29B(d), the transmittance decreased with increasing thickness, whereas the transmittance modulation increased with thickness. The film color changed from yellow to gray for the 285 nm film and to black for the 385 nm and 625 nm films (Fig. 29B(e)).

Doping and hybridization are the most widely used strategies to improve the physical and chemical properties compared to their bare counterpart. Mo-doped V_2O_5, $(MoO_3)_{1-x}(V_2O_5)_x$ composites and $(WO_3)_{1-x}(V_2O_5)_x$ composites were investigated to improve the GC performance and time response.[4,301,302] Chang *et al.*[301] reported the coloration performance and response time of the composite oxide films of $(MoO_3)_{1-x}(V_2O_5)_x$ with $x = 0.00, 0.01, 0.03,$ and 0.05. The GC efficiency of the
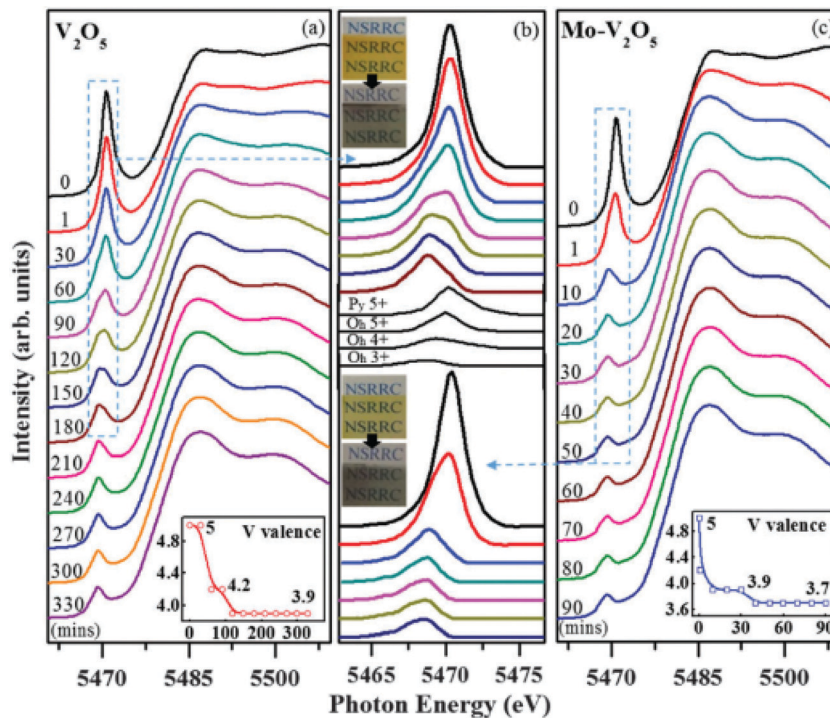
Fig. 30 *In situ* V K-edge XAS spectra of the colored state: (a) pure V_2O_5 film, (b) pre-edge regions of V_2O_5, Mo-V_2O_5, and different vanadium oxides, and (c) Mo-V_2O_5 films. Insets (a) and (c) show the time dependence reaction of the valence, reproduced with permission (Copyright 2022, Royal Society of Chemistry[4]).

MoO_3 film was improved by V_2O_5 doping. The $(MoO_3)_{0.99}$-$(V_2O_5)_{0.01}$ sample exhibited the shortest response time and highest change in transmittance. The modified MoO_3 film using a V_2O_5 over layer showed a stronger H_2 response than single MoO_3.[303] Ranjbar *et al.*[302] reported the gasochromism of $(WO_3)_{1-x}(V_2O_5)_x$ with x = 0.00, 0.09, 0.17, 0.23, 0.29, and 0.33. The E_{opt} decreased from 3.55 to 2.50 eV with increasing vanadium oxide concentration in WO_3.

The pure and Mo-doped V_2O_5 films fabricated using the sol–gel spin coating method exhibited excellent GC coloration. In-situ XAS was performed to determine the GC mechanism in terms of local atomic and electronic structures. The film color changed from light yellow to dark brown (inset, Fig. 30b).[4] A mixture of pyramid- and octahedral-like structures was found in Mo-doped V_2O_5, while the significant pyramid-like structure was identified in pure V_2O_5. The presence of more O_h (V^{5+}) in the Mo-doped V_2O_5 led to a four-fold faster response to H_2 than that of the pure V_2O_5 film.

The *in-situ* XAS spectra (Fig. 30a and c) showed that the same peak shifted to a lower energy and the intensity of the pre-edge peak decreased after the reaction time. However, the reaction time was 90 min for Mo-V_2O_5 and 330 min for pure V_2O_5, suggesting the importance of symmetric apical V–O bond in the GC effect. The more symmetric apical V–O bond leading to the faster coloration rate was demonstrated through the in-situ XAS study. Consequently, the Mo-V_2O_5 film exhibited faster GC coloration than the pristine V_2O_5 film (GC performance of ΔT = 20.3% compared with ΔT = 16.9% at λ = 750 nm, respectively)

being strongly correlated with the local atomic structure of the film.

GC windows are an alternative to other chromogenic windows for energy conservation but are also promising for use as a hydrogen sensor. The safe handling of hydrogen gas is of great importance for hydrogen energy technology because the amount of hydrogen tends to increase at a low concentration of approximately 4% in the atmosphere, which is a major issue in the future hydrogen economy. The hydrogen sensor based on the GC material requires no external electrical energy and consumes low power. When the GC windows are exposed to hydrogen, the change in optical transmission can be monitored and used as a hydrogen detector. Therefore, it is safer than other sensor technologies based on electrical measurements, which may give rise to an explosion. The advantages and disadvantages of GC applications need to be considered.

The construction of GCD is inexpensive and straightforward because only a single thin film is sufficient and can be coated easily on any glass substrate and even on flexible plastic substrates. Unlike ECDs, a transparent electrically conducting layer is not required in GCDs. On the other hand, water is critical for the GC film to transport hydrogen rapidly. Water should not escape from the GC film during the operation, particularly at higher temperatures. An integrated system that includes the gas supply system (pressurized bottle or electrolyzer), gas pump, and power supply is required for large-scale applications, indicating that additional external energy is indispensable. Another potential application of the GC effect is GC

mirrors based on metal hydrides that turn the colored state into a transparent state by taking up hydrogen.[304–306]

5.4. Photochromic process in V_2O_5

5.4.1 Fundamentals of photochromic V_2O_5. PC materials exhibit irreversible/reversible color changes or photo-induced coloration when exposed to a light source. Owing to the heat absorption and photocatalysis ability of V_2O_5, the PC mechanism can be operated following three cases (1) without excess temperature, (2) with excess temperature, and (3) photo-inserted hydrogen.

Electron–hole pairs can be separated, as shown in eqn (30),[50,307] to contribute to the PC phenomenon following two mechanisms with and without hydrogen-containing molecules.

$$V_2O_5 \xrightarrow{h\nu} V_2O_5^* + e^- + h^+ \qquad (30)$$
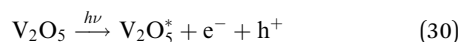
For the sample without hydrogen-containing molecules, the separated electrons move throughout the entire crystal and fill the split-off CB leading to an E_f shift. Owing to the separated state, electrons will relax to lower energy states and generate phonon energy because of collisions and scattering. Therefore, the contribution of this effect to photochromism is small compared to the photo-injection of hydrogen.[308]

Nishio *et al.*[309] reported the visible-light photochromism without a significant decrease in the effect. The coloration to blue-black may be caused by the reduction of V^{5+} to a lower valence, such as V^{4+} and V^{3+}. Two cases with and without heat treatment were investigated to discriminate the photochromism only and simultaneously occurring thermochromism–photochromism in V_2O_5.[309] Fig. 31 presents a model for light-induced thermochromism and bleaching of V_2O_5. Although irradiation heated the sample to above 400 °C, the color did not change after removing the irradiation as the sample cooled down rapidly to RT (route $1 \rightarrow 3 \rightarrow 4$, Fig. 31A). When the sample was reheated to 400 °C, its color state was maintained as it was cooled rapidly to RT (route $4 \rightarrow 2 \rightarrow 5$, Fig. 31A). Two different thermal treatments were also investigated. In the first method, the sample was heated to 400 °C and held at this temperature during irradiation for 60 min. In the end, irradiation was stopped, and the sample was cooled rapidly to RT. The color state for this method followed the route, $1 \rightarrow 4 \rightarrow 5$ (Fig. 31B). In the second method, the sample was held at RT during irradiation for 60 min, heated rapidly to 400 °C, and held at that temperature for 30 s before cooling to RT. The color state of the sample for this method followed the route $1 \rightarrow 3 \rightarrow 2 \rightarrow 6$, as shown in Fig. 31B.

The temperature increase (Δt), when exposed to laser intensity (I_0), is expressed using eqn (31).[310]

$$(\alpha\tau)^{1/2} \cdot \rho \cdot C_\nu t \cdot I_0 \cdot \tau \qquad (31)$$

where α, τ, ρ, and C_ν are the thermal diffusivity, pulse duration, mass density, and specific heat, respectively. If parameter values are $\alpha = 6 \times 10^{-6}$ m^2 s^{-1}, $\rho = 3.36$ g cm^{-3}, $C_v = 0.71$ J (g K)$^{-1}$, $\tau = 36$ ns, and $I_0 = 3.88 \times 10^6$ W cm^{-2}, Δt reaches 1222 K ($\sim$949 °C). Therefore, the actual temperature at the surface can be more than 976 °C, which is higher than the melting point of V_2O_5 ($\sim$690 °C).[310]

Fig. 32 shows the change in surface morphology of a thin film and pellet V_2O_5 after pulsed laser irradiation.[310,311] After 10 pulses of irradiation, the rod-like structure at the film surface transformed to a porous structure (Fig. 32A and B).[311] The surface roughness of the bulk-type pellet made by pressing a commercial powder became smooth and less porous after a single pulse of laser illumination (Fig. 32C and D).[310] The crystal structures were disordered, which led to a sub-stoichiometric composition and formed new local traps because of oxygen deficiencies.[312] These vacancies form V^{4+}, V^{3+}, and a mixture phase (Wadsley or Magnéli phase). The increasing temperature also extended the crystal and expanded the split-off of V_2O_5. The increasing temperature led to a TC phenomenon, which will be presented in detail in the next section.

The PL intensity changes as a result of the enhanced oxygen vacancies caused by the photoreduction and sample heating during laser irradiation.[106,118,309] At shorter wavelengths, the PL intensity decreased initially and increased at longer wavelengths. The peak of the PL intensity at $\sim$690 nm decreased
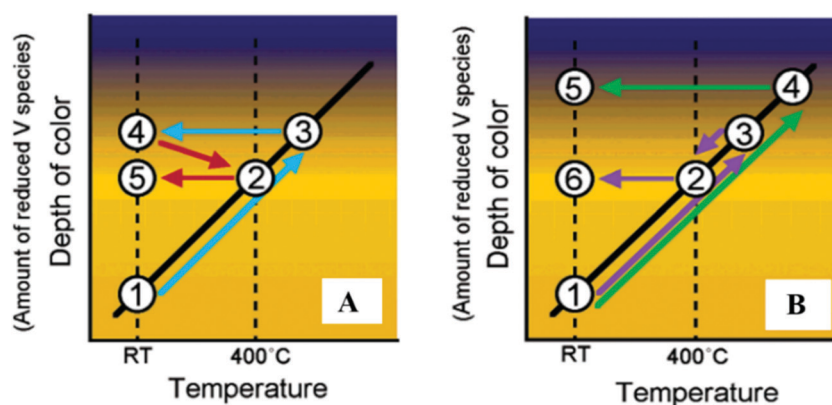
Fig. 31 Photochromism of models for light-induced thermochromism and bleaching process of V_2O_5. The background color of the figure represents the color of the sample, reproduced with permission (Copyright 2022, American Chemical Society[309]).
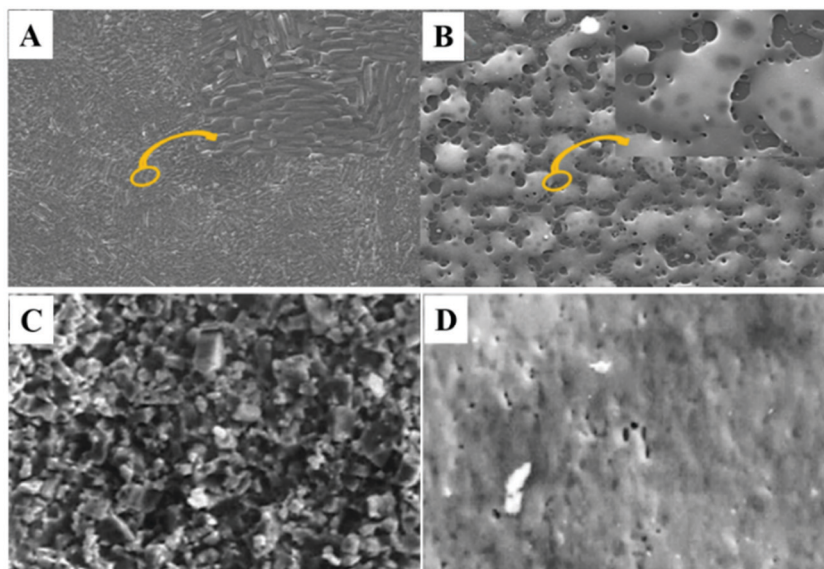
Fig. 32 SEM images of (A) and (B) the as-grown and colored V_2O_5 film after 10-pulse irradiation, (C) and (D) fresh and colored V_2O_5 pellets after one pulse irradiation. The figures are reproduced with permission (Copyright 2022, Elsevier[311] and IOPscience[310]).

slightly and became static after an initial exposure for 45 min, whereas a PL peak appeared at ∼450 nm with enhanced intensity.[118] The broad peak at 540–840 nm was quenched because of the increased temperature and photochromism when the film was irradiated for 60 min.[309] Two more peaks appeared at 408 and 448 nm after 10 pulses of irradiation, and the band edge of the V_2O_5 film increased.[106,313]

Due to the absorption of water (H_2O) or origins of polymers (CH_3OH, C_3H_5OH, and $(CH_3)_2NCHO$), the enhanced oxygen vacancies in sample were caused by decomposed H_2O or –OH led to the formation of a new oxidation state.[106,118,314] On the other hand, the oxygen molecules (O_2) of H_2O or –OH on the V_2O_5 surface are difficult to reduce with the electrons in the CB and mid-gap state because the negative potential of the redox potential of H^+/H_2 (4.5 eV, vacuum level) is at a higher level of the CB of V_2O_5 (5.0–5.2 eV, vacuum level).[37,315–317] On the other hand, the holes react easily with H_2O or the original polymers

on the V_2O_5 surface to form hydrogen ions. These electrons and hydrogen ions interact and react with V_2O_5 to form $H_xV_2O_5$, which are called hydrogen metal bronzes, as shown in eqn (20). Eqn (32)–(34) present the reaction of H_2O and CH_3OH with holes.[307,314]

$$h^+ + H_2O \rightarrow H^+ + {}^-OH \tag{32}$$

$$h^+ + CH_3OH \rightarrow H^+ + CH_2OH \tag{33}$$

$$h^+ + CH_2OH \rightarrow H^+ + CH_2O \tag{34}$$
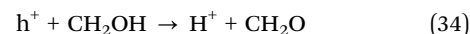
Gavrilyuk[308] presented the detailed mechanism of photo-injection of hydrogen from DMFA on TMOs. The V_2O_5 films were fabricated directly in an ambient condition containing DMFA ($(CH_3)_2NCHO$). These molecules were adsorbed on the V_2O_5 surface at O(1) because it has only one strong bond (Fig. 33A) and form of a donor–acceptor due to the overlap of
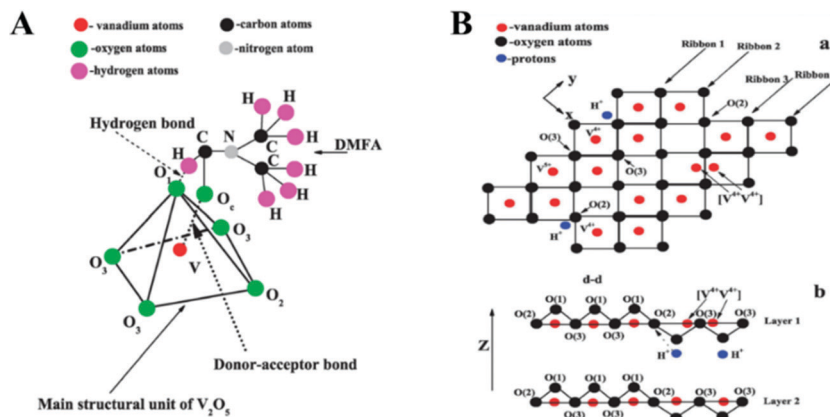
Fig. 33 Schematic diagram of (A) DMFA adsorption, donor–acceptor formation, and hydrogen bonds of DMFA–V_2O_5. (B) Possible position for the inserted hydrogen inside V_2O_5 crystalline reproduced with permission (Copyright 2022, Royal Society of Chemistry[318]).

the vacant d orbitals on the surface of the cation and the p orbital of O(2) with a lone electron pair.[318] The donor–acceptor (DA) bond (between the oxide and the molecules) and the bond of a proton (between H_2 and O(1) of V_2O_5) were generated. Fig. 33B shows a schematic diagram of the structure formation, including a sheet layer and cross-sectional layer (z-direction).

The transmission spectra for the $\nu(C=O)$ stretching vibration in the vapor, liquid, and adsorbed DMFA in the FTIR spectra results confirmed the formation of the DA bond.[308] The association in liquid led to a shift from 1725 cm^{-1} to 1675 cm^{-1}. This peak shifted continuously to smaller wavenumbers 1650 cm^{-1} when DA bonding was achieved due to the nucleophilic attack of the adsorbed molecules. Similarly, the peak of $\nu(C=O)$ also shifted from 1650 cm^{-1} of adsorbed DMFA in liquid to 1625 cm^{-1} of adsorbed DMFA containing deuterium. Hydrogen insertion can diminish the π overlap, which led to an elimination of the π state (valence band) and $\pi^\star$ state (conduction band) and a change in the E_{opt} of V_2O_5.

The N concentration (cm^{-3}) of the center inserted into thin film plays an essential role in the CE. The f concentration can be estimated using Smakula's equation (eqn (35)).[319]

$$N \times f = 0.87 \times 10^{17} \frac{n}{(n^2+2)^2} \alpha_{max} W \qquad (35)$$

where f, n, α_{max}, and W are the oscillator strength, refractive index, absorption coefficient in the band maximum, and half-bandwidth (eV), respectively. If the reflection losses are neglected, $\alpha_{max} \approx 2.31 \frac{D_{max}}{d}$, where d is the film thickness. This leads to the effect of the layer thickness on the PC sensitivity (ΔD_{max}).

5.4.2 V_2O_5 photochromic thin films and devices. Despite early studies, there are relatively few reports on V_2O_5 photochromism. The application of PC V_2O_5 in smart windows has been limited because of the small changes in OD, poor reversibility (reversibility is not complete), and a slow response time.[18] TMOs (except V_2O_5) have a narrow response in the ultraviolet (UV) region (< 400 nm) because it comprises only a few percent of the incident solar energy spectrum sunlight, while visible light (400–700 nm) occupies approximately 50% and NIR-IR (>700 nm) near 50%.[3,320]

V_2O_5 has a wide response in the spectrum from UV to visible light, such as thermal bleaching, multi-coloration, and high fatigability, which leads to a more interesting study. Table 6 lists the performance, including the switching time, OD, ΔT, and CE of GC, PC, and TC. The photo-coloration contrast and optical switching of the PC material were affected by the exposed light intensity, wavelength of the source, and irradiation time.[2] Photochromism in amorphous TMO films, including WO_3, MoO_3, and V_2O_5, prepared by vacuum evaporation, has been studied.[11,225,308] The film color developed gradually and was tinged with a blue color after irradiation for several hours.[225]

Commercial V_2O_5 powder exhibits PC behavior under laser irradiation.[309,310] The pink-yellow color of the V_2O_5 pellet (disk) turned immediately to a deep blue-black (Fig. 34A).[310] The

reversed color was obtained by annealing the colored sample at 400 °C. UV-visible diffusion reflectance of the colored sample is slightly higher in the UV region (< 460 nm) and much lower in the longer wavelength region (>460 nm) than that of the uncolored sample.

Fig. 34B shows the fresh and colored films after 10 pulses of irradiation of V_2O_5 films prepared by RF sputtering.[311] The color transformed from bright green (the as-grown film) to a deep dark blue. The transmittance of the colored film was much lower in the visible and NIR region than that of the uncolored film. The variation of the ΔT was approximately 46% at 560 nm and 14% at 900 nm, leading to broad absorption features without the abrupt absorption of a colored film. The V_2O_5 film fabricated by E_B shows that E_{opt} increased from 2.29–2.34 eV after UV irradiation for 30 min.[313]

Gavrilyuk's research group developed V_2O_5 photochromism.[308,314,318,319,321] Different synthesis methods, such as sol–gel, evaporation, and melting, were carried out to fabricate V_2O_5 films. Different organic molecules, such as CH_3OH, C_3H_5OH, and $(CH_3)_2NCHO$, as well as H_2O, were used on hydrogen photo-injection to investigate the CE. These studies confirmed that the PC sensitivity of V_2O_5 was influenced by the organic adsorbate, temperature, and film thickness, as shown in Fig. 35.[318,319,321]

Fig. 35A compares the PC sensitivities of different thinner V_2O_5 films illuminated for 120 min.[319] The generated electron–proton plasma diffused deeply into the film. This process was also affected by the porosity, thickness, and size of film particles and depended on the smallest particles. On the other hand, the plasma diffusion process reduced the concentration of injected centers, which lowered E_f. Consequently, a thicker film achieved a higher PC sensitivity than a thinner film. For the shift region, the optical shift showed a difference between the low energy (L-E) and high energy (H-E) of the absorption edge.

Fig. 35B presents the optical shifts of the sample at RT and 25 K.[318] The optical spectra shape was similar at L-E (<2.5 eV) and showed a blue shift at higher energy (>2.5 eV). For illumination at RT, the maximum shift reached 0.87 eV in the L-E and 0.77 eV in the H-E while the shift reached 0.78 eV in the L-E and 0.7 eV in the H-E, when illumination at 25 K. In particular, the OD showed an additional shift of 0.2 eV in the L-E and 0.5 eV in the H-E during the return to RT, whereas the intensity of the absorption band below 2.5 eV remained unchanged. The temperature affected the photoreaction to form a $V–O_1 \cdots H^+$ bond. The radicals formed at 25 K after the photo-detachment of H_2 through various stages and were more stable than at RT. This led to an enhanced optical shift reaching 0.9 eV in the L-E and 1.28 eV in the H-E.

Recently, PC properties of the Ag-doped V_2O_5, V_2O_5-based composites, and CTA/V_2O_5 NP bionanocomposites were investigated.[307,322,323] Both undoped and Ag-doped V_2O_5 films were colored by UV light irradiation and bleached with visible light irradiation and electrochemical processes. Un-doped films turned brown when exposed to UV light for 5 h and returned to dark yellow when bleached by visible light

Table 6 Gaso-, photo-, thermo-chromism of V_2O_5

Sample	Method	Chromogenic types	Test conditions	Evaluated wavelength (nm)	Coloration time (min)	Bleaching time (min)	Optical transmittance (reflectance) ΔT (ΔR) (%)	Optical band change ΔE_{opt} (eV)	Ref.
V_2O_5 film	The film was grown using the TE method	GC	Ethanol	—	—	100	5	—	287
			Methanol		—	100	4	—	
			Acetone		—	100	—	—	
			Isopropanol		—	100	—	—	
V_2O_5 film	The film was deposited on a glass substrate by sol–gel spin-coating	GC	Hydrogen	740	—	—	39	—	295
V_2O_5 film	The film was grown on a glass substrate by the TE method	GC	Hydrogen	545	—	—	12	—	298
0% O_2–V_2O_5 film	The films were grown on a glass substrate by a sputtering method				—	—	6	—	
5% O_2–V_2O_5 film					—	—	8	—	
V_2O_5 film: 285 nm	The film was deposited on a glass substrate by sol–gel spin-coating	GC	Hydrogen	700	—	—	13	—	288
V_2O_5 film: 385 nm					—	—	20	—	
V_2O_5 film: 625 nm					—	—	28	—	
V_2O_5 film	The film was deposited on an ITO substrate by sol–gel spin-coating	GC	Hydrogen	550	—	—	13.9	—	299
				800	—	—	16.9	—	
Pure V_2O_5	A Mo-modified V_2O_5 film was deposited on a silicon nitride membrane substrate by sol–gel spin-coating	GC	Hydrogen	750	100	—	16.9	—	4
Mg-V_2O_5					25	—	20.3	—	
$x = 0.00$	$(MoO_3)_{1-x}(V_2O_5)_x$ composite films were grown by the PLD method	GC	Hydrogen	450	12	18	31.8	—	301
$x = 0.01$					9	15	53.6	—	
$x = 0.03$					10	15	35.2	—	
$x = 0.05$					13.5	13	32.5	—	
$x = 0.00$				550	11	17	43.6	—	
$x = 0.01$					8.7	14	63.9	—	
$x = 0.03$					9.5	15	45.6	—	
$x = 0.05$					13	12.5	50.1	—	
$x = 0.00$				650	11	17	45.2	—	
$x = 0.01$					8.7	14	65.8	—	
$x = 0.03$					9.5	15	50.5	—	
$x = 0.05$					13	12.5	54.7		
V_2O_5 particles	A V_2O_5-based composite film was prepared by the sol–gel method	PC	UV irradiation	700	10	—	11	0.05	307
					60	2880	16	0.09	
V_2O_5 film	The film was deposited on an Al_2O_3 substrate by the RF sputtering method	PC	Laser irradiation	560	10 pulses	—	49	—	311
V_2O_5 pellet	V_2O_5 pellets were prepared at a pressure of 8 MPa from commercial powders	PC	Laser irradiation	600	—	—	6.0	—	310
V_2O_5	The film was deposited on a quartz substrate by the RF sputtering method	TC	RT–80 °C	2000	—	—	2.5	—	351
Film: 9, RT, -	The film was deposited on a quartz substrate by the DC magnetron method with different oxygen pressures, substrate temperatures, and annealing temperatures	TC	RT–200 °C	2500	—	—	30	—	110
Film: 15, 400, —					—	—	3.5	—	
Film: 20, RT, —					—	—	17	—	
Film: 9, RT, 400					—	—	11.5	—	
Film: 20, RT, 400					—	—	15	—	
Film: 20, RT, 200					—	—	39	—	
0% Mo-V_2O_5	Mo-doped V_2O_5 films were deposited on a glass substrate by the SP method	TC	250–400 °C	2500–3300	—	—	13	—	330
10% Mo-V_2O_5			25–50 °C		—	—	15	—	
20% Mo-V_2O_5			25–50 °C		—	—	18	—	
V_2O_5	Pure and Cr-doped V_2O_5 films were deposited on a silicon substrate by the MOCVD method	TC	40–220 °C	550	—	—	19	0.17	120
V_2O_5 300 nm			50–200 °C		—	—	3	—	
V_2O_5 1.2 μm			50–200 °C		—	—	18	—	
V_2O_5 2.4 μm			50–200 °C		—	—	20	—	
4.34% Cr-V_2O_5			40–220 °C		—	—	3	—	
V_2O_5/glass	The film was deposited on glass and FTO substrates by the RF sputtering method	TC	250–500 °C	550	—	—	37	0.61	326
V_2O_5/FTO				1000	—	—	25	—	
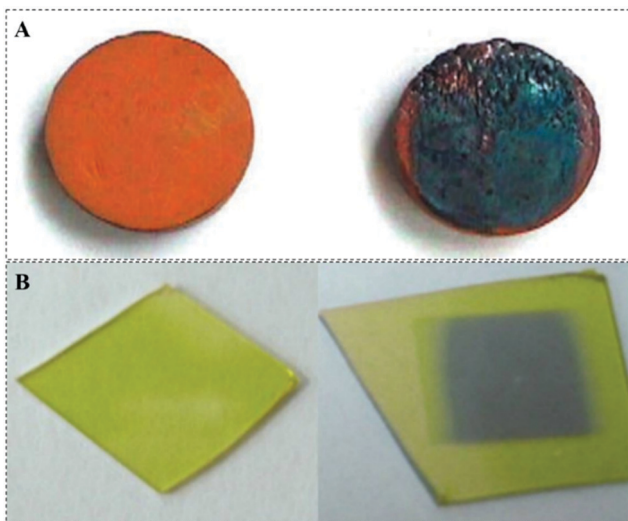
Fig. 34 Photographs of (A) fresh and colored V_2O_5 pellets and (B) the as-grown and colored V_2O_5 films. The figures are reproduced with permission (Copyright 2022, IOPscience[310] and Elsevier[311]).

irradiation for 4.5 h or recharged at +1.0 V for 60 s. For Ag-doped V_2O_5, the film rapidly became brown after only 4 min exposure to UV light. The bleaching sample required 6 h of visible irradiation or 20 s discharging at +1.0 V. The absorption spectra showed that the response of Ag-doped V_2O_5 is faster than that of the pure V_2O_5 film because of the contribution of absorption of UV light of Ag NPs.[322]

Miyazaki *et al.*[307] observed the natural reversible PC properties of V_2O_5-based composites at RT. For coloration, the transmittance spectra showed an absorption shift and a decrease in the IR and NIR regions (Fig. 36). The E_{opt} increased slightly from 2.52 eV to 2.61 eV, and the film color changed from yellow to green to pale blue after irradiation for 1 h. Natural bleaching showed that the film almost returned to the initial color after 48 h in the dark.

5.5. Thermochromic process in V_2O_5

5.5.1 Fundamentals of thermochromic V_2O_5.

The dynamics of the optical properties as a result of thermal stimulation was observed for various vanadium oxide phases, among which VO_2 has attracted increasing attention owing to its MIT at near RT (340 K). Lower MIT temperatures were reported for VO (126 K), V_6O_{13} (150 K), and the Magnéli phases, such as V_2O_3 (165 K), V_4O_7 (250 K), V_5O_9 (135 K), V_6O_{11} (177 K), and V_8O_{15} (70 K).[324]

Recently, some studies provided evidence of the SMT[325,326] or MIT[107,327] in V_2O_5. These reports reveal metallic behaviors at high temperatures. The transition temperature in V_2O_5 is one exception, while the experimental results converge towards a loss of lattice oxygen (vanadyl group) without a structural change. This section discusses some of the reports related to the TC phenomena of V_2O_5 materials.

Kang *et al.*[107] have reported temperature-dependent spectroscopic ellipsometry measurements of V_2O_5 films. An abrupt change in the extinction coefficient was observed at 265 to
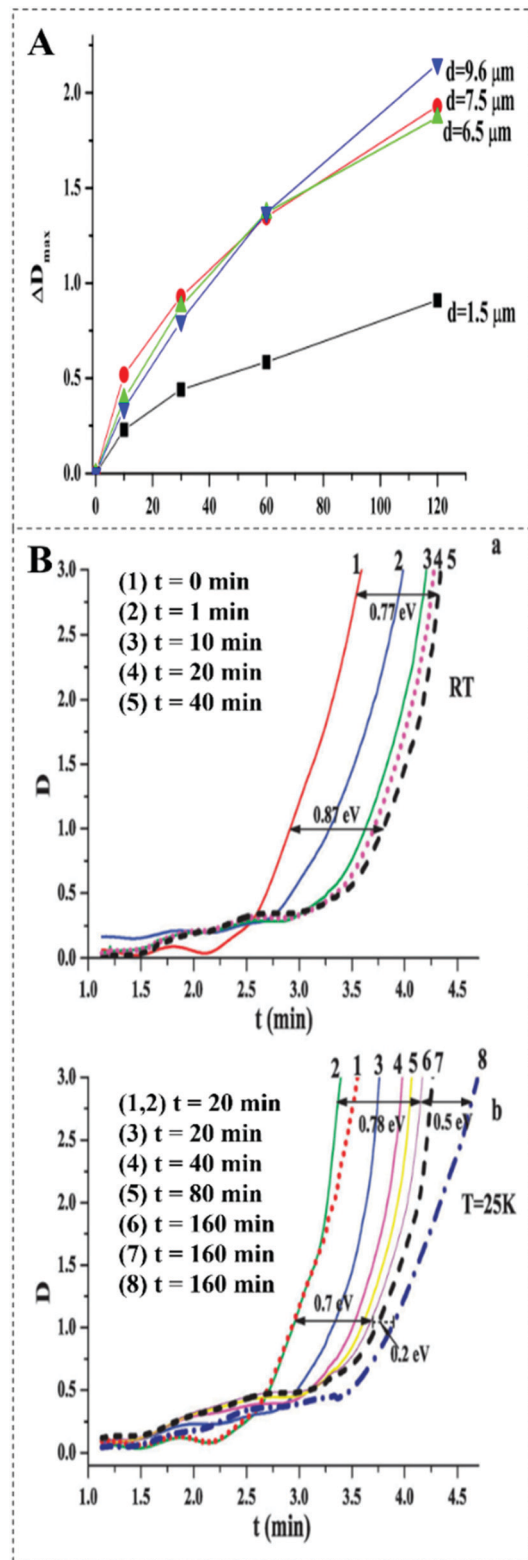
Fig. 35 Optical density spectra of the V_2O_5 film. (A) ΔD_{max} of different film thicknesses, (B) before and after the illumination time (*t*); before and after the illumination time (*t*) at 25 K ((7) illumination and heating up to *RT*, (8) illumination, heating up to RT, and maintain for 2 h). The figures are reproduced with permission (Copyright 2022, Elsevier[319] and Royal Society of Chemistry[318]).
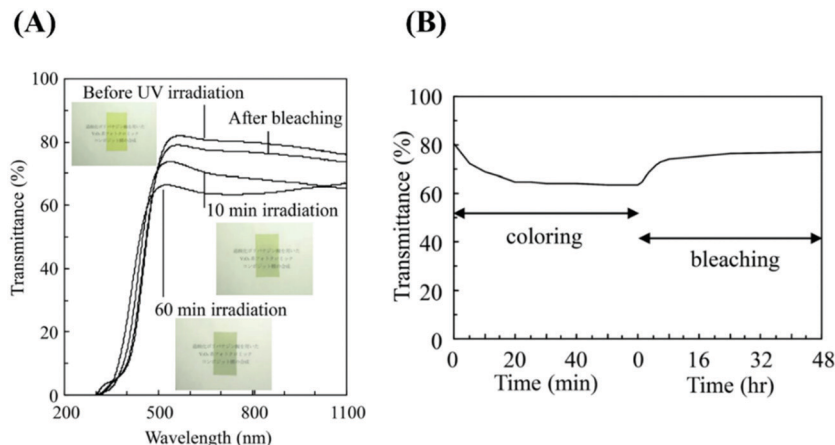
Fig. 36 Optical spectra change on the coloring and bleaching of composite films before and after UV-Vis irradiation: (A) Transmittance spectra and (B) the time dependence of transmittance change, reproduced with permission (Copyright 2022, Royal Society of Chemistry[307]).

325 °C, and a Drude absorption feature indicating the presence of a metallic phase was observed above 310 °C. Blum *et al.*[327] reported a reversible MIT of a $V_2O_5(001)$ single crystal at 77–127 °C. Scanning tunneling microscopy revealed the nucleation and growth of vanadyl (V=O) oxygen vacancies with temperature, which was consolidated by density functional theory (DFT) and Monte Carlo calculations. This reversible phenomenon occurred exclusively at the surface at 77–127 °C and became irreversible at higher temperatures by forming V_6O_{13} and V_2O_3. These results were discussed by Pergement *et al.*[328] and Aita,[329] who questioned the pertinence of describing this phenomenon as an MIT.

Pergement[328] suggested that heating V_2O_5 in this and other similar references induces a reduction and the formation of phases that are metallic at these temperatures. Aita[329] suggested that the XRD peak shift with a trend change at 200 °C indicates a structural transition from α-V_2O_5 to γ'-V_2O_5, a metastable polymorph. The monitoring of the lattice parameters, a, b, and c, of α-V_2O_5 as a function of temperature revealed a linear increase in "c" with temperature, while "a" and "b" remain unchanged.[120] The linear trend of "c" from 20 to 300 °C did not confirm the hypothesis of the α-V_2O_5 to γ'-V_2O_5 transition.

The distorted octahedra inside the V_2O_5 crystal affect the indirect vanadium–vanadium interactions with the intermediate vanadyl group. A shift in the (001) XRD peak,[107,120] a change in peak intensity, and a shift in the Raman spectrum were observed.

Fig. 37A(a) presents the reversible temperature-dependent Raman shifts.[223] In most of the peaks, the intensity decreased with sample heating and returned to the original level when the sample was cooled to RT (Fig. 37A(b)). In particular, the modes at 483 and 850 cm^{-1} vanish above 257 °C and re-emerge after cooling to RT. The peak at 483 cm^{-1} was ascribed to V–O(2)–V bending deformation along the z-direction, whereas the peak at 850 cm^{-1} was attributed to the antiphase stretching mode of V–O(2) bonds. The Raman shift of approximately 7 to 13 cm^{-1} was

observed over the temperature range of 77–377 °C (Fig. 37A(c)). The intensity ratio of the peak at 144 cm^{-1} (corresponding to the vibration O(x)–V–O(x)) and 993 cm^{-1} (corresponding V=O(1) stretching mode) increased rapidly above 177 °C (Fig. 37A(b)). This trend was attributed to the possible loss of O(1) atoms from the structure of V_2O_5.

Fig. 37B(a) shows the temperature-dependent XRD patterns over the 25–300 °C range.[120] The (001) peak showed a shift towards a lower XRD angle while the (200) peak remained unaffected (Fig. 37B(b)). Fig. 37B(c and d) show the reversible shift without any hysteresis effect, and they demonstrate a symmetric-like point at 160 °C. The obtained results agree with the increase in the distance between the "ab" layers of V_2O_5 with increasing temperature.

The relaxed structure, lattice expansion, phase transition, and oxygen vacancy in local structure might cause the appearance of mid-gap state and new split-off bands, and cause downward shifts of old split-off bands. Regarding E_{opt}, a decrease in E_{opt} with increasing temperature was reported: from 2.33 to 1.72 eV (RT–500 °C),[326] from 2.14 to 2.07 eV (27–377 °C),[223] and from 2.13 to 1.96 eV (40–220 °C).[120] The PL position peak also shifted and extended to a broad peak with increasing temperature.[325] Moreover, the measured temperature dependence of the photon energy showed that these parameters are reduced over the range of 280–295 °C. At higher temperatures (310–325 °C), the photon energy decreased significantly because of the metallic behavior.[107] The electrical measurements also showed that the resistance decreased suddenly with increasing temperature in the 227–277 °C,[223] 280–480 °C,[107] and 277–377 °C ranges.[325] While disregarding the debate on the MIT/SMT behavior, the changes in the E_{opt} and PL with the temperature well below 300 °C support the presence of thermochromism in V_2O_5.

5.5.2 V_2O_5 thermochromic thin films and devices. Compared to the EC and GC devices, TC V_2O_5 devices have attracted less attention because they are difficult to control. Nevertheless, TCDs and PCDs are based on a single thin film, and they can be
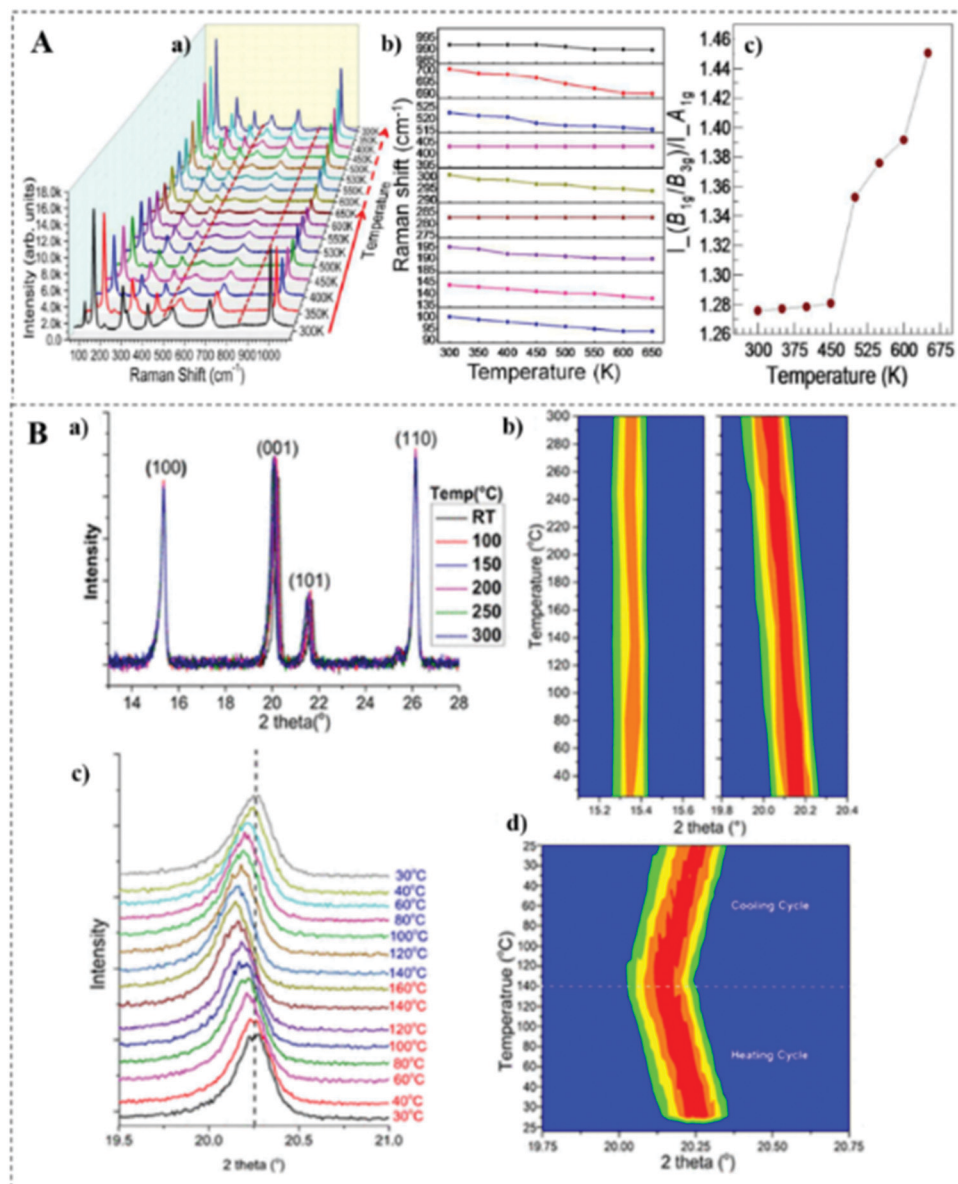
Fig. 37 Thermochromic properties of V_2O_5: (A) Temperature-dependent Raman spectra of V_2O_5 NRs: (a) increasing–decreasing temperature in the range 300–650 K, (b) altered vibrational frequencies, (c) intensity ratio of the peak at 144 cm^{-1} and 993 cm^{-1}. (B) XRD patterns of the V_2O_5 film at different temperatures (a) and contour plot of the peaks corresponding to (200) and (001) reflexes (b), (c and d) the reversibility of the thermochromism is monitored by measuring the shift of the reflex (001) in the heating and cooling stages. The figures are reproduced with permission (Copyright 2022, American Chemical Society[120,223]).

operated under direct sunlight without an additional control system. These are advantages for applications, such as pure smart windows on buildings or non-contact optical temperature sensors.

The change in the IR transmittance (region 2500–4000 cm^{-1}) due to TC of V_2O_5 was investigated. Cui *et al.*[110] compared optical transmittance in the IR region of the V_2O_5 film at RT and 200 °C. The films were deposited by sputtering at different substrate temperatures, annealing temperatures, and ratios of oxygen partial pressure. The transmittance variation reached 30% and 39% for the sample without annealing and the sample annealed at 400 °C, respectively.

Nazemiyan *et al.*[330] compared the TC properties of pure and Mo-doped V_2O_5. For the pure V_2O_5 film, the IR transmittance increased slightly with heating up to 250 °C and decreased sharply with heating up to 300–400 °C. The transparency of the TC film was observed clearly at 50 °C. In contrast, the transmittance decreased 1/6 orders of magnitude from 50 to 300 °C for the Mo-doped film because of the increase in carrier concentration. The SMT behavior exhibited that the resistance measurement also showed a decrease from $> 10^6 \ \Omega$ to $< 10^3 \ \Omega$ at 25 °C and above 300 °C, respectively.

Recently, evidence of visible TC behavior in V_2O_5 powder and coating was demonstrated.[120,331,332] This behavior
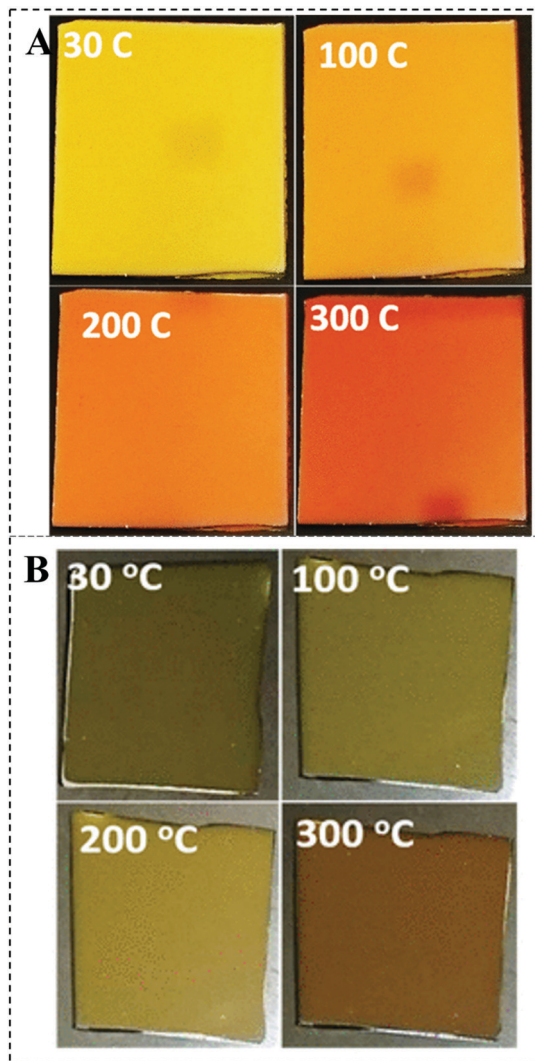
Fig. 38 Color modulation state (thermochromism), photographs of the film at different temperatures: (A) pure V_2O_5 film and (B) 4.34% Cr-doped V_2O_5 film, reproduced with permission (Copyright 2022, American Chemical Society[120]).

demonstrates the opposite orange to deep orange transition due to a temperature increase. The color transition from green to red in the mixed V_2O_5 and Cr_2O_3 powder was attributed to the TC behavior.[331] Kumar *et al.*[120,332] examined the visible thermochromism of V_2O_5 films grown by CVD on silicon, glass, and metal substrates. Fig. 38A shows the reversible TC for undoped V_2O_5 films on a silicon substrate. The color changed from bright yellow to deep orange with increasing temperature. The total hemispherical reflectance (THR) revealed a red shift with heating that was reversible with cooling. For the Cr-doped V_2O_5 thin film, the initial film at RT showed a different color compared to pure V_2O_5, with a dependence on the Cr doping concentration. For a doping concentration of 4.34%, the color changed from dark olive green to dark clay orange with increasing temperature from 30 to 300 °C (Fig. 38B). The THR revealed a slight shift, while the lattice parameter "c" increased by 0.045 Å.[120]

6. Conclusions and perspectives

6.1 Conclusions

This review presents the role of CDs in energy-saving applications. The crystalline and atomic structures of α-, β-, ε-, δ-, γ-, ζ-, and ω-phases of pure V_2O_5 and $M_xV_2O_5$ as well as their band structure were also discussed. The formation mechanism and synthesis methods to fabricate micro–nanostructured V_2O_5, including bottom-up (*i.e.*, physical vapor deposition, chemical vapor deposition, and solution method), top-down, and combined methods to control the morphologies of various zero dimension to three dimensions were presented. The wide ranges of E_{opt} due to the unique electronic structure of α-V_2O_{5-y} with three bands (main CB, split-off CB, and mid-gap state) were clarified. The multi-colors of the original V_2O_5 films (fixed chromism) due to the growth parameters, dopants, and composites were discussed.

Common parameters to evaluate the efficiency of V_2O_5 CDs, *i.e.*, the change in the optical bandgap, the optical transmittance, switching time, optical density, coloration efficiency, cycling stability, durability, and operational environment, are presented. The fundamental characteristics of chromogenic V_2O_5, including the electro-, gaso-, photo-, and thermochromism related with the advancements through decades, working mechanism, recent progress, and applications are summarized. In addition, the synthesis methods, structures (crystalline and electric band structures), and optical properties, which play an essential role in improving the CE, are outlined.

The micro–nano structure increases the surface area and limits the diffusion distance to improve the switching response time of ECDs and GCDs of V_2O_5. Element-doped V_2O_5 and materials@V_2O_5 composites increase the electronic conduction for enhancing the chromic performance of V_2O_5 devices. The ECDs using M-doped V_2O_5 exhibited long-term cycling stability and a high CE (M = Ti), rapid switching speed (M = Ag and Fe), and high visible transmittance (M = W and Mg). Similarly, M-doped V_2O_5 also demonstrates a faster response time on GCDs (M = Mo) and PCDs (M = Ag) while presenting new colors on TCDs (M = Cr). CDs show an improved switching time and enhanced durability because they prevent vanadium ion dissolution in the electrolyte and contribute to the high conductivity materials, *i.e.*, GO, RGO, PEDOP, and Ag.

The colored–bleached state contrasts of some metal oxides, such as WO_3, NiO, TiO_2, and MoO_3, correspond to two states of bright and dark, which lead to non-aesthetic smart windows with a dull and black appearance. The colored state can reduce the temperature inside the room but decrease the light intensity in the visible region, while the bleached state can enhance glare, resulting in user discomfort. As discussed above, the color change to the V_2O_5 film caused by both an absorption shift and intensity variation of light transmission/reflection occurs simultaneously, a potential material for smart windows. This shows that both anodic and cathodic colorations cause multistates, corresponding to multicolor. The colored state shows enhanced transmittance in the shorter wavelength

region but reduced transmittance in the NIR and IR regions. Hence, it can reduce the temperature but still maintain visible light transmission. The bleached state decreases in the shorter wavelength region, mitigating glare and making the color comfortable.

Furthermore, some important opening research directions for prospects as a guide for the wider materials science community are provided. The following communities will have high potential interest in this review, including physicists interested in the fundamentals of the optoelectronic characteristics, chemists/electrochemists interested in the synthesis and application of V_2O_5, and materials scientists and nanotechnology integrators. The synergy between these communities will potentially trigger the development of V_2O_5 chromogenics to the level of other established materials.

6.2 Perspectives

GCDs, PCDs, and TCDs are based on simple integration with a single thin film deposited on different substrates. There is no need for transparent conducting electrodes and an electrolyte, which may lead to easy fabrication on a large scale and prolonged service life. However, PCDs and TCDs have received less attention because of their relatively low performance and slow response. V_2O_5 TCDs operate at high temperatures, while PCDs need high excitation source intensities (*e.g.*, laser source). PCDs and TCDs are also passive methods that make it challenging to control chromogenic parameters. Therefore, V_2O_5 PCDs and TCDs do not find practical applications on smart windows. The photo- and thermal-reaction processes on V_2O_5 are explained and the potential for other applications in the future is highlighted. ECDs and GCDs are the active methods to control parameters, such as ΔT, t_b, t_c, and ΔD. On the other hand, at higher temperatures, during operation, water can be deposited on the surface of GCDs, leading to a decrease in performance and service life. Among the chromogenic applications of V_2O_5, ECDs have many advantages for smart windows applications. Nevertheless, there is no detailed study on the cost and assessed feasibility to produce V_2O_5 for large-scale commercialization. ECD$_S$ have complicated structures, including multilayer, electrolyte, and applied electrical system that requires a complicated setup, repair, and maintenance that may lead to high cost.[5]

Reducing global warming, alleviating climate change, energy saving, and green technology have attracted worldwide attention. Smart windows are crucial for energy saving and are a key to green technology to protect the environment and help develop a global society-economy. In view of the practical applications, multicolor, high optical transmittance, high optical contrast ratio, rapid switching response time, high color efficiency, long-term cycling, durability, and large-scale production are desirable for chromogenic materials, but the achievements in these parameters are challenging. The current research shows that the use of a single "technique" cannot meet these requirements. Therefore, the combination of "multitechniques" as "multidisciplinary integration" is a solution to optimize the above parameters. As shown in Fig. 39, the possible combinations of different strategies based on V_2O_5 materials are given as follows:

Strategy 1: combination of different synthesis methods, including bottom-up and top-down methods based on two or more steps, can fabricate various morphologies on a large scale. Moreover, the morphologies can be controlled and remain stable. For example, pure, metal-doped, and materials@V_2O_5 composites with different sizes and morphologies can be prepared using a solution method. Systematic methods are needed to correlate the aspect ratio, size, and oxygen deficiency of particles with the optical properties, including the response kinetic to external stimuli and the stability. Different NP sizes of pure or V_2O_5-based composites also can be obtained *via* a solid-state reaction using the mechanical milling method. Different ratios of various pure powders were mixed and ball milled to form a composite powder, which was then dispersed in a solvent. These solutions can be sprayed, electro-spun, rolled, spin-coated, casted, screen-printed, or co-assembling using the Langmuir–Blodgett technique on different substrates. These techniques can be used to prepare the monolayer or multilayer V_2O_5 on a large scale. Subsequently, the film can be annealed at different temperatures or atmospheres to control the surface morphology.[21] Thus far, many breakthroughs have been achieved in the research and development of micro–nanostructured V_2O_5 by combining many fabrication methods. V_2O_5 NPR/NTL can meet the high surface area and stability, but direct self-organization of V_2O_5 nanopore is difficult owing to the instability of vanadium oxide during growth in a water-containing electrolyte.[125] This architecture can be achieved by intermediate film growth or using dielectric breakdown etching. For example, V metal or a V_2O_5 dense film can be deposited on a substrate and covered by another film, such as TiO_2 and Al_2O_3. Nanopore of the intermediate film was prepared by the ECAD method that plays a nuclei role to grow V_2O_5 NPR/NTL.

Strategy 2: combination of different morphologies of V_2O_5 micro–nanostructures, including 0D, 1D, and 2D, can produce the desired V_2O_5 micro–nanoarchitectures. The tailored micro–nanostructure and rational designs are the keys for improving the surface area and achieving a short ion diffusion length and ion transport.[40] Owing to the novel behaviors, micro–nanostructured V_2O_5 has become a potential candidate for energy saving and energy storage. In addition, the utilization of heterojunctions could significantly enhance the electron–hole pair separation and oxidation kinetics in water for improving PC performance.

Strategy 3: combination of V_2O_5 with other materials via doping, composite, and hybrid formation can improve the physical and chemical properties of the materials. Recent developments of various synthesis methods and their combinations open new avenues for integrating multifunctional materials.[2] For example, the coexistence of other phases of vanadium oxide (VO_x) can amplify the chromic phenomena. Searching for accurate rates and coloration mechanisms of vanadium oxides can produce new colors and reduce the TC transition temperature. The combination of doping and composite can control the bandgap, enhance the long-term
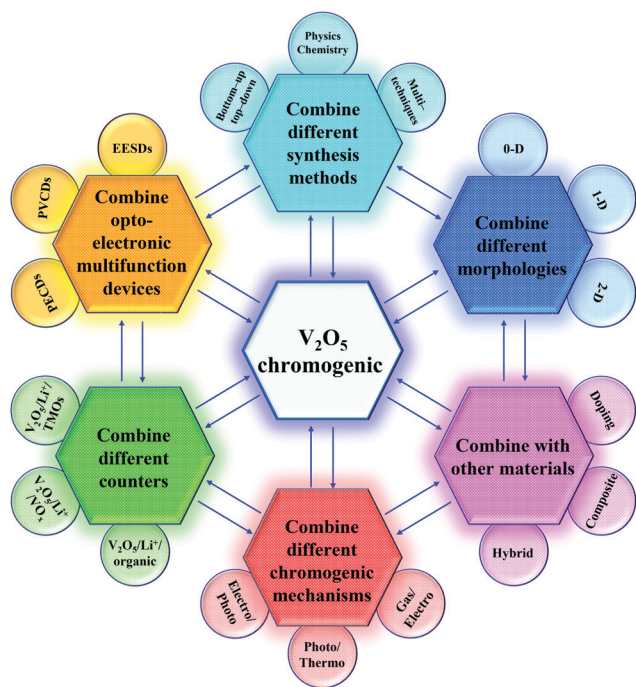
Fig. 39 Illustration of the prospects for improving V_2O_5 chromogenic devices.

durability, and improve conductivity. The cycling stability and electrochemical performance can be enhanced by integrating nanostructured V_2O_5 with a carbonaceous material and a conductive polymer.[32] Such development of new nanocomposites could potentially reduce the number of carbonaceous materials and conductive polymer under optimized electrochemical processes.

Although showing multicolor, the initial or bleaching state of the V_2O_5 fully stoichiometric phase exhibits an orange color. There is not enough light intensity in shading cases for smart windows. Therefore, the combination of V_2O_5 with other chromogenic materials, such as WO_3, MoO_3, and TiO_2, can meet the two standards, intensity and multicolor. The key challenges are to find a suitable mass ratio for EC performance and other chromogenic parameters. The influence of WO_3, MoO_3, and TiO_2 materials on the physical and chemical properties and the pathway ion at the interface between the materials also need examination. All the above open research trends in the future for chromogenic material@V_2O_5 composites.

Strategy 4: a combination of different chromogenic mechanisms, such as TC–PC, GC–EC, and PC–EC, can improve chromogenic performance. Based on the V_2O_5 TC and PC mechanisms discussed above, the color change phenomena in materials can occur due to the simultaneous optical and thermal absorption when exposed to light. Nevertheless, the influence of the V_2O_5 chromic types needs to be validated further.

Strategy 5: a combination of different chromogenic counters can produce a multicolor due to the overlay color with different counters. The regulated suitable color will result in a comfortable room that improves the quality of life with higher productivity. Most studies focused on a V_2O_5 single electrode but did not examine the influence of electrolyte type, another

electrode, and substrate to ECDs. Practical applications require V_2O_5 ECDs to meet the synchronous system (*i.e.*, two electrodes and the electrolyte).[333] As a result, the interface properties (*i.e.*, physical and chemical properties at the interface between the electrolyte and the EC layer, and between the EC layer and the substrate), as well as the mechanism of volume expansion, should be investigated thoroughly.

Strategy 6: combination of optoelectronic couple devices, such as EESDs (based on self-powered EC batteries mechanism), PECDs, and PVCDs (based on self-photo-recharge) to improve energy-saving performance. PECDs and PVCDs are the ideal perspectives of future buildings because of self-power and self-spectral tunability.[334] The combination of energy generation, energy storage, and chromogenics to become a three-in-one device will be the trend of future study and is receiving more attention that improves the energy-saving performance. Nevertheless, the challenge is determining how to combine them in the best possible way.

Despite considerable research efforts, challenges still remain, such as the long-term durability, possibility of large-scale production, reduced costs for commercialization, and installation complexity (ECDs and GCDs).[2,5] The multidisciplinary integration, including physics, chemistry, materials science, and nanomaterial technology, is a great solution. Many studies have focused on optimizing the coloration performance, but integrated application-oriented research is still lacking.[40] This leads to studies on V_2O_5 CDs to expand the use beyond the laboratory scale through commercialization. Therefore, the ingenious combination of two or more strategies (Fig. 39) based on multidisciplinary integration will be critical for parameter optimization to open opportunities to solve these problems but also are challenges. For example, a combination of materials can help choose the components accurately and control the concentration in materials@V_2O_5 composites precisely.

These challenges also need further fundamental and experimental investigations. This review also provided the keys to finding the appropriate solutions for developing V_2O_5 CDs and multifunctional devices (EESDs, PECDs, and PVCDs) in which V_2O_5 chromogenic mechanisms have similar phenomena. Furthermore, many studies on V_2O_5 applications were highlighted, such as photocatalysis, gas sensors, thermal sensors, electrochemical systems, battery systems, photoresponse, MIT, SMT, data display, optical signal processing, and optical switch.

This review presents the latest progress related to the advances of chromogenic V_2O_5, the fundamental aspects, and the applications related to energy saving. This review is an opening discussion because nanostructured V_2O_5-based research has challenges that remain to be overcome. Moreover, there is a huge space for nanostructured-V_2O_5 development, which requires more efforts in academia and industry toward new energy saving and storage applications in the future.

List of abbreviations:

(a) General

VO   Vanadium monoxide

VO$_2$	Vanadium dioxide
V$_2$O$_3$	Vanadium sesquioxide
V$_2$O$_5$	Vanadium pentoxide
WO$_3$	Tungsten oxide
MoO$_3$	Molybdenum trioxide
GO	Graphene oxide
RGO	Reduced graphene oxide
PEDOT	Poly(3,4-ethylenedioxythiophene)
PEDOP	Poly(3,4-ethylenedioxypyrrole)
DMFA	Dimethylformamide
CTA	Cellulose triacetate
PS	Polystyrene
TMOs	Transition metal oxides
ITO	Indium–tin oxide
FTO	Fluorine-doped tin oxide
PET	Polyethylene terephthalate
SMT	Semiconductor-metal transition
MIT	Metal-insulator transition
E_{opt}	Optical bandgap
E_g	Bandgap
E_c	Optical bandgap of colored state
E_b	Optical bandgap of bleached state
E_i	Optical bandgap of initial (pristine) film
$T_c(\lambda)$	Colored transmittance
$T_b(\lambda)$	Bleached transmittance
$T_i(\lambda)$	Initial transmittance
$R_c(\lambda)$	Colored reflectance
$R_b(\lambda)$	Bleached reflectance
$R_i(\lambda)$	Initial reflectance
VB	Valence band
CB	Conduction band
RT	Room temperature
vdW	van der Waals

(b) Morphology

0D, 1D, 2D, and 3D	
	Zero-, one-, two-, and three-dimension(s)
QDs	Quantum dots
NPs	Nanoparticles
NPRs	Nanoporous
NRs	Nanorods
NWs	Nanowires
NBs	Nanobelts
NFBs	Nanofibers
NFLs	Nanoflowers
NTs	Nanotubes
NTLs	Nanotubulars
NHs	Nanohollows
NSHs	Nanosheets
NSPs	Nanospheres
NRBs	Nanoribbons
DG	Double-gyroid

(c) Synthesis method

PVD	Physical vapor deposition
WCR	Wet chemical reaction

CBD	Chemical bath deposition
ECAD	Electrochemical anodization deposition
ESS	Electrostatic spray
ED	Electrodeposition
TP	Thermal pyrolysis
CSP	Chemical spray pyrolysis
ESP	Electrospun
CVD	Chemical vapor deposition
AP-CVD	Atmospheric-pressure CVD
LP-CVD	Low-pressure CVD
AL-CVD	Atomic layer CVD
MO-CVD	Metal–organic CVD
PE-CVD	Plasma-enhanced CVD
AA-CVD	Aerosol-assisted CVD
PLD	Pulsed laser deposition
ALD	Atomic layer deposition
PLA	Pulsed laser ablation
LASP	Laser-assisted surface processing
EBE	Electron beam evaporation
TE	thermal evaporation
RF-sputtering	Radio-frequency sputtering
DC-sputtering	Direct current sputtering
IB-sputtering	Ion beam sputtering
RFRP	Radio-frequency rotating plasma
TD	Thermal deposition
MQ	Melting quench
BM	Ball milling
DFT	Density-functional theory
OLCAO	Orthogonalized linear combination of atomic orbitals

(d) Measurement method

SEM	Scanning electron micrograph
TEM	Transmission electron microscope
STM	Scanning tunneling microscopy
XRD	X-Ray diffraction (XRD)
XPS	X-Ray photoelectron spectroscopy
XAS	X-ray absorption spectroscopy
EXAFS	Extended X-ray absorption fine structure
PL	Photoluminescence
CL	Cathodoluminescence
UV	Ultraviolet
IR	Infrared
NIR	Near infrared

Conflicts of interest

There are no conflicts to declare.

Acknowledgements

Notes and references

1 M. J. Serpe, *Nature News Views*, 2019, **565**, 438–439.

2 Y. Wang, E. L. Runnerstrom and D. J. Milliron, *Annu. Rev. Chem. Biomol. Eng.*, 2016, **7**, 283–304.

3 C. G. Granqvist, P. C. Lansåker, N. R. Mlyuka, G. A. Niklasson and E. Avendaño, *Sol. Energy Mater. Sol. Cells*, 2009, **93**, 2032–2039.

4 Y. R. Lu, H. H. Hsu, J. L. Chen, H. W. Chang, C. L. Chen, W. C. Chou and C. L. Dong, *Phys. Chem. Chem. Phys.*, 2016, **18**, 5203–5210.

5 Y. Ke, J. Chen, G. Lin, S. Wang, Y. Zhou, J. Yin, P. S. Lee and Y. Long, *Adv. Energy Mater.*, 2019, **9**, 1–38.

6 K. Sauvet, L. Sauques and A. Rougier, *Sol. Energy Mater. Sol. Cells*, 2009, **93**, 2045–2049.

7 J. L. Victor, C. Marcel, L. Sauques, N. Penin and A. Rougier, *Sol. Energy Mater. Sol. Cells*, 2021, **227**, 111113.

8 D. Nunes, A. Pimentel, L. Santos, P. Barquinha, L. Pereira, E. Fortunato and R. Martins, *Chromogenic applications*, 2019.

9 R. W. Pohl, *Proc. Phys. Soc., London*, 1937, **49**, 3–31.

10 J. R. Platt, *J. Chem. Phys.*, 1961, **34**, 862–863.

11 S. K. Deb, *Appl. Opt.*, 1969, **8**, 192–195.

12 W. C. Dautremont-Smith, *Displays*, 1982, **3**, 67–80.

13 W. C. Dautremont-Smith, *Displays*, 1982, **3**, 3–22.

14 R. J. Mortimer, *Annu. Rev. Mater. Res.*, 2011, **41**, 241–268.

15 V. K. Thakur, G. Ding, J. Ma, P. S. Lee and X. Lu, *Adv. Mater.*, 2012, **24**, 4071–4096.

16 V. Rai, R. S. Singh, D. J. Blackwood and D. Zhili, *Adv. Eng. Mater.*, 2020, **22**, 1–23.

17 G. K. Dalapati, A. K. Kushwaha, M. Sharma, V. Suresh, S. Shannigrahi, S. Zhuk and S. Masudy-Panah, *Prog. Mater. Sci.*, 2018, **95**, 42–131.

18 T. He and J. Yao, *Prog. Mater. Sci.*, 2006, **51**, 810–879.

19 R. Tällberg, B. P. Jelle, R. Loonen, T. Gao and M. Hamdy, *Sol. Energy Mater. Sol. Cells*, 2019, **200**, 109828.

20 K. Thummavichai, Y. Xia and Y. Zhu, *Prog. Mater. Sci.*, 2017, **88**, 281–324.

21 S. Wang, M. Liu, L. Kong, Y. Long, X. Jiang and A. Yu, *Prog. Mater. Sci.*, 2016, **81**, 1–54.

22 Y. Cui, Y. Ke, C. Liu, Z. Chen, N. Wang, L. Zhang, Y. Zhou, S. Wang, Y. Gao and Y. Long, *Joule*, 2018, **2**, 1707–1746.

23 M. E. A. Warwick and R. Binions, *J. Mater. Chem. A*, 2014, **2**, 3275–3292.

24 D. Kowalski, D. Kim and P. Schmuki, *Nano Today*, 2013, **8**, 235–264.

25 T. He and J. Yao, *J. Photochem. Photobiol., C*, 2003, **4**, 125–143.

26 M. Mihelčič, A. Šurca Vuk, I. Jerman, B. Orel, F. Švegl, H. Moulki, C. Faure, G. Campet and A. Rougier, *Sol. Energy Mater. Sol. Cells*, 2014, **120**, 116–130.

27 J. Yao, Y. Li, R. C. Massé, E. Uchaker and G. Cao, *Energy Storage Mater.*, 2018, **11**, 205–259.

28 S. Natarajan, S. J. Kim and V. Aravindan, *J. Mater. Chem. A*, 2020, **8**, 9483–9495.

29 L. R. De Jesus, J. L. Andrews, A. Parija and S. Banerjee, *ACS Energy Lett.*, 2018, **3**, 915–931.

30 A. Moretti and S. Passerini, *Adv. Energy Mater.*, 2016, **6**, 1600868.

31 Y. Yue and H. Liang, *Adv. Energy Mater.*, 2017, **7**, 1–32.

32 M. Liu, B. Su, Y. Tang, X. Jiang and A. Yu, *Adv. Energy Mater.*, 2017, **7**, 1–34.

33 J. Wang, H. Tang, L. Zhang, H. Ren, R. Yu, Q. Jin, J. Qi, D. Mao, M. Yang, Y. Wang, P. Liu, Y. Zhang, Y. Wen, L. Gu, G. Ma, Z. Su, Z. Tang, H. Zhao and D. Wang, *Nat. Energy*, 2016, **1**, 1–8.

34 D. Kundu, B. D. Adams, V. Duffort, S. H. Vajargah and L. F. Nazar, *Nat. Energy*, 2016, **1**, 1–8.

35 T. K. Le, M. Kang and S. W. Kim, *Mater. Charact.*, 2019, **153**, 52–59.

36 W. B. Fu, G. L. Shang, X. X. Gong, L. De Zhang and G. T. Fei, *J. Mater. Chem. C*, 2017, **5**, 1471–1478.

37 G. Terán-Escobar, J. Pampel, J. M. Caicedo and M. Lira-Cantú, *Energy Environ. Sci.*, 2013, **6**, 3088–3098.

38 H. Zhang, S. Wang, X. Sun and S. Chen, *J. Mater. Chem. C*, 2017, **5**, 817–823.

39 B. Yan, L. Liao, Y. You, X. Xu, Z. Zheng, Z. Shen, J. Ma, L. Jong and T. Yu, *Adv. Mater.*, 2009, **21**, 2436–2440.

40 W. Wu, M. Wang, J. Ma, Y. Cao and Y. Deng, *Adv. Electron. Mater.*, 2018, **4**, 1–19.

41 Y. T. Wang, W. T. Whang and C. H. Chen, *ACS Appl. Mater. Interfaces*, 2015, **7**, 8480–8487.

42 V. Mounasamy, G. K. Mani and S. Madanagurusamy, *Microchim. Acta*, 2020, **187**, 253.

43 H. Kim, T. K. Le, M. Kang, J. K. Lee, S. D. Park and S. W. Kim, *Mater. Lett.*, 2020, **277**, 128394.

44 G. T. Kim, J. Muster, V. Krstic, J. G. Park, Y. W. Park, S. Roth and M. Burghard, *Appl. Phys. Lett.*, 2000, **76**, 1875–1877.

45 A. B. Cezar, I. L. Graff, J. Varalda, W. H. Schreiner and D. H. Mosca, *J. Appl. Phys.*, 2014, **116**, 163904.

46 M. R. Parida, C. Vijayan, C. S. Rout, C. S. S. Sandeep, R. Philip and P. C. Deshmukh, *J. Phys. Chem. C*, 2011, **115**, 112–117.

47 T. Zhai, H. Liu, H. Li, X. Fang, M. Liao, L. Li, H. Zhou, Y. Koide, Y. Bando and D. Golberg, *Adv. Mater.*, 2010, **22**, 2547–2552.

48 G. Gu, M. Schmid, P. W. Chiu, A. Minett, J. Fraysse, G. T. Kim, S. Roth, M. Kozlov, E. Muñoz and R. H. Baughman, *Nat. Mater.*, 2003, **2**, 316–319.

49 S. Surnev, M. G. Ramsey and F. P. Netzer, *Prog. Surf. Sci.*, 2003, **73**, 117–165.

50 T. K. Le, M. Kang and S. W. Kim, *Ceram. Int.*, 2019, **45**, 15781–15798.

51 S. Ghosh, P. Roy, N. Karmodak, E. D. Jemmis and G. Mugesh, *Angew. Chem.*, 2018, **130**, 4600–4605.

52 F. Natalio, R. André, A. F. Hartog, B. Stoll, K. P. Jochum, R. Wever and W. Tremel, *Nat. Nanotechnol.*, 2012, **7**, 530–535.

53 A. A. Vernekar, D. Sinha, S. Srivastava, P. U. Paramasivam, P. D'Silva and G. Mugesh, *Nat. Commun.*, 2014, **5**, 1–13.

54 K. Qu, P. Shi, J. Ren and X. Qu, *Chem. – Eur. J.*, 2014, **20**, 7501–7506.

55 Y. Ding, G. Ren, G. Wang, M. Lu, J. Liu, K. Li and Y. Lin, *Anal. Chem.*, 2020, **92**, 4583–4591.

56 U.S National Library of Medicine, Search 'VANADIUM PENTOXIDE', https://pubchem.ncbi.nlm.nih.gov/compound/Vanadium-pentoxide).

57 Z. Tong, H. Lv, X. Zhang, H. Yang, Y. Tian, N. Li, J. Zhao and Y. Li, *Sci. Rep.*, 2015, **5**, 1–11.

58 K. Takahashi, Y. Wang and G. Cao, *Appl. Phys. Lett.*, 2005, **86**, 1–3.

59 C. Xiong, A. E. Aliev, B. Gnade and K. J. Balkus, *ACS Nano*, 2008, **2**, 293–301.

60 K. C. Cheng, F. R. Chen and J. J. Kai, *Sol. Energy Mater. Sol. Cells*, 2006, **90**, 1156–1165.

61 Y. Yang, D. Kim and P. Schmuki, *Electrochem. Commun.*, 2011, **13**, 1198–1201.

62 J. M. Gallardo-Amores, N. Biskup, U. Amador, K. Persson, G. Ceder, E. Morán and M. E. Arroyo y De Dompablo, *Chem. Mater.*, 2007, **19**, 5262–5271.

63 M. B. Smirnov, E. M. Roginskii, K. S. Smirnov, R. Baddour-Hadjean and J. P. Pereira-Ramos, *Inorg. Chem.*, 2018, **57**, 9190–9204.

64 R. Baddour-Hadjean, M. B. Smirnov, K. S. Smirnov, V. Y. Kazimirov, J. M. Gallardo-Amores, U. Amador, M. E. Arroyo-De Dompablo and J. P. Pereira-Ramos, *Inorg. Chem.*, 2012, **51**, 3194–3201.

65 V. V. Porsev, A. V. Bandura and R. A. Evarestov, *Acta Mater.*, 2014, **75**, 246–258.

66 P. Balog, D. Orosel, Z. Cancarevic, C. Schön and M. Jansen, *J. Alloys Compd.*, 2007, **429**, 87–98.

67 T. K. Le, M. Kang and S. W. Kim, *Mater. Sci. Semicond. Process.*, 2019, **94**, 15–21.

68 N. Pinna, M. Willinger, K. Weiss, J. Urban and R. Schlögl, *Nano Lett.*, 2003, **3**, 1131–1134.

69 A. Chakrabarti, K. Hermann, R. Druzinic, M. Witko, F. Wagner and M. Petersen, *Phys. Rev. B: Condens. Matter Mater. Phys.*, 1999, **59**, 10583–10590.

70 S. Atzkern, S. Borisenko, M. Knupfer, M. Golden, J. Fink, A. Yaresko and V. Antonov, *Phys. Rev. B: Condens. Matter Mater. Phys.*, 2000, **61**, 12792–12798.

71 J. Haber, M. Witko and R. Tokarz, *Appl. Catal., A*, 1997, **157**, 3–22.

72 S. Beke, *Thin Solid Films*, 2011, **519**, 1761–1771.

73 J. M. Cocciantelli, J. P. Doumerc, M. Pouchard, M. Broussely and J. Labat, *J. Power Sources*, 1991, **34**, 103–111.

74 A. Parija, Y. Liang, J. L. Andrews, L. R. De Jesus, D. Prendergast and S. Banerjee, *Chem. Mater.*, 2016, **28**, 5611–5620.

75 J. Goclon, R. Grybos, M. Witko and J. Hafner, *Phys. Rev. B: Condens. Matter Mater. Phys.*, 2009, **79**, 1–14.

76 K. McColl and F. Corà, *Phys. Chem. Chem. Phys.*, 2019, **21**, 7732–7744.

77 B. Singh, M. K. Gupta, S. K. Mishra, R. Mittal, P. U. Sastry, S. Rols and S. L. Chaplot, *Phys. Chem. Chem. Phys.*, 2017, **19**, 17967–17984.

78 M. Willinger, N. Pinna, D. S. Su and R. Schlögl, *Phys. Rev. B: Condens. Matter Mater. Phys.*, 2004, **69**, 1–7.

79 J. Wisniak, *Educ. Quim.*, 2014, **25**, 455–463.

80 R. Levi, M. Bar-Sadan, A. Albu-Yaron, R. Popovitz-Biro, L. Houben, C. Shahar, A. Enyashin, G. Seifert, Y. Prior and R. Tenne, *J. Am. Chem. Soc.*, 2010, **132**, 11214–11222.

81 V. Petkov, P. Y. Zavalij, S. Lutta, M. S. Whittingham, V. Parvanov and S. Shastri, *Phys. Rev. B: Condens. Matter Mater. Phys.*, 2004, **69**, 3–8.

82 M. Alsawafta, A. Almoabadi, S. Badilescu and V.-V. Truong, *J. Electrochem. Soc.*, 2015, **162**, H466–H472.

83 Z. Tong, X. Zhang, H. Lv, N. Li, H. Qu, J. Zhao, Y. Li and X. Y. Liu, *Adv. Mater. Interfaces*, 2015, **2**, 1500230.

84 S. Liang, Y. Hu, Z. Nie, H. Huang, T. Chen, A. Pan and G. Cao, *Nano Energy*, 2015, **13**, 58–66.

85 K. Zhu, C. Zhang, S. Guo, H. Yu, K. Liao, G. Chen, Y. Wei and H. Zhou, *ChemElectroChem*, 2015, **2**, 1660–1664.

86 M. Li, F. Kong, H. Wang and G. Li, *CrystEngComm*, 2011, **13**, 5317–5320.

87 L. Wu, Y. Yu, X. Han, T. Xu, Y. Zhang, Y. Li and J. Zhi, *J. Mater. Chem. C*, 2013, **1**, 6703–6708.

88 H. Liu and W. Yang, *Energy Environ. Sci.*, 2011, **4**, 4000–4008.

89 K. Zhang, N. Li, X. Ma, Y. Wang, J. Zhao, L. Qiang, X. Li and Y. Li, *J. Electroanal. Chem.*, 2018, **825**, 16–21.

90 S. Sajitha, U. Aparna and B. Deb, *Adv. Mater. Interfaces*, 2019, **6**, 1–9.

91 X. Ren, Y. Liu and W. Guo, *Sep. Purif. Technol.*, 2020, **253**, 117501.

92 G. Li, S. Pang, L. Jiang, Z. Guo and Z. Zhang, *J. Phys. Chem. B*, 2006, **110**, 9383–9386.

93 W. Kang, C. Yan, X. Wang, C. Y. Foo, A. W. Ming Tan, K. J. Zhi Chee and P. S. Lee, *J. Mater. Chem. C*, 2014, **2**, 4727–4732.

94 F. Krumeich, H. J. Muhr, M. Niederberger, F. Bieri, B. Schnyder and R. Nesper, *J. Am. Chem. Soc.*, 1999, **121**, 8324–8331.

95 T. K. Le, M. Kang, V. T. Tran and S. W. Kim, *Mater. Sci. Semicond. Process.*, 2019, **100**, 159–166.

96 K. Tang, Y. Zhang, Y. Shi, J. Cui, X. Shu, Y. Wang, J. Liu, J. Wang, H. H. Tan and Y. Wu, *J. Mater. Chem. C*, 2018, **6**, 12206–12216.

97 C. Han, M. Yan, L. Mai, X. Tian, L. Xu, X. Xu, Q. An, Y. Zhao, X. Ma and J. Xie, *Nano Energy*, 2013, **2**, 916–922.

98 R. Abazari, S. Sanati and L. A. Saghatforoush, *Chem. Eng. J.*, 2014, **236**, 82–90.

99 N. Van Hoa, T. T. H. Quyen, N. H. Nghia, N. Van Hieu and J. J. Shim, *J. Alloys Compd.*, 2017, **702**, 693–699.

100 Q. An, P. Zhang, F. Xiong, Q. Wei, J. Sheng, Q. Wang and L. Mai, *Nano Res.*, 2015, **8**, 481–490.

101 C. Zhang, Z. Chen, Z. Guo and X. W. (David) Lou, *Energy Environ. Sci.*, 2013, **6**, 974–978.

102 X. Rui, Z. Lu, H. Yu, D. Yang, H. H. Hng, T. M. Lim and Q. Yan, *Nanoscale*, 2013, **5**, 556–560.

103 R. Levi, M. Bar-Sadan, A. Albu-Yaron, R. Popovitz-Biro, L. Houben, C. Shahar, A. Enyashin, G. Seifert, Y. Prior and R. Tenne, *J. Am. Chem. Soc.*, 2010, **132**, 11214–11222.

104 C. V. Ramana, R. J. Smith, O. M. Hussain, C. C. Chusuei and C. M. Julien, *Chem. Mater.*, 2005, **17**, 1213–1219.

105 S. Thiagarajan, M. Thaiyan and R. Ganesan, *RSC Adv.*, 2016, **6**, 82581–82590.

106 M. Kang, M. Chu, S. W. Kim and J. W. Ryu, *Thin Solid Films*, 2013, **547**, 198–201.

107 M. Kang, I. Kim, S. W. Kim, J. W. Ryu and H. Y. Park, *Appl. Phys. Lett.*, 2011, **98**, 131907.

108 M. Panagopoulou, D. Vernardou, E. Koudoumas, N. Katsarakis, D. Tsoukalas and Y. S. Raptis, *J. Phys. Chem. C*, 2017, **121**, 70–79.

109 P. Singh and D. Kaur, *J. Appl. Phys.*, 2008, **103**, 043507.

110 H. N. Cui, V. Teixeira, L. J. Meng, R. Wang, J. Y. Gao and E. Fortunato, *Thin Solid Films*, 2008, **516**, 1484–1488.

111 T. Gallasch, T. Stockhoff, D. Baither and G. Schmitz, *J. Power Sources*, 2011, **196**, 428–435.

112 G. Y. Karaca, E. Eren, C. Alver, U. Koc, E. Uygun, L. Oksuz and A. U. Oksuz, *Electroanalysis*, 2017, **29**, 1324–1331.

113 H. A. Le, S. Chin, E. Park, G. Bae and J. Jurng, *Chem. Vap. Deposition*, 2012, **18**, 6–9.

114 H. Yin, K. Yu, H. Peng, Z. Zhang, R. Huang, J. Travas-Sejdic and Z. Zhu, *J. Mater. Chem.*, 2012, **22**, 5013–5019.

115 Y. Wang, Q. Su, C. H. Chen, M. L. Yu, G. J. Han, G. Q. Wang, K. Xin, W. Lan and X. Q. Liu, *J. Phys. D: Appl. Phys.*, 2010, **43**, 185102.

116 M. C. Wu and C. S. Lee, *J. Solid State Chem.*, 2009, **182**, 2285–2289.

117 L. S. Price, I. P. Parkin, M. N. Field, A. M. E. Hardy, R. J. H. Clark, T. G. Hibbert and K. C. Molloy, *J. Mater. Chem.*, 2000, **10**, 527–530.

118 A. Othonos, C. Christofides and M. Zervos, *Appl. Phys. Lett.*, 2013, **103**, 133112.

119 H. Groult, E. Balnois, A. Mantoux, K. Le Van and D. Lincot, *Appl. Surf. Sci.*, 2006, **252**, 5917–5925.

120 S. Kumar, A. Qadir, F. Maury and N. Bahlawane, *ACS Appl. Mater. Interfaces*, 2017, **9**, 21447–21456.

121 D. Barreca, L. Armelao, F. Caccavale, V. Di Noto, A. Gregori, G. A. Rizzi and E. Tondello, *Chem. Mater.*, 2000, **12**, 98–103.

122 C. Piccirillo, R. Binions and I. P. Parkin, *Chem. Vap. Deposition*, 2007, **13**, 145–151.

123 J. Musschoot, D. Deduytsche, H. Poelman, J. Haemers, R. L. Van Meirhaeghe, S. Van den Berghe and C. Detavernier, *J. Electrochem. Soc.*, 2009, **156**, P122.

124 M. Najdoski, V. Koleva and A. Samet, *J. Phys. Chem. C*, 2014, **118**, 9636–9646.

125 Y. Yang, S. P. Albu, D. Kim and P. Schmuki, *Angew. Chem.*, 2011, **123**, 9237–9241.

126 S. Wang, S. Li, Y. Sun, X. Feng and C. Chen, *Energy Environ. Sci.*, 2011, **4**, 2854–2857.

127 X. F. Zhang, K. X. Wang, X. Wei and J. S. Chen, *Chem. Mater.*, 2011, **23**, 5290–5292.

128 M. M. Margoni, S. Mathuri, K. Ramamurthi, R. R. Babu and K. Sethuraman, *Appl. Surf. Sci.*, 2017, **418**, 280–290.

129 H. G. Wang, D. L. Ma, Y. Huang and X. B. Zhang, *Chem. – Eur. J.*, 2012, **18**, 8987–8993.

130 P. Sahatiya, C. S. K. Reddy and S. Badhulika, *J. Mater. Chem. C*, 2017, **5**, 12728–12736.

131 S. Datta, C. Jo, M. De Volder and L. Torrente-Murciano, *ACS Appl. Mater. Interfaces*, 2020, **12**, 18803–18812.

132 J. Mu, J. Wang, J. Hao, P. Cao, S. Zhao, W. Zeng, B. Miao and S. Xu, *Ceram. Int.*, 2015, **41**, 12626–12632.

133 N. Wang, Y. Zhang, T. Hu, Y. Zhao and C. Meng, *Curr. Appl. Phys.*, 2015, **15**, 493–498.

134 N. Baig, I. Kammakakam, W. Falath and I. Kammakakam, *Mater. Adv.*, 2021, **2**, 1821–1871.

135 S. Khan and K. Singh, *Sci. Rep.*, 2020, **10**, 1–11.

136 C. Díaz-Guerra and J. Piqueras, *Cryst. Growth Des.*, 2008, **8**, 1031–1034.

137 P. Taylor, M. Kusper, T. Hesabizadeh, L. D. Geoffrion, F. Watanabe, E. Herth and G. Guisbiers, *Nanoscale Adv.*, 2021, **3**, 1954–1961.

138 Z. L. Wang, D. Xu, L. M. Wang and X. B. Zhang, *ChemPlusChem*, 2012, **77**, 124–128.

139 A. M. Glushenkov, V. I. Stukachev, M. F. Hassan, G. G. Kuvshinov, H. K. Liu and Y. Chen, *Cryst. Growth Des.*, 2008, **8**, 3661–3665.

140 Y. Zou, C. Wang, H. Chen, H. Ji, Q. Zhu and W. Yang, *Green Energy Environ.*, 2021, **6**, 169–175.

141 S. Beke, L. Korösi, S. Papp, L. Nánai, A. Oszkó, J. G. Kiss and V. Safarov, *Appl. Surf. Sci.*, 2007, **254**, 1363–1368.

142 W. Cheng, J. He, K. E. Dettelbach, N. J. J. Johnson, R. S. Sherbo and C. P. Berlinguette, *Chem*, 2018, **4**, 821–832.

143 H. Song, C. Zhang, Y. Liu, C. Liu, X. Nan and G. Cao, *J. Power Sources*, 2015, **294**, 1–7.

144 R. Wang, S. Yang, R. Deng, W. Chen, Y. Liu, H. Zhang and G. S. Zakharova, *RSC Adv.*, 2015, **5**, 41050–41058.

145 Z. Tong, J. Hao, K. Zhang, J. Zhao, B. L. Su and Y. Li, *J. Mater. Chem. C*, 2014, **2**, 3651–3658.

146 X. Chen, E. Pomerantseva, P. Banerjee, K. Gregorczyk, R. Ghodssi and G. Rubloff, *Chem. Mater.*, 2012, **24**, 1255–1261.

147 C. Liu, N. Kim, G. W. Rubloff and S. B. Lee, *Nanoscale*, 2017, **9**, 11566–11573.

148 C. Liu, E. I. Gillette, X. Chen, A. J. Pearse, A. C. Kozen, M. A. Schroeder, K. E. Gregorczyk, S. B. Lee and G. W. Rubloff, *Nat. Nanotechnol.*, 2014, **9**, 1031–1039.

149 L. Li, U. Steiner and S. Mahajan, *J. Mater. Chem.*, 2010, **20**, 7131–7134.

150 Z. Tong, N. Li, H. Lv, Y. Tian, H. Qu, X. Zhang, J. Zhao and Y. Li, *Sol. Energy Mater. Sol. Cells*, 2016, **146**, 135–143.

151 X. Liu, Y. Hu, G. Jia, H. Zhang, H. Jiang and C. Li, *J. Mater. Chem. A*, 2016, **4**, 12030–12035.

152 F. Guo, M. Fan, P. Jin, H. Chen, Y. Wu, G. D. Li and X. Zou, *CrystEngComm*, 2016, **18**, 4068–4073.

153 P. M. Marley, T. A. Abtew, K. E. Farley, G. A. Horrocks, R. V. Dennis, P. Zhang and S. Banerjee, *Chem. Sci.*, 2015, **6**, 1712–1718.

154 J. C. Parker, D. J. Lam, Y. N. Xu and W. Y. Ching, *Phys. Rev. B: Condens. Matter Mater. Phys.*, 1990, **42**, 5289–5293.

155 R. Irani, S. M. Rozati and S. Beke, *Mater. Chem. Phys.*, 2013, **139**, 489–493.

156 E. Streng, O. Nilsen and H. Fjellvåg, *J. Phys. Chem. C*, 2012, **116**, 19444–19450.

157 W. Lambrecht, B. Djafari-Rouhani and J. Vennik, *J. Phys. C: Solid State Phys.*, 1981, **14**, 4785–4795.

158 A. Talledo and C. G. Granqvist, *J. Appl. Phys.*, 1995, **77**, 4655–4666.

159 D. O. Scanlon, A. Walsh, B. J. Morgan and G. W. Watson, *J. Phys. Chem. C*, 2008, **112**, 9903–9911.

160 Z. R. Xiao and G. Y. Guo, *J. Chem. Phys.*, 2009, **130**, 214704.

161 T. M. Tolhurst, B. Leedahl, J. L. Andrews, P. M. Marley, S. Banerjee and A. Moewes, *Phys. Chem. Chem. Phys.*, 2016, **18**, 15798–15806.

162 M. Beaudoin, M. Meunier and C. J. Arsenault, *Phys. Rev. B: Condens. Matter Mater. Phys.*, 1993, **47**, 2197–2202.

163 J. Tauc, *Optical properties of solids*, Academic Press, New York, 1966.

164 T. D. H. Nguyen, K. D. Vo, H. D. Pham, T. M. D. Huynh and M.-F. Lin, *Comput. Mater. Sci.*, 2021, **198**, 110675.

165 P. D. Raj, S. Gupta and M. Sridharan, *Ceram. Int.*, 2017, **43**, 9401–9407.

166 C. R. Aita, Y. L. Liu, M. L. Kao and S. D. Hansen, *J. Appl. Phys.*, 1986, **60**, 749–753.

167 J. Song, X. Gu, Y. Cao and H. Zhang, *J. Mater. Chem. A*, 2019, **7**, 10543–10551.

168 M. B. Sahana, C. Sudakar, C. Thapa, G. Lawes, V. M. Naik, R. J. Baird, G. W. Auner, R. Naik and K. R. Padmanabhan, *Mater. Sci. Eng., B*, 2007, **143**, 42–50.

169 R. Santos, J. Loureiro, A. Nogueira, E. Elangovan, J. V. Pinto, J. P. Veiga, T. Busani, E. Fortunato, R. Martins and I. Ferreira, *Appl. Surf. Sci.*, 2013, **282**, 590–594.

170 A. Kumar, P. Singh, N. Kulkarni and D. Kaur, *Thin Solid Films*, 2008, **516**, 912–918.

171 N. Singh, A. Umar, N. Singh, H. Fouad, O. Y. Alothman and F. Z. Haque, *Mater. Res. Bull.*, 2018, **108**, 266–274.

172 A. Venkatesan, N. R. Krishna Chandar, A. Kandasamy, M. Karl Chinnu, K. N. Marimuthu, R. Mohan Kumar and R. Jayavel, *RSC Adv.*, 2015, **5**, 21778–21785.

173 Y. Iida and Y. Kanno, *J. Mater. Process. Technol.*, 2009, **209**, 2421–2427.

174 F. N. I. Sari, S. H. Lu and J. M. Ting, *J. Am. Ceram. Soc.*, 2020, **103**, 2252–2261.

175 T. K. Le, M. Kang, S. W. Han and S. W. Kim, *RSC Adv.*, 2018, **8**, 41317–41322.

176 M. Aslam, I. M. I. Ismail, N. Salah, S. Chandrasekaran, M. T. Qamar and A. Hameed, *J. Hazard. Mater.*, 2015, **286**, 127–135.

177 D. Dreifus, M. P. F. Godoy, A. C. Rabelo, A. D. Rodrigues, Y. G. Gobato, P. C. Camargo, E. C. Pereira and A. J. A. De Oliveira, *J. Phys. D: Appl. Phys.*, 2015, **48**, 445002.

178 Q. Wang, M. Brier, S. Joshi, A. Puntambekar and V. Chakrapani, *Phys. Rev. B*, 2016, **94**, 245305.

179 D. Liu, Y. Liu, B. B. Garcia, Q. Zhang, A. Pan, Y. H. Jeong and G. Cao, *J. Mater. Chem.*, 2009, **19**, 8789–8795.

180 M. Zhu, D. Zhang, S. Jiang, S. Liu, H. Qi and Y. Yang, *Ceram. Int.*, 2021, **47**, 15491–15499.

181 S. Surendren and B. Deb, *Electrochim. Acta*, 2021, **389**, 138629.

182 H. Shanak, H. Schmitt, J. Nowoczin and K. H. Ehses, *J. Mater. Sci.*, 2005, **40**, 3467–3474.

183 C. V. Ramana, O. M. Hussain, B. S. Naidu and P. J. Reddy, *Thin Solid Films*, 1997, **305**, 219–226.

184 W. Zhang, H. Li, W. W. Yu and A. Y. Elezzabi, *Light: Sci. Appl.*, 2020, **9**, 121.

185 W. Avansi, V. R. De Mendonça, O. F. Lopes and C. Ribeiro, *RSC Adv.*, 2015, **5**, 12000–12006.

186 C. V. Ramana, O. M. Hussain, S. Uthanna and B. S. Naidu, *Opt. Mater.*, 1998, **10**, 101–107.

187 S. R. Indhumathi, M. Manoj Cristopher, P. Karthick, M. Dhivya Pushpa, B. Poornima, C. Gopalakrishnan and K. Jeyadheepan, *Mater. Sci. Semicond. Process.*, 2019, **100**, 185–191.

188 M. M. Margoni, S. Mathuri, K. Ramamurthi, R. R. Babu, V. Ganesh and K. Sethuraman, *Appl. Surf. Sci.*, 2018, **449**, 193–202.

189 S. Thiagarajan, M. Thaiyan and R. Ganesan, *New J. Chem.*, 2015, **39**, 9471–9479.

190 A. A. Mane, V. V. Ganbavle, M. A. Gaikwad, S. S. Nikam, K. Y. Rajpure and A. V. Moholkar, *J. Anal. Appl. Pyrolysis*, 2015, **115**, 57–65.

191 V. X. Hien, D. D. Nhat, N. T. Nghi, L. H. Phuoc, C. T. Khoa, D. D. Vuong and N. D. Chien, *Mater. Sci. Semicond. Process.*, 2021, **126**, 105670.

192 X. Li, K. Perera, J. He, A. Gumyusenge and J. Mei, *J. Mater. Chem. C*, 2019, **7**, 12761–12789.

193 C. F. Armer, M. Lübke, I. Johnson, K. McColl, F. Cora, J. S. Yeoh, M. V. Reddy, J. A. X. Li and A. Lowe, *J. Solid State Electrochem.*, 2018, **24**, 3703–3716.

194 M. Abyazisani, M. M. Bagheri-Mohagheghi and M. R. Benam, *Mater. Sci. Semicond. Process.*, 2015, **31**, 693–699.

195 H. Chaudhary, K. Chaudhary, S. Zulfiqar, M. S. Saif, I. A. Alsafari, I. Shakir, P. O. Agboola, M. Safdar and M. F. Warsi, *Ceram. Int.*, 2021, **47**, 32521–32533.

196 M. Panagopoulou, D. Vernardou, E. Koudoumas, D. Tsoukalas and Y. S. Raptis, *Electrochim. Acta*, 2019, **321**, 134743.

197 L. H. Slewa, T. A. Abbas and N. M. Ahmed, *Sens. Actuators, B*, 2020, **305**, 127515.

198 Y. Yang, F. Teng, Y. Kan, L. Yang, W. Gu, J. Xu, Y. Zhao, X. Du and M. Ren, *CrystEngComm*, 2016, **18**, 3064–3078.

199 V. Balasubramani, J. Chandrasekaran, V. Manikandan, T. K. Le, R. Marnadu and P. Vivek, *J. Solid State Chem.*, 2021, **301**, 122289.

200 V. Balasubramani, J. Chandrasekaran, V. Manikandan, T. K. Le, R. Marnadu and P. Vivek, *Surf. Interfaces*, 2021, **25**, 101297.

201 G. Wu, K. Du, C. Xia, X. Kun, J. Shen, B. Zhou and J. Wang, *Thin Solid Films*, 2005, **485**, 284–289.

202 A. Qadir, T. K. Le, M. Malik, K. A. Amedome Min-Dianey, I. Saeed, Y. Yu, J. R. Choi and P. V. Pham, *RSC Adv.*, 2021, **11**, 23860–23880.

203 Z. Tong, S. Liu, X. Li, Y. Ding, J. Zhao and Y. Li, *Electrochim. Acta*, 2016, **222**, 194–202.

204 M. Lee, W. G. Hong, H. Y. Jeong, S. K. Balasingam, Z. Lee, S. J. Chang, B. H. Kim and Y. Jun, *Nanoscale*, 2014, **6**, 11066–11071.

205 B. R. Koo, J. W. Bae and H. J. Ahn, *Ceram. Int.*, 2019, **45**, 12325–12330.

206 C. Glynn, D. Creedon, H. Geaney, E. Armstrong, T. Collins, M. A. Morris and C. O'Dwyer, *Sci. Rep.*, 2015, **5**, 1–15.

207 R. Narayanan, A. Dewan and D. Chakraborty, *RSC Adv.*, 2018, **8**, 8596–8606.

208 S. Hassab, D. E. Shen, A. M. Österholm, M. Da Rocha, G. Song, Y. Alesanco, A. Viñuales, A. Rougier, J. R. Reynolds and J. Padilla, *Sol. Energy Mater. Sol. Cells*, 2018, **185**, 54–60.

209 N. A. Chernova, M. Roppolo, A. C. Dillon and M. S. Whittingham, *J. Mater. Chem.*, 2009, **19**, 2526–2552.

210 M. S. Whittingham, *J. Electrochem. Soc.*, 1976, **123**, 315–320.

211 D. W. Murphy, P. A. Christian, F. J. Disalvo and J. V. Waszczak, *Inorg. Chem.*, 1979, **18**, 2800–2803.

212 M. Muñoz-Castro, F. Berkemeier, G. Schmitz, A. Buchheit and H. D. Wiemhöfer, *J. Appl. Phys.*, 2016, **120**, 135106.

213 G. A. Horrocks, M. F. Likely, J. M. Velazquez and S. Banerjee, *J. Mater. Chem. A*, 2013, **1**, 15265–15277.

214 C. Costa, C. Pinheiro, I. Henriques and C. A. T. Laia, *ACS Appl. Mater. Interfaces*, 2012, **4**, 5266–5275.

215 I. Mjejri and A. Rougier, *J. Mater. Chem. C*, 2020, **8**, 3631–3638.

216 I. Mjejri, M. Gaudon, G. Song, C. Labrugère and A. Rougier, *ACS Appl. Energy Mater.*, 2018, **1**, 2721–2729.

217 W. Zhang, H. Li, M. Al-Hussein and A. Y. Elezzabi, *Adv. Opt. Mater.*, 2020, **8**, 1901224.

218 H. Liu, X. Liang, T. Jiang, Y. Zhang, S. Liu, X. Wang, X. Fan, X. Huai, Y. Fu, Z. Geng and D. Zhang, *Electrochim. Acta*, 2022, **404**, 139784.

219 A. Branco, J. Belchior, L. C. Branco and F. Pina, *RSC Adv.*, 2013, **3**, 25627–25630.

220 Z. Y. Li, X. Z. Lin and Q. H. Wu, *Chin. J. Chem. Phys.*, 2009, **22**, 241–245.

221 M. J. Walker, A. Jarry, N. Pronin, J. Ballard, G. W. Rubloff, L. J. Brillson and L. J. Brillson, *J. Mater. Chem. A*, 2020, **8**, 11800–11810.

222 A. Jarry, M. Walker, S. Theodoru, L. J. Brillson and G. W. Rubloff, *Chem. Mater.*, 2020, **32**, 7226–7236.

223 R. Basu, A. K. Prasad, S. Dhara and A. Das, *J. Phys. Chem. C*, 2016, **120**, 26539–26543.

224 R. J. Colton, PhD thesis, University of Pittsburgh, Pittsburgh, 1978.

225 R. J. Colton, A. M. Guzman and J. W. Rabalais, *Acc. Chem. Res.*, 1978, **11**, 170–176.

226 R. J. Colton, A. M. Guzman and J. W. Rabalais, *J. Appl. Phys.*, 1978, **49**, 409–416.

227 P. G. Dickens, S. J. French, A. T. Hight and M. F. Pye, *Mater. Res. Bull.*, 1979, **14**, 1295–1299.

228 S. Sato and Y. Seino, *Electronics and Communications in Japan (Part I: Communications)*, 1982, **65**, 104–111.

229 R. D. Rauh and S. F. Cogan, *Solid State Ionics*, 1988, **28–30**, 1707–1714.

230 T. Yoshino, N. Baba and Y. Kouda, *Jpn. J. Appl. Phys.*, 1987, **26**, 782–783.

231 P. V. Ashrit, K. Benaissa, G. Bader, F. E. Girouard and V. Van Truong, *Solid State Ionics*, 1993, **59**, 47–57.

232 S. F. Cogan, N. M. Nguyen, S. J. Perrotti and R. D. Rauh, *J. Appl. Phys.*, 1989, **66**, 1333–1337.

233 D. Wruck, S. Ramamur and M. Rubin, *Thin Solid Films*, 1989, **182**, 79–86.

234 K. Nagase, Y. Shimizu, N. Miura and N. Yamazoe, *Appl. Phys. Lett.*, 1994, **64**, 1059–1061.

235 Z. S. Guan, J. N. Yao, Y. A. Yang and B. H. Loo, *J. Electroanal. Chem.*, 1998, **443**, 175–179.

236 Z. Wang, J. Chen and X. Hu, *Thin Solid Films*, 2000, **375**, 238–241.

237 K. Nagase, Y. Shimizu, N. Miura and N. Yamazoe, *Appl. Phys. Lett.*, 1992, **60**, 802–804.

238 K. Nagase, Y. Shimizu, N. Miura and N. Yamazoe, *Appl. Phys. Lett.*, 1992, **61**, 243–245.

239 S. F. Cogan, N. M. Nguyen, S. J. Perrotti and R. D. Rauh, *Opt. Mater.*, 1989, **1016**, 57.

240 H. H. Afify, M. E. Hassan, A. M. Badr and H. A. Elsheikh, *Int. J. Thin Film Sci. Technol.*, 2018, **7**, 1–5.

241 C. E. Patil, N. L. Tarwal, P. S. Shinde, H. P. Deshmukh and P. S. Patil, *J. Phys. D: Appl. Phys.*, 2009, **42**, 025404–025410.

242 S. Zhang, S. Chen, Y. Luo, B. Yan, Y. Gu, F. Yang and Y. Cao, *J. Alloys Compd.*, 2020, **842**, 155882.

243 A. K. Surca, G. Dražič and M. Mihelčič, *Sol. Energy Mater. Sol. Cells*, 2019, **196**, 185–199.

244 C. Wang, X. Zhang, S. Liu, H. Zhang, Q. Wang, C. Zhang, J. Gao, L. Liang and H. Cao, *ACS Appl. Energy Mater.*, 2022, **5**, 88–97.

245 Y. Qi, K. Qin, Y. Zou, L. Lin, Z. Jian and W. Chen, *Appl. Surf. Sci.*, 2020, **514**, 145950.

246 M. R. J. Scherer, L. Li, P. M. S. Cunha, O. A. Scherman and U. Steiner, *Adv. Mater.*, 2012, **24**, 1217–1221.

247 S. Beke, S. Giorgio, L. Korösi, L. Nánai and W. Marine, *Thin Solid Films*, 2008, **516**, 4659–4664.

248 I. Mjejri, M. Gaudon and A. Rougier, *Sol. Energy Mater. Sol. Cells*, 2019, **198**, 19–25.

249 Z. Tong, H. Yang, L. Na, H. Qu, X. Zhang, J. Zhao and Y. Li, *J. Mater. Chem. C*, 2015, **3**, 3159–3166.

250 D. Ge, L. Yang, Z. Tong, Y. Ding, W. Xin, J. Zhao and Y. Li, *Electrochim. Acta*, 2013, **104**, 191–197.

251 D. Wei, M. R. J. Scherer, C. Bower, P. Andrew, T. Ryhänen and U. Steiner, *Nano Lett.*, 2012, **12**, 1857–1862.

252 M. R. J. Scherer and U. Steiner, *Electrochromic Materials and Devices*, 2015, pp. 311–336.

253 Y. S. Hsiao, C. W. Chang-Jian, W. L. Syu, S. C. Yen, J. H. Huang, H. C. Weng, C. Z. Lu and S. C. Hsu, *Appl. Surf. Sci.*, 2021, **542**, 148498.

254 Y. M. Li and T. Kudo, *Sol. Energy Mater. Sol. Cells*, 1995, **39**, 179–190.

255 C. E. Patil, P. R. Jadhav, N. L. Tarwal, H. P. Deshmukh, M. M. Karanjkar and P. S. Patil, *Mater. Chem. Phys.*, 2011, **126**, 711–716.

256 U. Tritschler, F. Beck, H. Schlaad and H. Cölfen, *J. Mater. Chem. C*, 2015, **3**, 950–954.

257 S. Kim and M. Taya, *Sol. Energy Mater. Sol. Cells*, 2012, **107**, 225–229.

258 S. Kim, M. Taya and C. Xu, *J. Electrochem. Soc.*, 2009, **156**, E40.

259 B. N. Reddy, R. Mukkabla, M. Deepa and P. Ghosal, *RSC Adv.*, 2015, **5**, 31422–31433.

260 S. Jiang, Z. Li, S. Huang, S. Lu, Y. Yu, G. Mou, J. Xu, Q. Zhu, X. Tan, X. Zhu and G. S. Zakharova, *J. Electrochem. Soc.*, 2014, **161**, H684–H688.

261 M. Zhi, W. Huang, Q. Shi, B. Peng and K. Ran, *J. Electrochem. Soc.*, 2016, **163**, H891–H895.

262 G. F. Zhao, W. Q. Wang, X. L. Wang, X. H. Xia, C. D. Gu and J. P. Tu, *J. Mater. Chem. C*, 2019, **7**, 5702–5709.

263 Y. Liu, C. Jia, Z. Wan, X. Weng, J. Xie and L. Deng, *Sol. Energy Mater. Sol. Cells*, 2015, **132**, 467–475.

264 R. K. Jain, A. Khanna, Y. K. Gautam and B. P. Singh, *Appl. Surf. Sci.*, 2021, **536**, 147804.

265 W. He, Y. Liu, Z. Wan and C. Jia, *RSC Adv.*, 2016, **6**, 68997–69006.

266 A. Kim, G. Kalita and J. H. Kim, *Nanomaterials*, 2021, **11**, 3213.

267 J.-L. Wang, J.-W. Liu, S.-Z. Sheng, Z. He, J. Gao and S.-H. Yu, *Nano Lett.*, 2021, **21**, 9203–9209.

268 P. Kounavis, M. Vomvas, M. Mytilineou, M. Roilos and L. Murawski, *J. Phys. C-Solid State Phys.*, 1988, **21**, 967–973.

269 F. Coustier, J. Hill, B. B. Owens, S. Passerini and W. H. Smyrl, *J. Electrochem. Soc.*, 1999, **146**, 1355–1360.

270 H. Kim, T. K. Le, M. Kang, J. K. Lee, S. D. Park and S. W. Kim, *Ceram. Int.*, 2021, **47**, 8834–8839.

271 S. Iwanaga, M. Marciniak, R. B. Darling and F. S. Ohuchi, *J. Appl. Phys.*, 2007, **101**, 123709.

272 M. Li, D. Weng, Y. Wei, J. Zheng and C. Xu, *Electrochim. Acta*, 2017, **248**, 206–214.

273 J. W. Bae, B. R. Koo and H. J. Ahn, *Ceram. Int.*, 2019, **45**, 7137–7142.

274 Y. Wei, J. Zhou, J. Zheng and C. Xu, *Electrochim. Acta*, 2015, **166**, 277–284.

275 G. Salek, B. Bellanger, I. Mjejri, M. Gaudon and A. Rougier, *Inorg. Chem.*, 2016, **55**, 9838–9847.

276 Y. Lu, L. Liu, D. Mandler and P. S. Lee, *J. Mater. Chem. C*, 2013, **1**, 7380–7386.

277 C. O. Avellaneda and L. O. S. Bulhões, *Sol. Energy Mater. Sol. Cells*, 2006, **90**, 444–451.

278 A. Jin, W. Chen, Q. Zhu and Z. Jian, *Electrochim. Acta*, 2010, **55**, 6408–6414.

279 X. Zhang, W. Li, X. Chen, Y. Zhao, L. Wang, M. Chen, Z. Li and Y. Li, *Chem. Commun.*, 2020, **56**, 10062–10065.

280 S. Oukassi, C. Giroud-Garampon, C. Dubarry, C. Ducros and R. Salot, *Sol. Energy Mater. Sol. Cells*, 2016, **145**, 2–7.

281 H. Park, D. S. Kim, S. Y. Hong, C. Kim, J. Y. Yun, S. Y. Oh, S. W. Jin, Y. R. Jeong, G. T. Kim and J. S. Ha, *Nanoscale*, 2017, **9**, 7631–7640.

282 P. Yang, P. Sun and W. Mai, *Mater. Today*, 2016, **19**, 394–402.

283 L. Wang, M. Guo, J. Zhan, X. Jiao, D. Chen and T. Wang, *J. Mater. Chem. A*, 2020, **8**, 17098–17105.

284 P. Zhang, F. Zhu, F. Wang, J. Wang, R. Dong, X. Zhuang, O. G. Schmidt and X. Feng, *Adv. Mater.*, 2017, **29**, 1–7.

285 C. O'Dwyer, *Adv. Mater.*, 2016, **28**, 5681–5688.

286 B. D. Boruah, B. Wen, S. Nagane, X. Zhang, S. D. Stranks, A. Boies and M. De Volder, *ACS Energy Lett.*, 2020, **5**, 3132–3139.

287 C. Seo, H. Cheong and S. H. Lee, *Sol. Energy Mater. Sol. Cells*, 2008, **92**, 190–193.

288 Y. K. Ho, C. C. Chang, D. H. Wei, C. L. Dong, C. L. Chen, J. L. Chen, W. L. Jang, C. C. Hsu, T. S. Chan, K. Kumar, C. L. Chang and M. K. Wu, *Thin Solid Films*, 2013, **544**, 461–465.

289 G. Rizzo, A. Arena, A. Bonavita, N. Donato, G. Neri and G. Saitta, *Thin Solid Films*, 2010, **518**, 7124–7127.

290 W. L. Jang, Y. M. Lu, C. L. Chen, Y. R. Lu, C. L. Dong, P. H. Hsieh, W. S. Hwang, J. L. Chen, J. M. Chen, T. S. Chan, J. F. Lee and W. C. Chou, *Phys. Chem. Chem. Phys.*, 2014, **16**, 4699–4708.

291 V. Wittwer, M. Datz, J. Ell, A. Georg, W. Graf and G. Walze, *Sol. Energy Mater. Sol. Cells*, 2004, **84**, 305–314.

292 H. Nakagawa, N. Yamamoto, S. Okazaki, T. Chinzei and S. Asakura, *Sens. Actuators, B*, 2003, **93**, 468–474.

293 R. Baetens, B. P. Jelle and A. Gustavsen, *Sol. Energy Mater. Sol. Cells*, 2010, **94**, 87–105.

294 L. F. Zhu, J. C. She, J. Y. Luo, S. Z. Deng, J. Chen and N. S. Xu, *J. Phys. Chem. C*, 2010, **114**, 15504–15509.

295 C. L. Chen, C. L. Dong, Y. K. Ho, C. C. Chang, D. H. Wei, T. C. Chan, J. L. Chen, W. L. Jang, C. C. Hsu, K. Kumar and M. K. Wu, *Europhys. Lett.*, 2013, **101**, 17006.

296 W. Jin, S. Yan, L. An, W. Chen, S. Yang, C. Zhao and Y. Dai, *Sens. Actuators, B*, 2015, **206**, 284–290.

297 D. Wang, K. Gu, Q. Zhao, C. Zhai, T. Yang, Q. Lu, J. Zhang and M. Zhang, *New J. Chem.*, 2018, **42**, 14188–14193.

298 P. Liu, S.-H. Lee, H. M. Cheong, C. E. Tracy, J. R. Pitts and R. D. Smith, *J. Electrochem. Soc.*, 2002, **149**, H76.

299 Y. R. Lu, T. Z. Wu, H. W. Chang, J. L. Chen, C. L. Chen, D. H. Wei, J. M. Chen, W. C. Chou and C. L. Dong, *Phys. Chem. Chem. Phys.*, 2017, **19**, 14224–14229.

300 W. L. Jang, Y. M. Lu, Y. R. Lu, C. L. Chen, C. L. Dong, W. C. Chou, J. L. Chen, T. S. Chan, J. F. Lee, C. W. Pao and W. S. Hwang, *Thin Solid Films*, 2013, **544**, 448–451.

301 C. C. Chang, J. Y. Luo, T. K. Chen, K. W. Yeh, T. W. Huang, C. H. Hsu, W. H. Chao, C. T. Ke, P. C. Hsu, M. J. Wang and M. K. Wu, *Thin Solid Films*, 2010, **519**, 1552–1557.

302 M. Ranjbar, S. M. Mahdavi and A. Iraji Zad, *Sol. Energy Mater. Sol. Cells*, 2008, **92**, 878–883.

303 C. Imawan, H. Steffes, F. Solzbacher and E. Obermeier, *Sens. Actuators, B*, 2001, **77**, 346–351.

304 N. J. K. J. N. Huiberts, R. Griessen, J. H. Rector, R. J. Wijngaarden, J. P. Dekker and D. G. de Groot, *Nature*, 1996, **380**, 231–234.

305 W. Lohstroh, R. J. Westerwaal, B. Noheda, S. Enache, I. A. M. E. Giebels, B. Dam and R. Griessen, *Phys. Rev. Lett.*, 2004, **93**, 2–5.

306 K. Yoshimura, C. Langhammer and B. Dam, *MRS Bull.*, 2013, **38**, 495–503.

307 H. Miyazaki, T. Matsuura and T. Ota, *RSC Adv.*, 2017, **7**, 2388–2391.

308 A. Gavriluk, *Chromic Materials, Phenomena and their Technological Applications*, 2009.

309 S. Nishio and M. Kakihana, *Chem. Mater.*, 2002, **14**, 3730–3733.

310 Z. Liu, G. Fang, Y. Wang, Y. Bai and K. L. Yao, *J. Phys. D: Appl. Phys.*, 2000, **33**, 2327–2332.

311 M. Kang, E. Oh, I. Kim, S. W. Kim, J. W. Ryu and Y. G. Kim, *Curr. Appl. Phys.*, 2012, **12**, 489–493.

312 Q. J. Wang, H. Wang, Z. H. Zhou, J. Zuo and C. L. Zhang, *Nanoscale*, 2020, **12**, 21368–21375.

313 S. Krishnakumar and C. Menon, *Phys. Status Solidi A*, 1996, **153**, 439.

314 A. Gavriluk and T. Lanskaya, *Tech. Phys. Lett.*, 1994, **20**, 219–221.

315 F. Xie, W. C. H. Choy, C. Wang, X. Li, S. Zhang and J. Hou, *Adv. Mater.*, 2013, **25**, 2051–2055.

316 M. Batzill, *Energy Environ. Sci.*, 2011, **4**, 3275–3286.

317 A. Ganguly, O. Anjaneyulu, K. Ojha and A. K. Ganguli, *CrystEngComm*, 2015, **17**, 8978–9001.

318 A. Gavriluk, U. Tritthart and W. Gey, *Phys. Chem. Chem. Phys.*, 2011, **13**, 9490–9497.

319 Y. Wang, L. Pan, Y. Li and A. I. Gavriluk, *Appl. Surf. Sci.*, 2014, **314**, 384–391.

320 T. Tai Chow, C. Li and Z. Lin, *Sol. Energy Mater. Sol. Cells*, 2010, **94**, 212–220.

321 A. Gavriluk, *Sov. Tech. Phys. Lett.*, 1984, **10**, 6.

322 Y. Iida and Y. Kanno, *Jpn. J. Appl. Phys.*, 2008, **47**, 667–670.

323 J. Gomez-Hermoso-de-Mendoza, H. S. Barud, J. Gutierrez and A. Tercjak, *Carbohydr. Polym.*, 2019, **208**, 50–58.

324 Z. Yang, C. Ko and S. Ramanathan, *Annu. Rev. Mater. Res.*, 2011, **41**, 337–367.

325 R. Basu and S. Dhara, *J. Appl. Phys.*, 2018, **123**, 161550.

326 A. Pérez-Pacheco, D. R. Acosta-Najarro, R. Castañeda-Guzmán, H. Cruz-Manjarrez, L. Rodriguez-Fernandez, J. C. Pineda-Santamaría and M. Aguilar-Franco, *J. Appl. Phys.*, 2013, **113**, 184307.

327 R. P. Blum, H. Niehus, C. Hucho, R. Fortrie, M. V. Ganduglia-Pirovano, J. Sauer, S. Shaikhutdinov and H. J. Freund, *Phys. Rev. Lett.*, 2007, **99**, 226103.

328 A. Pergament, G. Stefanovich and V. Andreeev, *Appl. Phys. Lett.*, 2013, **102**, 2–3.

329 C. Rubin, Aita, *Appl. Phys. Lett.*, 2014, **104**, 2008–2010.

330 M. Nazemiyan and Y. S. Jalili, *AIP Adv.*, 2013, **3**, 112103.

331 M. Gaudon, P. Deniard, L. Voisin, G. Lacombe, F. Darnat, A. Demourgues, J. L. Perillon and S. Jobic, *Dyes Pigm.*, 2012, **95**, 344–350.

332 S. Kumar, F. Maury and N. Bahlawane, *Mater. Res. Soc. Symp. Proc.*, 2005, **2**, 1–5.

333 W. Zhang, H. Li, E. Hopmann and A. Y. Elezzabi, *Nanophotonics*, 2020, **10**, 825–850.

334 A. Cannavale, P. Cossari, G. E. Eperon, S. Colella, F. Fiorito, G. Gigli, H. J. Snaith and A. Listorti, *Energy Environ. Sci.*, 2016, **9**, 2682–2719.

335 W. Zhong, J. Huang, S. Liang, J. Liu, Y. Li, G. Cai, Y. Jiang and J. Liu, *ACS Energy Lett.*, 2020, **5**, 31–38.

336 C. K. Christensen, D. R. Sørensen, J. Hvam and D. B. Ravnsbæk, *Chem. Mater.*, 2019, **31**, 512–520.

337 S. Tepavcevic, H. Xiong, V. R. Stamenkovic, X. Zuo, M. Balasubramanian, V. B. Prakapenka, C. S. Johnson and T. Rajh, *ACS Nano*, 2012, **6**, 530–538.

338 R. Baddour-Hadjean, A. Marzouk and J. P. Pereira-Ramos, *J. Raman Spectrosc.*, 2012, **43**, 153–160.

339 J. M. Coccíantelli, M. Ménétrier, C. Delmas, J. P. Doumerc, M. Pouchard and P. Hagenmuller, *Solid State Ionics*, 1992, **50**, 99–105.

340 X. Rocquefelte, F. Boucher, P. Gressier and G. Ouvrard, *Chem. Mater.*, 2003, **15**, 1812–1819.

341 C. Leger, S. Bach, P. Soudan and J.-P. Pereira-Ramos, *J. Electrochem. Soc.*, 2005, **152**, A236.

342 Y. A. González-Rivera, E. Cervantes-Juárez, L. Aquino-Meneses, R. Lozada-Morales, S. Jiménez-Sandoval, E. Rubio-Rosas, R. Agustín-Serrano, C. De La Cerna, E. Reyes-Cervantes, O. Zelaya Angel, S. A. Tomas, F. Rodriguez-Melgarejo and M. Palomino-Ovando, *J. Lumin.*, 2014, **155**, 119–124.

343 A. Carolin Amala, R. Vignesh, G. V. Geetha and R. Sivakumar, *Phys. Status Solidi A*, 2021, **218**, 1–12.

344 N. S. Kumar, M. S. Raman, J. Chandrasekaran, R. Priya, M. Chavali and R. Suresh, *Mater. Sci. Semicond. Process.*, 2016, **41**, 497–507.

345 M. Firdous, F. K. Butt, S. Zaman, J. Ahmad, M. U. Hassan Farooq, M. Safdar, S. Hussain, M. J. M. Zapata, H. Maqsood and C. Cao, *Ceram. Int.*, 2020, **46**, 16135–16141.

346 D. Porwal, A. C. M. Esther, I. N. Reddy, N. Sridhara, N. P. Yadav, D. Rangappa, P. Bera, C. Anandan, A. K. Sharma and A. Dey, *RSC Adv.*, 2015, **5**, 35737–35745.

347 M. Liberatore, F. Decker, A. Šurca Vuk, B. Orel and G. Dražič, *Sol. Energy Mater. Sol. Cells*, 2006, **90**, 434–443.

348 J. Wu, D. Qiu, H. Zhang, H. Cao, W. Wang, Z. Liu, T. Tian, L. Liang, J. Gao and F. Zhuge, *J. Electrochem. Soc.*, 2018, **165**, D183–D189.

349 S. Zanarini, F. Di Lupo, A. Bedini, S. Vankova, N. Garino, C. Francia and S. Bodoardo, *J. Mater. Chem. C*, 2014, **2**, 8854–8857.

350 M. Panagopoulou, D. Vernardou, E. Koudoumas, D. Tsoukalas and Y. S. Raptis, *Electrochim. Acta*, 2017, **232**, 54–63.

351 H. Liu, D. Wan, A. Ishaq, L. Chen, B. Guo, S. Shi, H. Luo and Y. Gao, *ACS Appl. Mater. Interfaces*, 2016, **8**, 7884–7890.